1-1-2013

Morphologies of Precise Polyethylene-Based Acid Copolymers and Ionomers

Francisco Buitrago
University of Pennsylvania, buitrago@seas.upenn.edu

Morphologies of Precise Polyethylene-Based Acid Copolymers and Ionomers

Abstract
Acid copolymers and ionomers are polymers that contain a small fraction of covalently bound acidic or ionic groups, respectively. For the specific case of polyethylene (PE), acid and ionic pendants enhance many of the physical properties such as toughness, adhesion and rheological properties. These improved properties result from microphase separated aggregates of the polar pendants in the non-polar PE matrix. Despite the widespread industrial use of these materials, rigorous chemical structure - morphology - property relationships remain elusive due to the inevitable structural heterogeneities in the historically-available acid copolymers and ionomers.

Recently, precise acid copolymers and ionomers were successfully synthesized by acyclic diene metathesis (ADMET) polymerization. These precise materials are linear, high molecular weight PEs with pendant acid or ionic functional groups separated by a precisely controlled number of carbon atoms. The morphologies of nine precise acid copolymers and eleven precise ionomers were investigated by X-ray scattering, solid-state 13C nuclear magnetic resonance (NMR) and differential scanning calorimetry (DSC). For comparison, the morphologies of linear PEs with pseudo-random placement of the pendant groups were also studied.

Previous studies of precise copolymers with acrylic acid (AA) found that the microstructural precision produces a new morphology in which PE crystals drive the acid aggregates into layers perpendicular to the chain axes and presumably at the interface between crystalline and amorphous phases. In this dissertation, a second new morphology for acid copolymers is identified in which the aggregates arrange on cubic lattices. The fist report of a cubic morphology was observed at room and elevated temperatures for a copolymer functionalized with two phosphonic acid (PA) groups on every 21st carbon atom. The cubic lattice has been identified as face-centered cubic (FCC).

Overall, three morphology types have been identified for precise acid copolymers and ionomers at room temperature: (1) liquid-like order of aggregates dispersed throughout an amorphous PE matrix, (2) one-dimensional long-range order of aggregates in layers coexisting with PE crystals, and (3) three-dimensional periodicity of aggregates in cubic lattices in a PE matrix featuring defective packing. The liquid-like morphology is a result of high content of acid or ionic substituents deterring PE crystallinity due to steric hindrance. The layered morphology occurs when the content of pendants is low and the PE segments are long enough to crystallize. The cubic morphologies occur in precise copolymers with geminal substitution of phosphonic acid (PA) groups and long, flexible PE segments.

At temperatures above the thermal transitions of the PE matrix, all but one material present a liquid-like morphology. Those conditions are ideal to study the evolution of the interaggregate spacing (d*) in X-ray scattering as a function of PE segment length between pendants, pendant type and pendant architecture (specifically, mono or geminal substitution). Also at elevated temperatures, the morphologies of precise acrylic acid (AA) copolymers and ionomers were investigated further via atomistic molecular dynamics (MD) simulations. The simulations complement X-ray scattering by providing real space visualization of the aggregates, demonstrating the occurrence of isolated, string-like and even percolated aggregate structures.

This is the first dissertation completely devoted to the morphology of precise acid copolymers and precise ionomers. The complete analysis of the morphologies in these novel materials provides new insights into the

shapes of aggregates in acid copolymers and ionomers in general. A key aspect of this thesis is the complementary use of experimental and simulation methods to unlock a wealth of new understanding.

Degree Type
Dissertation

Degree Name
Doctor of Philosophy (PhD)

Graduate Group
Chemical and Biomolecular Engineering

First Advisor
Karen I. Winey

Keywords
Acid copolymer, Ionomer

Subject Categories
Mechanics of Materials | Morphology

MORPHOLOGIES OF PRECISE POLYETHYLENE-BASED ACID COPOLYMERS AND IONOMERS

C. Francisco Buitrago

A DISSERTATION

in

Chemical and Biomolecular Engineering

Presented to the Faculties of the University of Pennsylvania

in Partial Fulfillment of the Requirements for the Degree of Doctor of Philosophy

2013

Supervisor of Dissertation

_____

Karen I. Winey, Professor, Materials Science and Engineering

Graduate Group Chairperson

_____

Raymond J. Gorte, Professor, Chemical and Biomolecular Engineering

Dissertation Committee

John C. Crocker, Associate Professor, Chemical and Biomolecular Engineering

Robert A. Riggleman, Assistant Professor, Chemical and Biomolecular Engineering

Paul A. Heiney, Professor, Physics and Astronomy

MORPHOLOGIES OF PRECISE POLYETHYLENE-BASED ACID COPOLYMERS AND IONOMERS

To the memories of

Ancízar López López and Cornelia Botero Mejía

Acknowledgements

This dissertation has been enriched by the work and dedication of many individuals. In particular, I am indebted to Prof. Karen Winey for her tremendous leadership and relentless dedication. I have grown as a person and as a scientist following her exemplary mentorship, which I hope to emulate in my own endeavors. It has been a privilege to be part of her research group.

I would also like to thank Prof. Paul Heiney, Prof. John Crocker and Prof. Robert Riggleman for serving on my thesis committee. The great majority of the work discussed here is X-ray scattering done at the MAXS facility at Penn, which is mainly overseen and maintained in excellent condition by Prof. Heiney. I appreciate all his teachings and insights into this technique. Many of the analytical methods for studying the structure of materials used in this dissertation were first introduced to me in the class of Prof. Crocker. Whenever I have fundamental questions about the subject, I go back to his instructive lectures. Prof. Riggleman has been a constant presence in the polymer community since his arrival to Penn. I thank him for promoting the exchange of research ideas among polymer scientists.

Many of the results and conclusions in this dissertation stem from collaborations with extraordinary scientists. I would like to thank Prof. Kenneth Wagener, Dr. Kathleen Opper and Dr. Brian Aitken for allowing me to study their unique and extremely valuable precise copolymers and ionomers. I also acknowledge their consistent willingness to answer questions about chemistry and to provide input to my experimental results. I am

especially grateful to Dr. Amalie Frischknecht, Dr. Mark Stevens and Dr. Dan Bolintineanu for the MD simulations included in this dissertation and for insightful discussions about polymer morphology and dynamics. Many of the findings about precise copolymers and ionomers presented here are based on the excellent work by Dr. Christopher Chan and Dr. Michelle Seitz. Finally, the NMR studies were carried out by Dr. Todd Alam and Dr. Janelle Jenkins at Sandia National Laboratories.

I want to extend special gratitude to those that have work alongside me throughout my Ph.D. career. Dr. Minfang Mu and Dr. Sadie White were inspiring presences during the short period I overlapped with them in the research group. Dr. Wenqin Wang, Dr. David Salas de la Cruz and Dr. Jae-Hong Choi have been my models throughout my Ph.D. studies. They spent time training me and explaining every detail of the experimental techniques I have learned in this group. I thank Dr. Rose Mutiso for her continuous companionship and friendship in these five years; and my current colleagues Michael O'Reilly, Wei-Shao Tung, Sharon Sharick, L. Robert Middleton and Han-Chang Yang.

I want to thank the staff members of the Engineering school. Especially, I would like to acknowledge Steven Szewczyk for sharing his knowledge of nearly every piece of equipment in the laboratory. I also thank Dr. Douglas Yates for training me in electron microscopy. Pat Overend, John Linscheid, Vicky Lee, Raymond Hsiao, Magaret Addario and Jackie Egitto have facilitated all my administrative needs.

Most importantly, I would like to thank my parents. This dissertation is also their achievement as they have made enormous sacrifices to allow me the opportunity to study and seek intellectual fulfillment.

ABSTRACT

MORPHOLOGIES OF PRECISE POLYETHYLENE-BASED ACID COPOLYMERS AND IONOMERS

C. Francisco Buitrago

Karen I. Winey

Acid copolymers and ionomers are polymers that contain a small fraction of covalently bound acidic or ionic groups, respectively. For the specific case of polyethylene (PE), acid and ionic pendants enhance many of the physical properties such as toughness, adhesion and rheological properties. These improved properties result from microphase separated aggregates of the polar pendants in the non-polar PE matrix. Despite the widespread industrial use of these materials, rigorous chemical structure – morphology – property relationships remain elusive due to the inevitable structural heterogeneities in the historically-available acid copolymers and ionomers.

Recently, precise acid copolymers and ionomers were successfully synthesized by acyclic diene metathesis (ADMET) polymerization. These precise materials are linear, high molecular weight PEs with pendant acid or ionic functional groups separated by a precisely controlled number of carbon atoms. The morphologies of nine precise acid copolymers and eleven precise ionomers were investigated by X-ray scattering, solid-state ^{13}C nuclear magnetic resonance (NMR) and differential scanning calorimetry

(DSC). For comparison, the morphologies of linear PEs with pseudo-random placement of the pendant groups were also studied.

Previous studies of precise copolymers with acrylic acid (AA) found that the microstructural precision produces a new morphology in which PE crystals drive the acid aggregates into layers perpendicular to the chain axes and presumably at the interface between crystalline and amorphous phases. In this dissertation, a second new morphology for acid copolymers is identified in which the aggregates arrange on cubic lattices. The fist report of a cubic morphology was observed at room and elevated temperatures for a copolymer functionalized with two phosphonic acid (PA) groups on every 21st carbon atom. The cubic lattice has been identified as face-centered cubic (FCC).

Overall, three morphology types have been identified for precise acid copolymers and ionomers at room temperature: (1) liquid-like order of aggregates dispersed throughout an amorphous PE matrix, (2) one-dimensional long-range order of aggregates in layers coexisting with PE crystals, and (3) three-dimensional periodicity of aggregates in cubic lattices in a PE matrix featuring defective packing. The liquid-like morphology is a result of high content of acid or ionic substituents deterring PE crystallinity due to steric hindrance. The layered morphology occurs when the content of pendants is low and the PE segments are long enough to crystallize. The cubic morphologies occur in precise copolymers with geminal substitution of phosphonic acid (PA) groups and long, flexible PE segments.

At temperatures above the thermal transitions of the PE matrix, all but one material present a liquid-like morphology. Those conditions are ideal to study the

evolution of the interaggregate spacing (d^*) in X-ray scattering as a function of PE segment length between pendants, pendant type and pendant architecture (specifically, mono or geminal substitution). Also at elevated temperatures, the morphologies of precise acrylic acid (AA) copolymers and ionomers were investigated further via atomistic molecular dynamics (MD) simulations. The simulations complement X-ray scattering by providing real space visualization of the aggregates, demonstrating the occurrence of isolated, string-like and even percolated aggregate structures.

This is the first dissertation completely devoted to the morphology of precise acid copolymers and precise ionomers. The complete analysis of the morphologies in these novel materials provides new insights into the shapes of aggregates in acid copolymers and ionomers in general. A key aspect of this thesis is the complementary use of experimental and simulation methods to unlock a wealth of new understanding.

Table of Contents

Dedication……..iii

Acknowledgements……...iv

Abstract……vii

Table of Contents……...x

List of Schemes……xiv

List of Tables……xv

List of Figures……...xviii

1. Introduction……..……1

1.1 Polyethylene-Based Acid Copolymers and Ionomers…….……1

1.2 Background of Precise Copolymers via ADMET……...6

1.3 Background of Precise Acid Copolymers and Ionomers……9

1.4 Simulations of Precise Acid Copolymers and Ionomers……...13

1.5 Outline and Contributions……..17

1.6 References……..20

2. A Precise Acid Copolymer Exhibits a Face-Centered Cubic Structure……...27

2.1 Introduction……27

2.2 Experimental Section…….....29

2.2.1 Material…….…29

2.2.2 Sample Preparation……...29

2.2.3 X-ray Scattering……...…….30

2.3 Results and Discussion……...……..….30

2.3.1 One-Dimensional X-ray Scattering at Room Temperature……..30

2.3.2 Two-Dimensional X-ray Scattering at Room Temperature……..34

2.3.3 One-Dimensional X-ray Scattering at Elevated Temperature……..37

2.4 Conclusions.....…...38

2.5 References…….…….39

3. Morphology Trends in Precise Acid- and Ion-Containing Polymers at Elevated Temperature……...40

3.1 Introduction……40

3.2 Experimental Section……44

3.2.1 Materials……...44

3.2.2 X-ray Scattering……47

3.3 Results and Discussion……..49

3.3.1 Acid- and Ion-Rich Aggregates……49

3.3.2 Mono- and Geminal Configurations…….56

3.3.3 Precise and Pseudo-Random Configurations……60

3.4 Conclusions……63

3.5 References……..64

4. Room Temperature Morphologies of Precise Acid- and Ion-Containing Polymers……...……..……...……..68

4.1 Introduction……68

4.2 Experimental Section……72

4.2.1 Materials……...72

4.2.2 Sample Preparation……...73

4.2.3 Differential Scanning Calorimetry……74

4.2.4 Solid-State ^{13}C MAS NMR Spectroscopy……74

4.2.5 X-ray Scattering……75

4.3 Results and Discussion……..75

4.3.1 Liquid-Like Morphologies……75

4.3.2 Layered Morphologies……..82

4.3.3 Cubic Morphologies……..93

4.4 Conclusions……..100

4.5 References……101

5. Direct Comparisons of the Morphologies of Precise Ionomers as Predicted by X-ray scattering and Atomistic MD Simulations…….104

5.1 Introduction……..104

5.2 Experimental Methods……106

5.2.1 Materials……106

5.2.2 X-ray Scattering……..108

5.2.3 Scattering Models……...108

5.3 Simulation Methods……110

5.4 Results and Discussion……112

5.5 Conclusions……..126

5.6 References……127

6. Conclusions and Future Work……130

6.1 Conclusions……..130

6.2 Future Work……133

6.2.1 Morphology of Precise Ionomers as a Function of Neutralization Level...133

6.2.2 FTIR and DRS of Precise Acid Copolymers and Ionomers……...136

6.2.3 Mechanical Testing of Precise Acid Copolymers and Ionomers……138

6.2.4 Morphology and Properties of Precise Copolymers with Sulfonic Acid Pendants……..140

6.3 References……142

Appendix A: Dynamic Mechanical Analysis and Rheology of Precise Ionomers Containing 1-Methylimidazolium Bromide…….144

Appendix B: Additional Information for Chapter 3……..150

Appendix C: Additional Information for Chapter 4……..157

Appendix D: Additional Information for Chapter 5……..162

List of Schemes

Scheme 1.1 General ADMET polymerization procedure followed by exhaustive hydrogenation to achieve perfectly linear polyethylenes functionalized with precisely sequenced pendants (R)……...7

Scheme 2.1 Linear poly(ethylene-*co*-vinylidene phosphonic acid) with geminal phosphonic acid groups on every 21st carbon atom, p21gPA……29

List of Tables

Table 1.1 Composition and Primary Structure Characterization of Precise Acid Copolymers and Ionomers Synthesized by ADMET Polymerization……...13

Table 3.1 Nomenclature, Pendant Volume Fractions and Characteristic Lengths from X-ray Scattering for Twelve Precise Copolymers at $T > T_m$…….46

Table 4.1 Morphology Types and Morphological Parameters for Various Precise Copolymers at Room Temperature (20 °C)……....73

Table 4.2 Thermal Transitions (DSC) and Polyethylene Chain Structure (NMR) for Precise Acid Copolymers and Ionomers……78

Table 5.1 Precise Acid Copolymers and Ionomers Synthesized by ADMET Polymerization and Characterized at 120 °C……...113

Table 5.2 MHS Fit Parameters from X-ray Scattering and Atomistic MD Simulations Compared to Cluster Analysis from Real Space Simulations…….121

Table 5.3 MHC Fit Parameters from X-ray Scattering and Atomistic MD Simulations……..124

Table D.1 Analytical Fits to I(q) from X-ray Scattering and MD Simulations for p9AA……163

Table D.2 Analytical Fits to I(q) from X-ray Scattering and MD Simulations for p15AA……..164

Table D.3 Analytical Fits to I(q) from X-ray Scattering and MD Simulations for p21AA……..165

Table D.4 Analytical Fits to I(q) from X-ray Scattering and MD Simulations for p9AA-43%Li..……..166

Table D.5 Analytical Fits to I(q) from X-ray Scattering and MD Simulations for p15AA-45%Li……..167

Table D.6 Analytical Fits to I(q) from X-ray Scattering and MD Simulations for p9AA-33%Na……..168

Table D.7 Analytical Fits to I(q) from X-ray Scattering and MD Simulations for p15AA-34%Li……..169

Table D.8 Analytical Fits to I(q) from X-ray Scattering and MD Simulations for p9AA-24%Cs……...170

Table D.9 Analytical Fits to I(q) from X-ray Scattering and MD Simulations for p15AA-31%Cs..……...171

Table D.10 Analytical Fits to I(q) from X-ray Scattering and MD Simulations for p15AA-82%Zn..……...172

Table D.11 Analytical Fits to I(q) from X-ray Scattering and MD Simulations for p21AA-56%Zn..……...173

List of Figures

Figure 1.1 Intensity vs. scattering vector (q) for p15AA-81%Zn (blue) and r15AA-82%Zn (gold) at 120 °C. These materials are linear polyethylenes (PE) copolymerized with the same mole fraction of acrylic acid (AA) and partially neutralized with Zn. The pendant groups are either precisely (blue) or randomly (gold) arranged along the PE backbone……..6

Figure 1.2 Visual representations of ionic aggregate morphologies from atomistic MD simulations of partially neutralized precise AA copolymers. Only aggregates with two or more counterions are shown. Different colors are used only to distinguish between different aggregates. Adapted from reference 62……..16

Figure 1.3 Ionic aggregates (grey) from coarse-grained MD simulations. (a) Well-defined aggregates feature PE spacers that bridge the aggregates (red) or form close loops within the same aggregate (blue). (b) Less organized aggregates feature wide loops (purple). Chain ends are shown in green. Adapted from reference 59……..16

Figure 2.1 (a) X-ray scattering intensity as a function of q for p21gPA at room temperature. The arrows indicate the peak positions corresponding to the allowed reflections from a FCC lattice with a lattice parameter of a_{FCC} = 4.19 nm. The green line is the spherical form factor for acid aggregates of radius R_{agg} = 1.1 nm. (b) The measured Bragg distances from X-ray scattering as a function of the assigned Miller indices. The best-fit line uses Equation 2.1 to determine a_{FCC}. The inset shows a FCC lattice, but note that the acid aggregates in blue are shown smaller than experimentally determined for clarity…….32

Figure 2.2 (a) Room temperature X-ray scattering data from a stretched film of p21gPA, where the arrows indicate the stretch direction and correspond to the <1 1 0> direction. (b) X-ray scattering intensity as a function of azimuthal angle extracted from (a) and the specified q values. Simulated diffraction patterns for single crystal FCC lattices when the beam is along the [1 1 0] direction (c) and along the [1 2 1] direction (d). The expected {2 2 0} points, which are not observed in the data due to a minimal in the form factor scattering, are represented as open circles. Black and red dots in (b) indicate whether the observed diffraction peak corresponds to the crystal orientation in (c) or (d), respectively……36

Figure 2.3 (a) X-ray scattering intensity as a function of q for p21gPA at 155 °C. Arrows indicate the allowed reflections for an FCC lattice with a_{FCC} = 4.06 nm. The {2 2 0} reflection is absent due to a minimum in the form factor for a sphere with R_{agg} = 1.1 nm……..38

Figure 3.1: Pendant groups and polymer architectures of polyethylene-based copolymers…….41

Figure 3.2 (a) Intensity vs. scattering vector (q) for precise AA, PA and ImBr materials exhibiting liquid-like morphologies above their thermal transitions. The curves are shifted vertically for clarity. (b) Characteristic lengths ($d^* = 2\pi/q^*$) determined from the low-angle peak as a function of PE spacer……51

Figure 3.3 The effect of pendant size on the relative distance of mono-substituted precise AA, PA and ImBr copolymers at elevated temperature. The relative distances are the d^*-spacings from Figure 2b divided by the length of 9, 15 or 21 carbon-carbon bonds in all-*trans* chain conformation……...55

Figure 3.4 Schematic of amorphous (a) p15AA (ϕ= 0.13) and (b) p15ImBr (ϕ= 0.36). The colored shapes depict globular, discrete aggregates, not individual pendant groups. Although the PE spacer between pendants is the same (15 C-C bonds), the higher volume fraction in p15ImBr produces a substantially larger interaggregate, center-to-center distances (d^*), such that $d^*/l_{\text{all-}trans}>1$……56

Figure 3.5 The effect of geminal substitution on the relative distance in AA and PA precise copolymers at elevated temperature. Note that p21gPA has FCC symmetry, but d^* is extracted from the main scattering peak and corresponds to the interaggregate spacing……...57

Figure 3.6 Wide-angle X-ray scattering at elevated temperature comparing the structure in the amorphous PE regions for single and geminal PA and AA materials. All single copolymers exhibit the typical scattering observed in amorphous PE synthesized via ADMET. The geminal PA copolymers (p21gPA and p15gPA) exhibit two characteristic length scales in the amorphous morphology……..58

Figure 3.7 Room temperature X-ray scattering of 11,11PA and 11,11gPA, which are small molecules with mono- and geminal-substitution of PA pendant groups, respectively. The amorphous halo for 11,11PA is comparable to that of the mono-substituted precise copolymers (p15PA and p21PA, see Figure 3.6), while the amorphous halo for 11,11gPA exhibits one correlation length in distinct contrast to the behavior of geminal-substituted precise copolymers (p15gPA and p21gPA, see Figure 3.6)……..60

Figure 3.8 Intensity vs. X-ray scattering vector for precise vs. pseudo-random PA and ImBr copolymers. Data on the PA copolymers were collected at 150 °C, and for the ImBr materials at 120 °C…….62

Figure 4.1 Precise polymer architecture and pendant groups in polyethylene-based copolymers……..71

Figure 4.2 Morphology types of precise acid copolymers and ionomers at room temperature. The morphologies are characterized by the order of the aggregates (colored globules) in the PE matrix. PE crystals are represented in yellow, and the grey lines represent PE……...71

Figure 4.3 (a) ^{13}C CP MAS NMR spectra of five precise copolymers exhibiting liquid-like morphologies. (b) DSC thermographs of precise AA, PA and ImBr copolymers exhibiting liquid-like morphologies, where the black arrows denote the T_gs. The copolymer p15AA exhibits a small endotherm…….77

Figure 4.4 Room temperature X-ray scattering of precise AA, PA and ImBr copolymers featuring liquid-like packing of aggregates of the associating groups, as evidenced by the broad peaks at q between 2 and 8 nm^{-1}. Data is shifted vertically for clarity in this and subsequent figures……..80

Figure 4.5 ^{13}C CP MAS NMR spectra (left) and deconvolved quantitative ^{13}C MAS NMR data (right) for five precise copolymers exhibiting layered morphologies……..83

Figure 4.6 DSC thermograms of precise AA, PA and ImBr copolymers exhibiting layered morphologies. All materials have polyethylene segments long enough to form crystallites, and their T_ms are indicated by the black arrows…….85

Figure 4.7 X-ray scattering of precise AA, PA and ImBr copolymers featuring layered microphase separated aggregates. Triangles indicate the expected higher order reflections (h = 1, 2, 3, 4, 5) calculated using the a_{layer} (Table 4.1). These copolymers have polyethylene segments that form crystallites, as indicated by the sharp reflections at q ~ 15 nm^{-1}……...87

Figure 4.8 Two-dimensional X-ray scattering patterns of isotropic (left) and oriented (right) semicrystalline AA, PA and ImBr precise copolymers at room temperature: (a) p21AA, (b) p21gAA, (c) p21PA, (d) p15ImBr and (e) p21ImBr. The arrows indicate the draw direction in the oriented films……...89

Figure 4.9 Intensity vs. scattering vector for semicrystalline AA and PA precise copolymers integrated (a) parallel and (b) perpendicular to the draw direction. Triangles indicate the expected higher order reflections (h = 1, 2, 3, 4, 5) calculated using the a_{layer} (Table 4.1)……..90

Figure 4.10 (a) Oriented p21PA showing PA aggregates (red) self-assembled into layers associated to PE crystallites (yellow) and with liquid-like order in the amorphous PE. (b) Oriented p21ImBr having aggregates of ImBr (green) in layers that form during deformation at high temperature and PE crystallites that form between the layers upon cooling. The center-to-center spacings between the PA and ImBr layers are 2.65 nm and 3.33 nm, respectively (Table 4.1). The black arrows indicate the direction of the stretch…….91

Figure 4.11 (a) ^{13}C CP MAS NMR spectra of copolymers with cubic morphologies. (b) DSC thermographs of p15gPA and p21gPA. The black arrows indicate weak thermal transitions……...95

Figure 4.12 Room temperature synchrotron X-ray scattering of p21gPA, the precise copolymer with geminal PA groups on every 21st carbon. The solid red arrows indicate FCC ($a_{cub,\ FCC}$ = 4.10 nm) peaks observed in the pattern. The dotted arrow indicates the position of the expected {2 2 0} peak that coincides with a minimum in the form-factor of spherical aggregates of radius 1.1 nm...……96

Figure 4.13 Synchrotron X-ray scattering of p15gPA, the precise material with geminal PA groups on every 15th carbon. The black triangles indicate the expected reflection for SC ($a_{cub,\ SC}$ = 2.06 nm) and BCC ($a_{cub,\ BCC}$ = 2.90 nm) lattices. For BCC, an additional expected peak is indicated with an open blue triangle. The inset shows the good agreement of equation (1) and the observed peaks with q/q* = 1:2:√5:√8. The two missing peaks corresponding to √3 and √6 match with minima in the form factor of spherical aggregates of radius ~ 0.95 nm (black dashed line)……...98

Figure 5.1 Morphology data from simulations and experiments. (a-c) Snap shots from simulated systems after ~35 ns at 120 °C. Only aggregates with two or more counterions are shown. Different colors represent distinct aggregates. (d-f) Comparisons of structure factor profiles extracted from simulations (red) and X-ray scattering profiles from experiments (black) at 120 °C. Intensity shifted for clarity…….115

Figure 5.2 Peak maxima correspondence for (a) the aggregate peak (q^*_{agg}) and (b) the amorphous halo (q^*_{am}) between experimental and simulated ionomer systems. The legend indicates each sample by the numbers given in Table 5.1. Blue, red and green markers correspond to p9, p15 and p21 materials, respectively……117

Figure 5.3 Relative intensity of the ionomer peak (I^*_{agg}) with respect to the amorphous halo (I^*_{am}) for precise acid copolymers and ionomers obtained from experiments and simulations. Blue, red and green markers correspond to p9, p15 and p21 materials, respectively……..119

Figure 5.4 (a) Real-space CI/SS morphology of p15AA-82%Zn. Spherical (MHS) model fit to (b) Simulated and (b) experimental I(q) profiles……120

Figure 5.5 X-ray scattering of p15AA-82%Zn fit with the MHC model (blue line)…..122

Figure 5.6 (a) Real-space LS morphology of p9AA-43%Li. Cylindrical (MHS) model fit to (b) Simulated and (b) experimental I(q) profiles…….123

Figure 5.7 Close-up to aggregates from p9AA-43%Li. (a) Aggregate diameters, corresponding to 2R, are explicitly indicated. (b) Inter- and intra-aggregate distances measured from the interior of the aggregates are indicated. These distances correspond to $2R_{ca}$……125

Figure 6.1 Single aggregates from a precise AA copolymer (p9AA) with 43% neutralization with (a) Cs and (b) Zn. Oxygen atoms are shown in red, counterions in yellow, and hydrogen atoms in white. Adapted from reference 4……...135

Figure 6.2 FTIR of precise AA copolymers with pendant groups on every 21st (p21AA), 15th (p15AA) and 9th (p9AA) carbon atom. The intense band at 1700 cm^{-1} indicates hydrogen bonded carboxylic acids. The smaller band at 1750 cm^{-1} can quantify the amount of isolated carboxylic acids in the samples. Data courtesy of Hanqing (Elaine) Masser……..137

Figure 6.3 Tensile mechanical data for precise AA copolymers functionalized on every 21st (p21AA), 15th (p15AA) and 9th (p9AA) carbon atom. The elastic modulus (E) is indicated for each species. Data courtesy of L. Robert Middleton……..140

Figure A.1. (a) Storage modulus (G') as a function of temperature for linear polyethylene with various levels of imidazolium bromide substitutions. (b) tanδ as a function of temperature for the same materials……..145

Figure A.2. Master Curve of the storage modulus (G') for precise imidazolium bromide ionomers……...148

Figure B.1 Multiple temperature X-ray scattering for p15ImBr and r21gPA well above their highest transition temperatures……....150

Figure B.2 ^{31}P MAS NMR of the different precise and pseudo random PA polymers at room temperature…….153

Figure B.3 The variable temperature ^{31}P MAS NMR line width for the p21PA copolymer. The line is for a visual guide only…….154

Figure B.4 The variable temperature ^{31}P MAS NMR line width for the p21PA copolymer. The line is for a visual guide only…….154

Figure B.5 The variable temperature ^{31}P MAS NMR line width for the r21PA copolymer. The line is for a visual guide only……..…155

Figure B.6 Variable temperature ^{31}P MAS NMR spectra of PA copolymers before heating (top), at an elevated temperature (middle, 120 ^{o}C) and upon returning to room temperature (bottom)……...156

Figure C.1 DSC (left) and X-ray scattering (right) of p15AA acid copolymers and partially neutralized ionomers with 34% Na (violet line) and 31% Cs (red line)……157

Figure C.2 X-ray scattering intensity as a function of azimuthal angle extracted from the anisotropic pattern of p21PA in Figure 4.7c. The specified *q* values correspond to the maxima of the intensity vs. *q* patterns observed in Figure 4.8……158

Figure C.3 ^{13}C CP NMR MAS data (blue) overlaid with ^{13}C CP NMR MAS data with dipolar-filter (green) and ^{1}H spin-lock (red) data for precise copolymers that exhibit layered morphologies at room temperature. These copolymers are semi-crystalline…..160

Figure C.4 ^{13}C CP NMR MAS data (blue) of the "cubic materials" with overlay of ^{13}C CP NMR MAS data with dipolar-filter (green) and ^{1}H spin-lock (red)……..161

Figure D.1 (a) Real-space morphology of p9AA. (b) Simulated and (b) experimental I(*q*) profiles fit with the MHS and MHC models. Amorphous halo fit with *one or **two Lorentzians……...163

Figure D.2 (a) Real-space morphology of p15AA. (b) Simulated and (b) experimental I(*q*) profiles fit with the MHS and MHC models. Amorphous halo fit with *one or **two Lorentzians……...164

Figure D.3 (a) Real-space morphology of p21AA. (b) Simulated and (b) experimental I(*q*) profiles fit with the MHS and MHC models. Amorphous halo fit with *one or **two Lorentzians……...165

Figure D.4 (a) Real-space morphology of p9AA-43%Li. (b) Simulated and (b) experimental I(q) profiles fit with the MHS and MHC models. Amorphous halo fit with *one or **two Lorentzians……...166

Figure D.5 (a) Real-space morphology of p15AA-45%Li. (b) Simulated and (b) experimental I(q) profiles fit with the MHS and MHC models. Amorphous halo fit with *one or **two Lorentzians……...167

Figure D.6 (a) Real-space morphology of p9AA-33%Na. (b) Simulated and (b) experimental I(q) profiles fit with the MHS and MHC models. Amorphous halo fit with *one or **two Lorentzians……...168

Figure D.7 (a) Real-space morphology of p15AA-34%Na. (b) Simulated and (b) experimental I(q) profiles fit with the MHS and MHC models. Amorphous halo fit with *one or **two Lorentzians……...169

Figure D.8 (a) Real-space morphology of p9AA-24%Cs. (b) Simulated and (b) experimental I(q) profiles fit with the MHS and MHC models. Amorphous halo fit with *one or **two Lorentzians……...170

Figure D.9 (a) Real-space morphology of p15AA-31%Cs. (b) Simulated and (b) experimental I(q) profiles fit with the MHS and MHC models. Amorphous halo fit with *one or **two Lorentzians……...171

Figure D.10 (a) Real-space morphology of p15AA-82%Zn. (b) Simulated and (b) experimental I(q) profiles fit with the MHS and MHC models. Amorphous halo fit with *one or **two Lorentzians……...172

Figure D.11 (a) Real-space morphology of p21AA-56%Zn. (b) Simulated and (b) experimental I(q) profiles fit with the MHS and MHC models. Amorphous halo fit with *one or **two Lorentzians……...173

Chapter 1

Introduction

1.1 Polyethylene-Based Acid Copolymers and Ionomers

Polyethylene (PE), the most common synthetic polymer, offers an astonishing assortment of properties as a result of simple molecular alterations. Among the myriad of possible variations, the incorporation of small amounts of covalently bonded polar groups to the non-polar PE backbone results in substantial improvements in the chemical and physical properties.[1,2] For example, modifications with carboxylic acid or ionized carboxylate pendants yield excellent high temperature strength and transparency ideal for applications in packaging.[3,4] These properties originate from the strong interactions between polar groups giving rise to physical crosslinks between the PE chains that improve the viscoelastic melt properties and disrupt the formation of spherulites. PE-based acid- and ion-containing polymers have also been successfully used as impact resistant plastics (golf balls, bumper guards, etc.) and thermoplastic elastomers, applications in which their toughness and ease of processing make them particularly attractive.[3]

More recently, there has been significant research interest in ion-containing polymers (or ionomers) and acid copolymers as solid polymer electrolytes for batteries and fuel cells.[5-1] Lithium neutralized ionomers can potentially be used as single ion conducting electrolytes in lithium-based batteries. Such ionomer membranes could cheaply fulfill the ion conductivity and electrode separation requirements, while relieving

the safety concerns commonly found in liquid electrolytes.[6] Polymer electrolytes containing phosphonic acid and imidazole groups have also been suggested as convenient substitutes for sulfonated materials in polymer electrolyte membrane (PEM) fuel cells due to their good proton conductivity at intermediate temperatures (below 200 °C) and low humidity.[9] In addition, it has been suggested that phosphonic acid transports protons exclusively through structural diffusion thanks to its ability to act as a proton donor and acceptor.[11]

Historically, the most widely researched PE-based acid copolymers are those with random placement of carboxylic acid pendants.[12,13] The carboxylic acid pendants can be neutralized with a variety of cations such as sodium or zinc to produce carboxylate ionomers. Previous studies of these materials have been directed towards elucidating the origin of improved physical properties such as melt viscosity and relaxation times. It is now extensively accepted that those properties result from strong interactions between the acid or ionic groups that act as physical crosslinks restraining polymer diffusion.[12] Since the polar groups exist in a low dielectric constant PE medium, they tend to microphase separate into assemblies that can vary from simple ion pairs to larger aggregates. However, the shape, composition and spatial arrangement of those assemblies have been heavily debated, and many models have been put forward to help explain experimental observations.

For acid copolymers and ionomers in general, dynamic mechanical analysis (DMA) indicates that the addition of polar groups results in a rubbery plateau in the modulus that persists well above the highest thermal transition of the parent

homopolymer.[3] In addition, the end of this plateau is accompanied by an extra thermal transition that is only observed in the functionalized materials. These physical properties have been linked to the morphology by the Eisenberg-Hird-Moore (EHM) model,[14] in which two phases with separate thermal transitions coexist. One thermal transition is associated to the polymer matrix far from acid or ionic aggregates, and the other to the polymer matrix adjacent to aggregates having restricted mobility. However, at room temperature this model is inadequate to describe PE-based copolymers, as it neglects the contribution of PE crystals to the properties. It has been reported that functionalization with acid or ionic pendants reduces the percent crystallinity of PE,[13] but the extent of this crystallinity loss cannot be predicted for specific levels of functionalization and neutralization due to structural inconsistencies from sample to sample. A complete understanding of the structure-property relationships in PE-based ionomers is hampered further by the evolution of secondary crystallites after extended aging at room temperature.[15]

Another experimental observation that is typical of ionomers is a correlation peak at low angles in X-ray scattering. Although it is generally accepted that this peak results from electron density contrast between the polar aggregates and the non-polar polymer matrix, its detailed meaning with regards to morphology has been a matter of disagreement.[3,16,17] Currently, the most popular model used to gather quantitative information from this ionomer peak was introduced by Yarusso and Cooper, which approximates the aggregates as monodisperse spheres of increased ion density with liquid-like packing in the polymer matrix.[18,19] A modification to this model based on

work by Kinning and Thomas proposes a corona composed of polymer segments with restricted mobility surrounding the aggregates and imposing a separation of closest approach between them.[20,21] In this dissertation, this model will be referred to as the modified hard-sphere (MHS) model.

The implementation of the MHS model requires validation of its assumptions by other experimental methods. High-angle annular dark-field scanning transmission electron microscopy (HAADF-STEM) has been successfully implemented for direct imaging of ionic aggregates in some ionomer systems.[22-30] Suitable samples must consist of atomic species that lend a considerable degree of atomic number contrast (Z-contrast) between the ionic and the non-polar regions of the material. In the case of PE-based ionomers with pendant carboxylate anionic groups, neutralizing cations with high atomic number such as copper, zinc or cesium are indispensable for effective Z-contrast with the hydrocarbon matrix. Unfortunately, in employing HAADF-STEM to image these ionic aggregates, effective Z-contrast is not achieved between the carbon, oxygen and hydroxyl groups, which play an essential part in aggregate formation due to hydrogen bonding, and constitute a significant portion of the volume of the aggregates. Another drawback of HAADF-STEM is that it captures transmission images of samples with finite thickness, where the specimen (~ 50 nm) is significantly thicker than general aggregate sizes (~ 1 nm). Therefore, the resulting micrographs are two-dimensional projections of ionic aggregates arranged in 3-D and featuring extensive overlap between the aggregates, which is particularly problematic due to the small size of the aggregates and the resolution capabilities of most electron microscopes. For all these reasons, HAADF-

STEM is prone to generate a distorted picture of the size and arrangement of ionic aggregates.

Despite the established and possible commercial applications of ionomers and acid copolymers, realizing their full potential requires fundamental understanding of their chemical structure – processing – morphology – property relationships. This task has been historically challenging due to the lack of structural control over the polymers, which would allow a systematic study of the effects of tunable characteristics on the morphology and properties. Furthermore, a molecular-level understanding of the morphology and dynamics dictating the macroscopic properties cannot be attained via common experimental techniques. This dissertation summarizes progress on that front made possible by the development of precise acid copolymers and ionomers synthesized via acyclic diene metathesis (ADMET) polymerization. Precise copolymers and ionomers are linear PE functionalized with polar groups at an exact and consistent sequence of carbon atoms along the polymer backbone. This level of structural precision is a great help experimentally because it generates unprecedentedly well-defined morphology and property data (Figure 1.1). Additionally, these homogeneous model materials can be simulated to complement the experiments and gain molecular-level knowledge of morphology and dynamics.

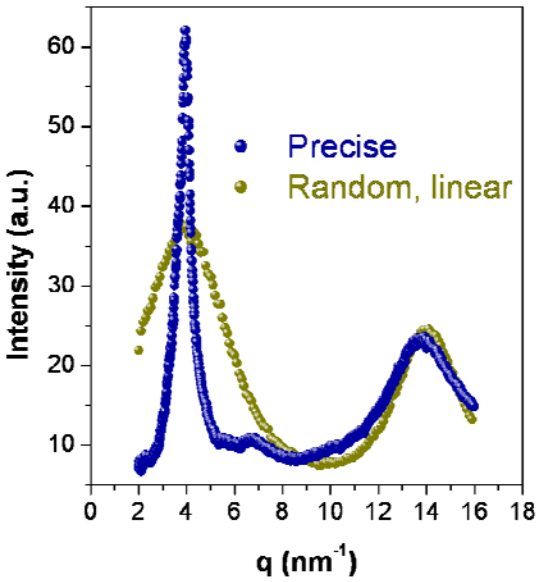

Figure 1.1 Intensity vs. scattering vector (q) for p15AA-81%Zn (blue) and r15AA-82%Zn (gold) at 120 °C. These materials are linear polyethylenes (PE) copolymerized with the same mole fraction of acrylic acid (AA) and partially neutralized with Zn. The pendant groups are either precisely (blue) or randomly (gold) arranged along the PE backbone.

1.2 Background of Precise Copolymers via ADMET

In the polymer community, ADMET polymerization first came to prominence as a controlled method to incorporate pendant groups into polymer systems by taking advantage of symmetrical diene monomers reacted in the presence of Grubbs' catalysts (Scheme 1.1). Followed by a hydrogenation reaction, this variety of step-growth polymerization produces linear copolymers of ethylene and various comonomers that would be unattainable through chain-growth polymerization methods, where the differences in reactivity of the reactants produces chain transfer defects and low

comonomer inclusion.[31] Thereon, researchers started to use this synthesis method as a tool to help elucidate fundamental structure-property relationships in PE-based copolymers.

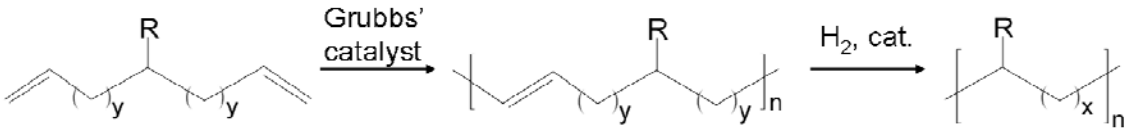

Scheme 1.1 General ADMET polymerization procedure followed by exhaustive hydrogenation to achieve perfectly linear polyethylenes functionalized with precisely sequenced pendants (R).

Wagener and co-workers reported the first successful implementation of ADMET polymerization to achieve linear PE for structure-property investigations.[32] In comparison to typical industrially produced materials, the linear ADMET PEs in this first report had lower molecular weights (Mn = 15.0 kg/mol). However, that value is well above the entanglement molecular weight for linear PE (1.0 kg/mol),[31] allowing for a reliable examination of the melting temperature (T_m) and enthalpy of melting (ΔH_m) in high-molecular weight, defect-free and highly crystalline hydrocarbons. The effect of the PE structure on the thermal properties continued with the synthesis of precisely branched, linear PE. Initially, methyl branches were incorporated at a variety of precise sequences along the polymer chain using ADMET.[33] In that study, the T_m was observed to decrease from 134 °C for linear ADMET PE, to 62 °C for methyl branches every 21st carbon atom, and all the way down to 35 °C for methyl branches on every 15th atom. Further research

led to the synthesis of PE with precise ethyl branches,[34] and butyl and hexyl branches.[35,36] A comprehensive study on the effect of branches ranging from methyl to adamantyl groups and placed on every 21st atom on the structure-property relationships of PE found that methyl and ethyl branching decrease the T_m in a systematic way accompanied by a transition in the crystalline PE unit cell from orthorhombic to triclinic due to incorporation of the defects in the crystals. For bulkier branches equal or greater in mass than propyl, defective crystals melting at a constant temperature (~ 10 °C) were found due to exclusion of the branches from the crystals into the amorphous phase.[37]

ADMET PEs containing a precise distribution of pendant halogens were also synthesized to study their structure-property relationships.[38-40] The motivation for this work was the wide range of applications that halogenated polymers such as PVC and PTFE produce as a result of changes in the polymer structure. Precise materials functionalized with fluorine, chlorine and bromine on every 19th carbon atom exhibit homopolymer-like behavior as evidenced by sharp crystalline PE diffraction rings (WAXD) and narrow melting endotherms (DSC).[39] In contrast, copolymers with random halogen distributions and with similar or lower branching levels usually exhibit much broader WAXD peaks and melting endotherms.[40-42] In a similar way to precise methyl branches, the relatively small chlorine and bromine atoms are incorporated into the PE crystals causing the orthorhombic unit cell to evolve into triclinic. However, fluorine atoms are small enough to go into the orthorhombic crystals with minimum disruptions to the unit cell dimensions. Precisely distributed pendant carbonyl oxygens were examined in the same study and also shown to be incorporated in the orthorhombic unit cell. The

precise copolymers that preserve the orthorhombic unit cells display melting endotherms ~ 130 °C, whereas those with triclinic unit cells melt at ~ 60 °C.[39] Finally, besides the precise acid copolymers and ionomers discussed in this dissertation, other PE-based copolymers synthesized by ADMET whose properties have not yet been studied in depth include acetates,[43] PEO[44] and pi-conjugated chromophores.[45]

1.3 Background of Precise Acid Copolymers and Ionomers

The incorporation of polar groups along the non-polar PE backbones has been researched during the better part of the last 50 years to attain a wide variety of material properties. Acid and ionic pendants endow PE with enhanced toughness, adhesion, barrier properties, surface properties and rheological properties.[2] In addition to those new properties, the periodic incorporation of those polar groups has the potential of preserving crystallinity and thus maintaining high modulus, strength and solvent resistance even at high comonomer concentrations. Random PE-based ionomers are usually obtained by neutralization of the parent acid copolymers. The synthesis of these copolymers can be achieved either by copolymerization with a monomer containing the acid pendant, or by a postsynthesis modification of a nonionic polymer.[4] These synthetic methods have been optimized commercially using high-pressure free radical polymerization. Early attempts to synthesize highly regular PE with acidic functional groups involved protection-deprotection strategies to improve their compatibility with metallocene and Ziegler-Natta catalysts.[2,31] However, those attempts were more successful for esters or alcohols than for acids. In the 1970s, Shell reported the synthesis of copolymers of 10-undecenoic acid

with 1-hexene and 4-methyl-1-pentene to obtain macromolecules with periodic carboxylic acid pendants.[46] This synthesis featured the protected form alumino tris-(10-undecenoate), but following deprotection the systems contained appreciable amounts of anhydrides and carboxylate groups in addition to the acids. An improved method for the copolymerization of 10-undecenoic acid with ethylene was suggested by Aaltoen et al., but deactivation of the catalyst proved too severe for practical implementation.[47] Synthesis of highly regular olefins/esters copolymers followed by deprotection can also yield acid copolymers and carboxylate ionomers. For example, sodium carboxylate ionomers can be obtained by the reaction of 2,6-dimethylphenyl 10-undecenoate with ethylene, which can be treated with acetic acid to generate the carboxylic acid copolymers.[48,49] None of the examples above, nor the standard high-pressure free radical polymerization technique can achieve copolymers with the level of microstructural precision required for rigorous structure-property relationship studies.

The first report of ADMET PE copolymerized with acrylic acid (AA) was published in 2007 by Baughman, *et al*.[50] Before polymerization, the symmetrical diene monomers were protected with a hemiacetal ester moiety designed to prevent decomposition of the first-generation Grubbs' catalyst by the acidic groups. Hydrogenation and deprotection of the copolymers were performed using a Wilkinson's catalyst in a hydrogen atmosphere. The resulting materials featured carboxylic acid pendants on every 9th (p9AA, 22 mol% AA), 15th (p15AA, 13 mol% AA) and 21st (p21AA, 9.5 mol% AA) carbon atom. Primary structure characterization by gel permeation chromatography (GPC) found that the resulting precise acid copolymers had

high molecular weights and polydispersity indexes (PDI) of ~ 2 (Table 1.1).[50] DSC data of as-synthesized samples showed that neither p9AA nor p15AA formed crystals due to the limited chain mobility imposed by the AA groups forming physical cross-links. However, p21AA presented a sharp melting endotherm at 45 °C arising from the long defect-free ethylene runs between acid pendants. Following the successful synthesis of the AA copolymers, the same samples were ionized in a 75/25 v/v solvent mixture of 1,4 dioxane and 1-butanol, and subsequently neutralized at different levels with Zn,[51] Li, Na and Cs.[52]

Following the successful synthesis and characterization of the AA copolymers, precise materials with phosphonic acid (PA) pendants were reported.[53,54] Along with the single pendants, geminal precise copolymers featuring two PA groups on every 15th (p15gPA) or 21st (p21gPA) atom were presented for the first time. In this case, decomposition of the first-generation Grubbs' catalyst is avoided via esterification of the acid pendants. After polymerization and exhaustive hydrogenation of the double bonds, deprotected PA pendants were obtained by hydrolysis. Primary structural information by GPC is shown in Table 1.1.[54] Similar to the AA variety, as-synthesized p9PA and p15PA did not exhibit any crystallinity by DSC due to the defects and cross-links introduced by the bulky, pendant groups. On the other hand, p21PA and p21gPA featured peculiar melting behaviors never seen previously in precise ADMET copolymers. After erasing their thermal history, no recrystallization was evident after 72 hours of aging at room temperature. Then, p21PA exhibited two T_ms attributed to primary and secondary crystals developing at different stages of the recrystallization process. For p21gPA, an extremely

broad melting endotherm peaking at 87 °C and spanning approximately 100 ° is observed.[54]

The final group of materials studied in this dissertation is a family of precise ionomers featuring 1-methylimidazolium bromide (ImBr) pendants.[55] After several unsuccessful attempts to polymerize diene monomers containing the ionic groups, a clever strategy was devised in which bromine-functionalized precise copolymers were attained by ADMET and hydrogenation, followed by quantitative quaternization using excess 1-methylimidazole. Primary analysis by GPC is found in Table 1.1.[55] Thermal characterization of as-synthesized samples was carried out by DSC and DMA, producing similar trends to those previously discussed for AA and PA copolymers. In this case, both p9ImBr and p15ImBr only showed T_gs while p21ImBr had two T_ms at 88 and 106 °C. In addition, DMA confirmed that all three precise copolymers underwent thermal transitions below 20 °C related to chain relaxation of the PE matrix. Higher thermal transitions ranging between 50 to 80 °C were associated with relaxation in ionic aggregates.

Table 1.1 Composition and Primary Structure Characterization of Precise Acid Copolymers and Ionomers Synthesized by ADMET Polymerization

Sample	mol% functional comonomer	M_n (kg/mol)	M_w (kg/mol)	PDI
p9AA	22	25.1	40.8	1.62
p15AA	13	31.8	59.1	1.86
p21AA	9.5	37.7	65.2	1.73
p9PA	22	10.6	17.1	1.61
p15PA	13	23.6	40.4	1.68
p21PA	9.5	17.9	34.5	1.93
p15gPA	13	6.2	11.4	1.82
p21gPA	9.5	19.5	33.3	1.71
p9ImBr	22	38.0	79.8	2.1
p15ImBr	13	44.0	88.0	2.0
p21ImBr	9.5	53.0	106	2.0

GPC data obtained in THF relative to PS standards.

1.4 Simulations of Precise Acid Copolymers and Ionomers

The development of precise copolymers has facilitated the use of simulation methods to complement the morphological information obtained from experimental techniques. Since precise copolymers are structurally simple and homogeneous, they serve as model materials for molecular dynamics (MD) simulations. These MD simulations of precise copolymers result in real-space representations that serve as alternatives to direct imaging of ionomer morphology through microscopy. Simulation and theoretical studies also provide access to information about charged polymer systems that is well beyond the capabilities of current experimental methods. In particular, the local environment and dynamics of the aggregates are two queries that require molecular-

level resolution. Most of the previous computational work in polymer systems with charged functional groups has been motivated by their promise for fuel cell applications,[56] or focused on their remarkable glass transition behavior.[57] Other research that specifically probed aggregates in polymer systems containing associating groups was employed using so-called stickers, which have short-range attraction to each other but do not experience repulsive same-charge-like interactions. These systems were observed to form discrete, roughly spherical aggregates when the stickers were placed in-chain or in the chain ends.[58]

Coarse-grained and fully atomistic MD simulations of precise acid copolymers and ionomers in the melt have recently been published.[59-62] Real space visualization of the simulation boxes confirms aggregation of the polar groups in the non-polar matrix. However, the aggregate sizes and shapes are much more diverse than previously hypothesized. Clear differences in the ionic aggregates have been observed as a function of charged group placement (in-chain vs. pendant),[59] PE spacer length between functionalizations,[60] level of neutralization and cation type.[61,62] In addition, comparisons between precise and random configurations of linear ionomers also exhibit different evolutions in aggregate morphology as a function of charged group placement and architecture.[60] The aggregate morphologies identified in the atomistic MD simulation studies are shown in Figure 1.2 and include "compact, isolated" (CI); "short, stringy" (SS); "long, stringy" (LS); "partially percolated" (PP) and "fully percolated" (FP).[62] Furthermore, the atomistic MD simulations contain enough detail to enable structure factor calculations that include atomic form factors, and can therefore be compared

directly to X-ray scattering data.[62] The simulated X-ray scattering profiles demonstrate that the aggregate peak at low angles is present in all ionomers independent of their aggregate morphology type from real space examinations. Further analysis of the radial distribution functions confirm that the aggregate peak can originate from both, inter- and intra-aggregate interference scattering.[59] A final finding about the morphology of precise ionomer melts through simulations involves the improved ordering detected in these materials by X-ray scattering.[51,63] The inter- and/or intra-aggregate separation in these systems correlates very well with the precise PE spacers imposed by their molecular structures. The reason for this is the propensity of the PE spacers to act as bridges between aggregates or to form close loops which exit and re-enter into the same aggregate at a great proximity.[60] Wide loops, linking well-separated ion groups within the same aggregate, were found with much less frequency (Figure 1.3).

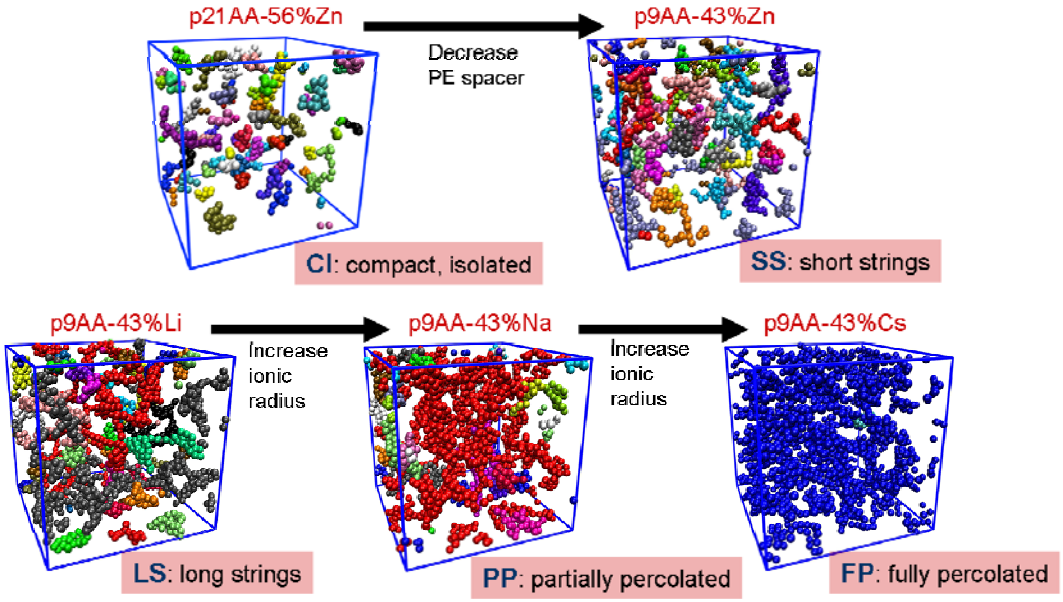

Figure 1.2 Visual representations of ionic aggregate morphologies from atomistic MD simulations of partially neutralized precise AA copolymers. Only aggregates with two or more counterions are shown. Different colors are used only to distinguish between different aggregates. Adapted from reference 62.

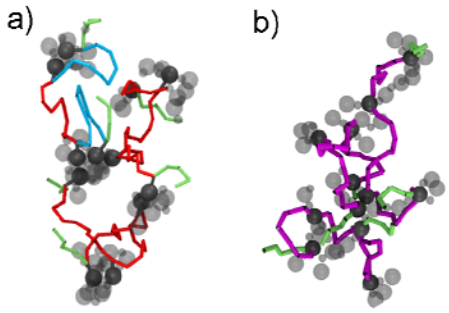

Figure 1.3 Ionic aggregates (grey) from coarse-grained MD simulations. (a) Well-defined aggregates feature PE spacers that bridge the aggregates (red) or form close loops within the same aggregate (blue). (b) Less organized aggregates feature wide loops (purple). Chain ends are shown in green. Adapted from reference 59.

The molecular-level resolution of the MD simulations allows for the study of dynamics in ionomers. Prior to MD simulations of precise ionomers had taken place, computational work was utilized to predict diffusion constants for ionomers without focusing on the mechanism of counterion transport.[64,57] In fact, previous theoretical studies relied on an ion hopping mechanism for dynamics proposed from stress relaxation and rheology experiments.[65,66] In contrast, recent coarse-grained MD simulations found that isolated aggregates merge into larger structures, where ionic rearrangements occur fairly quickly in the melt.[67] These larger ionic aggregates later break forming new isolated aggregates having exchanged ions in the process.

1.5 Outline and Contributions

This dissertation adds to the extraordinary breakthroughs in the fundamental research of acid copolymers and ionomers attributed to the development of precise ADMET materials. The microstructural homogeneity of these copolymers results in morphologies with unprecedented aggregate order, producing in some instances periodic aggregate structures in 1 and 3 dimensions. The effect of pendant type, length of PE segments between pendants, pendant architecture, and neutralizing cations in carboxylate ionomers on the morphologies at elevated and room temperatures were studied using X-ray scattering, solid-state nuclear magnetic resonance (NMR) spectroscopy and differential scanning calorimetry (DSC). To complement the information from experimental techniques, MD simulations of precise model materials were carried out to

provide real space visualization of the morphologies. Quite unexpectedly, a diverse group of aggregate shapes were identified, which provide an opportunity to validate the MHS model and to propose other variations when appropriate.

In Chapter 2, the morphology of a linear PE precisely functionalized with geminal PA pendants on every 21st carbon atom (p21gPA), is shown to exhibit a face-centered cubic (FCC) packing of acid aggregates.[68] This is the first report of cubic ordering of aggregates in an acid copolymer, and it is the direct consequence of the molecular precision of the material. X-ray scattering from isotropic films results in higher-order peaks used to determine the lattice parameter at room temperature (a_{FCC} = 4.19 nm) and at 155 °C, well above the thermal transition of the polyethylene matrix (a_{FCC} = 4.06 nm). Stretching the material produces an anisotropic scattering pattern featuring two coexisting crystalline orientations results, both having the <110> direction of the FCC lattice along the stretching direction. This chapter was published in *ACS Macro Letters*: Buitrago, C. F.; Opper, K. L; Wagener, K. B.; Winey, K. I. *ACS Macro Lett.* **2012**, 1, 71-74.

Chapter 3 presents the morphologies at elevated temperatures ($T > T_g$, T_m) of twelve precise PEs copolymerized with AA, PA and ImBr groups.[63] These precise copolymers have one or two pendant groups on every 9th, 15th or 21st carbon atom along the PE chain. The morphologies were studied via X-ray scattering. The polar pendant groups in these materials self-assemble into microphase-separated aggregates dispersed throughout the non-polar PE matrix. At high temperatures the PE segments are amorphous, such that the aggregates are distributed in a liquid-like manner in eleven of these precise copolymers. As mentioned before, the one exception is p21gPA, which has

long-range order of aggregates even at elevated temperatures (FCC lattice). The correlations distances between aggregates are found to increase with the following: carbon spacer length between pendant groups, size and volume fraction of the pendant species, and functional group configuration (single vs. geminal substitution). Compared to the commercial, random versions of acid- and ion-containing polymers, precise copolymers exhibit sharper and more intense X-ray scattering peaks that increase the certainty about the morphology of this class of materials. This chapter has been submitted to *Macromolecules*: Buitrago, C. F.; Alam, T. M.; Opper, K. L.; Aitken, B. S.; Wagener, K. B.; Winey, K. I. *Macromolecules*, Submitted.

In Chapter 4, the room temperature morphologies of the same twelve precise copolymers discussed in Chapter 3 are studied by DSC, solid-state ^{13}C NMR and X-ray scattering.[69] The polar pendants microphase separate from the non-polar PE segments, giving rise to acid-rich or ionic aggregates dispersed throughout the matrix. DSC and ^{13}C NMR found that steric congestion and decreased diffusional motion caused by the associating pendants have repercussions on the macrostructure of the polymer matrix, going from moderately semi-crystalline (~ 35%) to completely amorphous as the frequency of the pendants increases. The precise nature of the substitutions along the polymer chains gives rise to highly ordered morphologies unknown in traditional acid- and ion-containing polymers. Copolymers substituted on every 9^{th} carbon feature liquid-like packing of the aggregates with narrower spatial and size distributions, as suggested by their comparatively sharp and more intense aggregate peaks in relation to random, commercial varieties. As the frequency of the pendants decreases, allowing PE

crystallization, hierarchical structures form with aggregates arranged in layers perpendicular to the axes of the polymer chains. A third morphology variety identified in this study features cubic packing of the aggregates, which requires the flexibility afforded by long PE spacers and the high volume fraction of aggregates attained by geminal PA groups on every substituted carbon. This chapter has been submitted to *Macromolecules*: Buitrago, C. F.; Jenkins, J. E.; Opper, K. L.; Aitken, B. S.; Wagener, K. B.; Alam, T. M.; Winey, K. I. *Macromolecules*, Submitted.

In Chapter 5, the melt morphology of three precise AA copolymers and eight ionomers obtained by neutralizing them with Zn, Li, Na and Cs are studied by X-ray scattering and atomistic MD simulations.[52] Direct comparisons of experimental X-ray scattering profiles and the structure factors from the simulations are in excellent agreement. This concurrence suggests that precise AA copolymers and ionomers form aggregates that can range from compact, isolated to stringy to percolated structures. In addition, the suitability of the MHS model is tested and contrasted with a new model for string-like or cylindrical ionic aggregates (the modified hard-cylinder model, MHC).

Chapter 6 presents the conclusions of the dissertation and a discussion of ongoing and future work. Appendix A discusses DMA and melt rheology for one random and 3 precise ImBr ionomers.[55] Appendices B, C and D contain additional information for Chapters 3, 4 and 5.

1.6 References

1. Padwa, A. R. *Prog. Polym. Sci.* **1989,** 14, (6), 811-833.

2. Boffa, L. S.; Novak, B. M. *Chem. Rev.* **2000,** 100, (4), 1479-1493.

3. Eisenberg, A.; Kim, J.-S., *Introduction to Ionomers*. 1st ed. ed.; Wiley: New York, 1998.

4. Grady, B. P. *Polym. Eng. Sci.* **2008,** 48, (6), 1029-1051.

5. Schlick, S., *Ionomers: Characterization, Theory and applications*. CRC Press: Boca Raton, FL, 1996.

6. Meyer, W. H. *Adv. Mater.* **1998,** 10, (6), 439-+.

7. Wright, P. V. *MRS Bull.* **2002,** 27, (8), 597-602.

8. Kreuer, K. D. *ChemPhysChem* **2002,** 3, (9), 771-+.

9. Schuster, M.; Rager, T.; Noda, A.; Kreuer, K. D.; Maier, J. *Fuel Cells* **2004,** 5, (3), 355-365.

10. Steininger, H.; Schuster, M.; Kreuer, K. D.; Kaltbeitzel, A.; Bingol, B.; Meyer, W. H.; Schauff, S.; Brunklaus, G.; Maier, J.; Spiess, H. W. *Phys. Chem. Chem. Phys.* **2007,** 9, (15), 1764-1773.

11. Schuster, M.; Kreuer, K. D.; Steininger, H.; Maier, J. *Solid State Ion.* **2008,** 179, (15-16), 523-528.

12. Capek, I. *Adv. Colloid Interface Sci.* **2004,** 112, (1-3), 1-29.

13. Capek, I. *Adv. Colloid Interface Sci.* **2005,** 118, (1-3), 73-112.

14. Eisenberg, A.; Hird, B.; Moore, R. B. *Macromolecules* **1990,** 23, 4098-4107.

15. Loo, Y. L.; Wakabayashi, K.; Huang, Y. E.; Register, R. A.; Hsiao, B. S. *Polymer* **2005,** 46, (14), 5118-5124.

16. Marx, C. L.; Caulfield, D. F.; Cooper, S. L. *Macromolecules* **1973,** 6, (3), 344-353.

17. Macknigh.Wj; Taggart, W. P.; Stein, R. S. *Journal of Polymer Science Part C-Polymer Symposium* **1974**, (45), 113-128.

18. Yarusso, D. J.; Cooper, S. L. *Macromolecules* **1983,** 16, (12), 1871-1880.

19. Yarusso, D.; Cooper, S. L. *Polymer* **1985,** 26, (3), 371-378.

20. Kinning, D. J.; Thomas, E. L. *Macromolecules* **1984,** 17, 1712-1718.

21. Ding, Y. S. H., S. R.; Hodgson, K. O.; Register, R. A.; Cooper, S. L. *Macromolecules* **1988,** 21, (6), 1698-1703.

22. Benetatos, N. M.; Chan, C. D.; Winey, K. I. *Macromolecules* **2007,** 40, (4), 1081-1088.

23. Batra, A.; Cohen, C.; Kim, H.; Winey, K. I. *Macromolecules* **2006,** 39, (4), 1630-1638.

24. Benetatos, N. M.; Winey, K. I. *J. Polym. Sci. Pt. B-Polym. Phys.* **2005,** 43, (24), 3549-3554.

25. Kirkmeyer, B. P.; Puetter, R. C.; Yahil, A.; Winey, K. I. *J. Polym. Sci. Pt. B-Polym. Phys.* **2003,** 41, (4), 319-326.

26. Kirkmeyer, B. P.; Weiss, R. A.; Winey, K. I. *J. Polym. Sci. Pt. B-Polym. Phys.* **2001,** 39, (5), 477-483.

27. Winey, K. I.; Laurer, J. H.; Kirkmeyer, B. P. *Macromolecules* **2000,** 33, (2), 507-513.

28. Taubert, A.; Winey, K. I. *Macromolecules* **2002,** 35, (19), 7419-7426.

29. Kirkmeyer, B. P.; Taubert, A.; Kim, J.-S.; Winey, K. I. *Macromolecules* **2002,** 35, (7), 2648-2653.

30. Benetatos, N. M.; Winey, K. I. *Macromolecules* **2007,** 40, (9), 3223-3228.

31. Baughman, T. W.; Wagener, K. B., Recent advances in ADMET polymerization. In *Metathesis Polymerization*, 2005; Vol. 176, pp 1-42.

32. Ogara, J. E.; Wagener, K. B. *Makromolekulare Chemie-Rapid Communications* **1993,** 14, (10), 657-662.

33. Smith, J. A.; Brzezinska, K. R.; Valenti, D. J.; Wagener, K. B. *Macromolecules* **2000,** 33, (10), 3781-3794.

34. Sworen, J. C.; Smith, J. A.; Berg, J. M.; Wagener, K. B. *J. Am. Chem. Soc.* **2004,** 126, (36), 11238-11246.

35. Sworen, J. C.; Wagener, K. B. *Macromolecules* **2007,** 40, (13), 4414-4423.

36. Rojas, G.; Wagener, K. B. *Macromolecules* **2009,** 42, 1934 - 1947.

37. Rojas, G.; Inci, B.; Wei, Y. Y.; Wagener, K. B. *J. Am. Chem. Soc.* **2009,** 131, (47), 17376-17386.

38. Watson, M. D.; Wagener, K. B. *Macromolecules* **2000,** 33, (24), 8963-8970.

39. Boz, E.; Wagener, K. B.; Ghosal, A.; Fu, R. Q.; Alamo, R. G. *Macromolecules* **2006,** 39, (13), 4437-4447.

40. Alamo, R. G.; Jeon, K.; Smith, R. L.; Boz, E.; Wagener, K. B.; Bockstaller, M. R. *Macromolecules* **2008,** 41, (19), 7141-7151.

41. Stephens, C. H.; Yang, H.; Islam, M.; Chum, S. P.; Rowan, S. J.; Hiltner, A.; Baer, E. *J. Polym. Sci. Pt. B-Polym. Phys.* **2003,** 41, (17), 2062-2070.

42. Gomez, M. A.; Tonelli, A. E.; Lovinger, A. J.; Schilling, F. C.; Cozine, M. H.; Davis, D. D. *Macromolecules* **1989,** 22, (12), 4441-4451.

43. Watson, M. D.; Wagener, K. B. *Macromolecules* **2000,** 33, (15), 5411-5417.

44. Berda, E. B.; Wagener, K. B. *Macromolecules* **2008,** 41, (14), 5116-5122.

45. Mei, J. G.; Aitken, B. S.; Graham, K. R.; Wagener, K. B.; Reynolds, J. R. *Macromolecules* **2010,** 43, (14), 5909-5913.

46. Holler, H. V.; Youngman, E. A. Polymerization Process and Products. 1973.

47. Aaltonen, P.; Lofgren, B. *Eur. Polym. J.* **1997,** 33, (8), 1187-1190.

48. Purgett, M. D.; Vogl, O. *Journal of Macromolecular Science-Chemistry* **1987,** A24, (12), 1465-1481.

49. Purgett, M. D.; Macknight, W. J.; Vogl, O. *Polym. Eng. Sci.* **1987,** 27, (19), 1461-1468.

50. Baughman, T. W.; Chan, C. D.; Winey, K. I.; Wagener, K. B. *Macromolecules* **2007,** 40, (18), 6564-6571.

51. Seitz, M. E.; Chan, C. D.; Opper, K. L.; Baughman, T. W.; Wagener, K. B.; Winey, K. I. *J. Am. Chem. Soc.* **2010,** 132, (23), 8165-8174.

52. Buitrago, C. F.; Bolintineanu, D. S.; Seitz, M. E.; Stevens, M. J.; Frischknecht, A. L.; Winey, K. I. *In Preparation*.

53. Opper, K. L.; Fassbender, B.; Brunklaus, G.; Spiess, H. W.; Wagener, K. B. *Macromolecules* **2009,** 42, (13), 4407-4409.

54. Opper, K. L.; Markova, D.; Klapper, M.; Mullen, K.; Wagener, K. B. *Macromolecules* **2010,** 43, (8), 3690-3698.

55. Aitken, B. S.; Buitrago, C. F.; Heffley, J. D.; Lee, M.; Gibson, H. W.; Winey, K. I.; Wagener, K. B. *Macromolecules* **2012,** 45, 681-687.

56. Galperin, D.; Khalatur, P. G.; Khokhlov, A. R., Morphology of Nafion Membranes: Microscopic and Mesoscopic Modeling. In *Device and Materials Modeling in PEM Fuel Cells*, Paddison, S. J.; Promislow, K. S., Eds. Springer: New York, 2009; Vol. 113, pp 453-483.

57. Wong, C.; Clarke, J. H. R. *J. Chem. Phys.* **2002,** 116, (15), 6795-6802.

58. Ayyagari, C.; Bedrov, D.; Simith, G. D. *Polymer* **2004,** 45, (13), 4549-4558.

59. Hall, L. M.; Stevens, M. J.; Frischknecht, A. L. *Phys. Rev. Lett.* **2011,** 106, (12).

60. Hall, L. M.; Seitz, M. E.; Winey, K. I.; Opper, K. L.; Wagener, K. B.; Stevens, M. J.; Frischknecht, A. L. *J. Am. Chem. Soc.* **2012,** 134, (1), 574-587.

61. Bolintineanu, D. S.; Stevens, M. J.; Frischknecht, A. L. *ACS Macro Lett.* **2013,** 2, (3), 206-210.

62. Bolintineanu, D. S.; Stevens, M. J.; Frischknecht, A. L. *Macromolecules* **2013**, DOI: 10.1021/ma400848m.

63. Buitrago, C. F.; Alam, T. M.; Opper, K. L.; Aitken, B. S.; Wagener, K. B.; Winey, K. I. *Macromolecules*, Submitted.

64. Goswami, M.; Kumar, S. K.; Bhattacharya, A.; Douglas, J. F. *Macromolecules* **2007,** 40, (12), 4113-4118.

65. Vanhoorne, P.; Register, R. A. *Macromolecules* **1996,** 29, (2), 598-604.

66. Colby, R. H.; Zheng, X.; Rafailovich, M. H.; Sokolov, J.; Peiffer, D. G.; Schwarz, S. A.; Strzhemechny, Y.; Nguyen, D. *Phys. Rev. Lett.* **1998,** 81, (18), 3876-3879.

67. Hall, L. M.; Stevens, M. J.; Frischknecht, A. L. *Macromolecules* **2012,** 45, (19), 8097-8108.

68. Buitrago, C. F.; Opper, K. L.; Wagener, K. B.; Winey, K. I. *ACS Macro Lett.* **2012,** 1, (1), 71-74.

69. Buitrago, C. F.; Jenkins, J. E.; Opper, K. L.; Aitken, B. S.; Wagener, K. B.; Alam, T. M.; Winey, K. I. *Macromolecules*, Submitted.

Chapter 2

A Precise Acid Copolymer Exhibits a Face-Centered Cubic Structure

2.1 Introduction

Acyclic diene metathesis (ADMET) polymerization has produced the first family of precise acid copolymers[1,2] and ionomers.[3] These precise materials are linear, high molecular weight polyethylenes featuring acid or ionic pendants separated by a specific and constant number of carbon atoms. Precise acid copolymers and ionomers present researchers with unprecedented control over the molecular structure of polyethylenes functionalized with polar moieties, which in turn allows for a thorough investigation of the factors controlling the resulting morphologies and properties.

Baughman et al.[1] published room temperature X-ray scattering data for linear polyethylene with precisely placed carboxylic acid groups and reported a set of new higher-order scattering peaks corresponding to the separation between carboxylic acid dimers. FTIR and NMR[4] further confirm the presence of acid-acid dimers at room temperature. The distance between acid dimers in the semicrystalline copolymer with a carboxylic acid group on every 21st carbon is 2.53 nm, which is comparable to the length of 21 carbon-carbon bonds in an all-*trans* conformation (2.7 nm). This correlation distance between acid groups decreases systematically as the number of carbons between acid groups decreases. Moreover, in the semi-crystalline acid copolymer the acid dimers are arranged in layers that are perpendicular to the polymer chain, although Baughman et al. were unable to determine if acid layers are positioned inside or on the surface of the

lamellae. The morphologies of these precise acid copolymers were also studied above the melting temperature, where Seitz et al.[3] found a weak X-ray scattering peak indicating smaller separations between acid dimers as expected for an amorphous structure.

In precise polyethylene ionomers partially neutralized with Zn, the ionic groups form ionic aggregates.[3] As the content of Zn cations increased due to higher acid content and/or higher percent of neutralization, the extent of polyethylene crystallinity at room temperature decreased and the ionic aggregates persisted about the melting temperature. However, the most striking observation was when the ionic aggregates were found to assemble on a cubic lattice. Specifically, the precise ionomer with a carboxylic acid on every 9th carbon and partially neutralized with Zn (66 mol%) has a high temperature (120 °C) X-ray scattering profile that is consistent with a body-centered cubic (BCC) packing of aggregates with a radius of ~0.5 nm.[3] That was the first report of ionic aggregates packing into a periodic structure, and it is a direct result of the precision in the parent acid copolymer.

More recently, precise copolymers with phosphonic acid (PA) pendants have been synthesized.[2] In a previous study[5] of branched, randomly substituted polyethylene with PA groups, microphase separation of PA aggregates was demonstrated by DSC and DMA. Microphase separation driven by hydrogen bonding between the PAs reduces the interfacial area between the PA pendants and the non-polar polyethylene. While carboxylic acids have two hydrogen bonding sites and therefore prefer to form dimers, PA groups have three hydrogen bonding sites that could lead to larger assemblies. This chapter depicts the study of a face-centered cubic (FCC) morphology in a linear

polyethylene precisely substituted on every 21st carbon atom with two PA groups. A combination of room and elevated temperature X-ray scattering from isotropic and stretched polymers were critical in identifying the FCC morphology in this precise geminal PA copolymer.

2.2 Experimental Section

2.2.1 Material: Poly(ethylene-*co*-vinylidene phosphonic acid) was polymerized by ADMET chemistry, and its synthesis, molecular characterization, and thermal properties are described elsewhere.[2] The result is a linear, high molecular weight polyethylene M_n = 19.5 kg/mol, PDI = 1.71) precisely functionalized with geminal phosphonic acid groups on every 21st carbon atom. This acid copolymer is shown is Scheme 2.1 and is denoted as p21gPA, where p and g indicate a precise copolymer with geminal substitution.

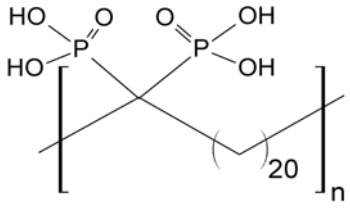

Scheme 2.1 Linear poly(ethylene-*co*-vinylidene phosphonic acid) with geminal phosphonic acid groups on every 21st carbon atom, p21gPA.

2.2.2 Sample Preparation: A p21gPA film for room temperature X-ray scattering was hot-pressed at 150 °C and cooled to room temperature in ambient air. An oriented sample was obtained by drawing a hot-pressed film in hot air and then cooling to room

temperature under tension. Both films were aged at room temperature for 3 days before X-ray scattering experiments at room temperature. For X-ray scattering at 155 °C, a sample was loaded into a sample cell with mica windows.

2.2.3 X-ray Scattering: X-ray scattering was performed using a Nonius FR 591 rotating-anode generator operated at 40 kV and 85 mA. A bright, highly collimated beam was obtained via Osmic Max-Flux optics and triple pin-hole collimation under vacuum. The scattering data were collected using a Bruker Hi-Star multiwire two-dimensional detector with an 11-cm sample-to-detector distance, corresponding to a scattering vector between 1.5 and 8.0 nm^{-1}. The 2-D data reduction and analysis were performed using the Datasqueeze software.[6] For temperature studies, a Linkham oven controlled via a Linkham TMS 94 temperature controller was used. The sample was held at elevated temperatures for at least 1 h prior to data collection to ensure thermal equilibrium. At both thermal conditions, X-ray scattering data were collected for 45 minutes.

2.3 Results and Discussion

2.3.1 One-Dimensional X-ray Scattering at Room Temperature: The one-dimensional X-ray scattering profile of p21gPA at room temperature shows several intense peaks between scattering vectors (q) of 1.5 and 8.0 nm^{-1}, Figure 2.1a. The observed peak breadth in Figure 1a for p21gPA is ~ 0.2 nm^{-1}, as given by the half-width-at-half-maximum. This is comparable to the peak breadth measured for highly crystalline silver behenate over the same q range. Thus, the instrument resolution, rather than the finite crystal size, dominates the observed peak breadth. The first peak at q = 2.6 nm^{-1} has

a shoulder at ~ 3.1 nm^{-1}. Moreover, there are two peaks at 4.8 and 5.1 nm^{-1} that overlap. The q values of these four peaks can be converted to Bragg distances (d) in real space by $d = 2\pi/q$. These peak positions deviate significantly from the two previous cases discussed in the introduction, namely a layered morphology and a BCC lattice of aggregates in precise acid copolymers[1] and ionomers,[3] respectively. In addition, this scattering profile is not consistent with the modified liquid-like scattering model of monodisperse spheres that is widely applied to acid-containing polymers and ionomers.[7]

The multiple scattering peaks for p21gPA agree exceptionally well with the expected reflections from a FCC ordering when the 2.6 nm^{-1} peak is taken as the first allowed reflection. The allowed reflections for a FCC lattice are indicated by their {h k l} Miller indices in Figure 2.1a. The expected {2 2 0} reflection for FCC is not observed. If, as a first approximation, we assume that the PA aggregates form spheres, the aggregate size can be determined by form factor scattering. An aggregate radius (R_{agg}) of 1.1 nm produces a minimum in the spherical form factor scattering that coincides with the missing {220} reflection, Figure 2.1a. One can certainly imagine other ionic aggregate shapes from ellipsoids to strings to 3D continuous periodic structures that might minimize chain stretching. In fact, recent simulated bead-spring polymers with precisely-spaced ionic groups have found both discrete, globular aggregates and percolated, string-like aggregates depending on the details of the molecular architectures.[8] For the remainder of this chapter, the underlying assumption of spherical aggregates will be maintained.

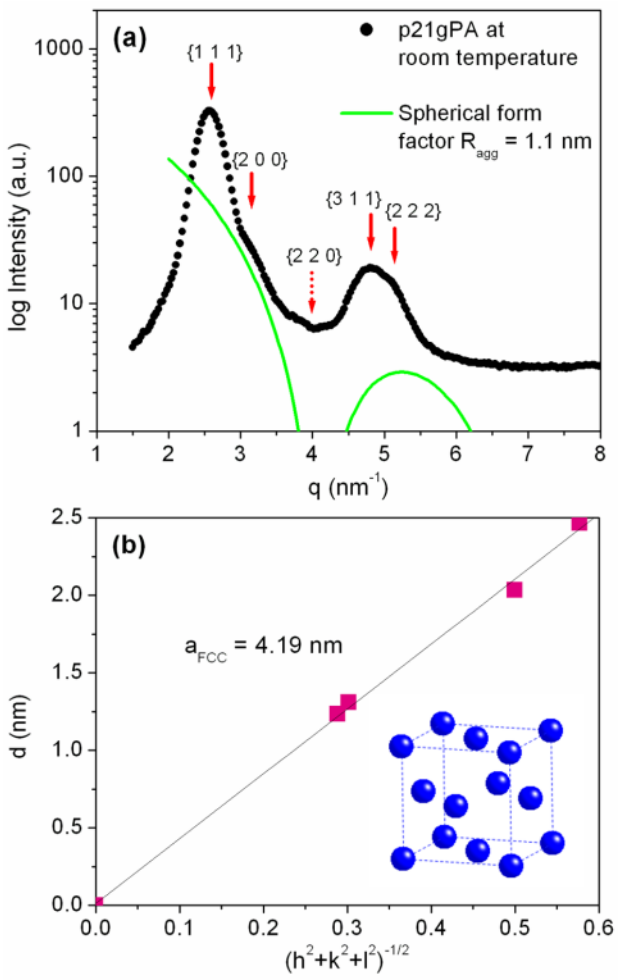

Figure 2.1 (a) X-ray scattering intensity as a function of q for p21gPA at room temperature. The arrows indicate the peak positions corresponding to the allowed reflections from a FCC lattice with a lattice parameter of a_{FCC} = 4.19 nm. The green line is the spherical form factor for acid aggregates of radius R_{agg} = 1.1 nm. (b) The measured Bragg distances from X-ray scattering as a function of the assigned Miller indices. The best-fit line uses Equation 2.1 to determine a_{FCC}. The inset shows a FCC lattice, but note that the acid aggregates in blue are shown smaller than experimentally determined for clarity.

Using the experimentally observed Bragg distances (d) and the Miller indices, the FCC lattice parameter was determined using:

$$d = \frac{a_{FCC}}{\sqrt{h^2 + l^2 + k^2}} \tag{2.1}$$

The data in Figure 2.1b correspond to a FCC lattice with a_{FCC} = 4.19 ± 0.03 nm. Given this lattice parameter, the center-to-center distance between aggregates is 2.96 nm, which is larger than the aggregate diameter (2.2 nm), as expected. The data presented in Figure 2.1 demonstrates that at room temperature phosphonic acid groups in p21gPA microphase separate and assemble on a FCC lattice in an amorphous polyethylene matrix.

The 1.1 nm aggregate radius, which was approximated by matching a spherical form factor minimum with the missing peak in the scattering data, can be evaluated by comparing the volume fraction of acid aggregates based on the FCC structure (ϕ_{FCC}) and the volume fraction of acid groups calculated based on stoichiometry (ϕ_{stoi}).

$$\phi_{FCC} \equiv \frac{4 \cdot \left(4/3 \cdot \pi \cdot R_{agg}^3\right)}{a_{FCC}^3} \tag{2.2}$$

$$\phi_{stoi} = \frac{2V_{PA}}{V_{p21gPA}} \tag{2.3}$$

In Equation 2.3, V_{PA} is the volume of a PA pendant, V_{p21gPA} is the volume per repeating unit of p21gPA, and the factor of 2 reflects the geminal functionalization. These volumes were calculated from the molecular weight of the monomeric unit and the densities of amorphous polyethylene ($\rho_{PE,\ amorphous}$ = 0.855 g/cm^3)[9] and pure phosphonic acid (ρ_{PA} = 1.23 g/cm^3).[10] The volume fractions calculated from the proposed morphology and the chemical stoichiometry are in good agreement: ϕ_{FCC} = 0.30 and ϕ_{stoi} = 0.28. This analysis

further supports the FCC unit cell. However, an aggregate of R_{agg} = 1.1 nm contains 25 geminal PA groups, as found by dividing the volume of one aggregate by V_{PA}. This aggregation number appears to be inconsistent with our assumption of spherical aggregates and thereby suggests an alternative aggregate shape with form factor scattering similar to a sphere. Regardless of the aggregate shape, the lattice symmetry is FCC.

2.3.2 Two-Dimensional X-ray Scattering at Room Temperature: The one-dimensional scattering data in Figure 2.1a were obtained from an isotropic p21gPA film that gave uniform scattering rings at the two-dimensional X-ray scattering detector. Figure 2.2a is the two-dimensional X-ray scattering profile of a p21gPA sample stretched in the direction of the arrows. This anisotropic scattering pattern is analyzed in Figure 2.2b by plotting the intensity as a function of azimuthal angle at the four q positions corresponding to FCC peak positions. At the lowest q (2.6 nm^{-1}) corresponding to the {1 1 1} family of planes, four strong peaks are evident at azimuthal angles of 36°, 144°, 215° and 322°. In addition, two weaker {1 1 1} scattering points are detected at 90° and 270°. At q = 3.1 nm^{-1}, only two {2 0 0} peaks are observed at 90° and 270°. Both the {3 1 1} and {2 2 2} families of planes at 4.8 and 5.1 nm^{-1}, respectively, have four peaks the maxima of which are slightly different. The {2 2 2} family has peaks at the same angles as the {1 1 1}, while the {3 1 1} are at 27°, 153°, 206° and 331°.

These experimental results are compared to single crystal scattering patterns for a FCC lattice with a_{FCC} = 4.19 nm simulated using CrystalMaker®. Figures 2.2c and 2.2d show the expected calculated patterns when the X-ray beam is along the [1 1 0] and the

[1 2 1] crystallographic directions, respectively. Note that the reflections corresponding to the diffraction patterns in Figures 2.2c and 2.2d are indicated in Figure 2.2b with black and red dots, respectively. The four {1 1 1} peaks with two-fold symmetry in Figure 2.2c correspond to the strongest peaks in the experimental data. The two meridional {1 1 1} peaks in Figure 2.2d are consistent with the weaker {1 1 1} peaks in Figure 2.2b. The observed {2 0 0} and {2 2 2} peaks correspond to the single crystal scattering position in Figure 2.2c, while the experimental {3 1 1} peaks match the pattern in Figure 2.2d. The allowed {2 2 0} reflections in the single crystal diffraction patterns are shown in Figures 2.2c and 2.2d, but are missing in Figure 2.2a, because as discussed for the isotropic scattering data the {2 2 0} reflections coincide with a minimum in the spherical form factor.

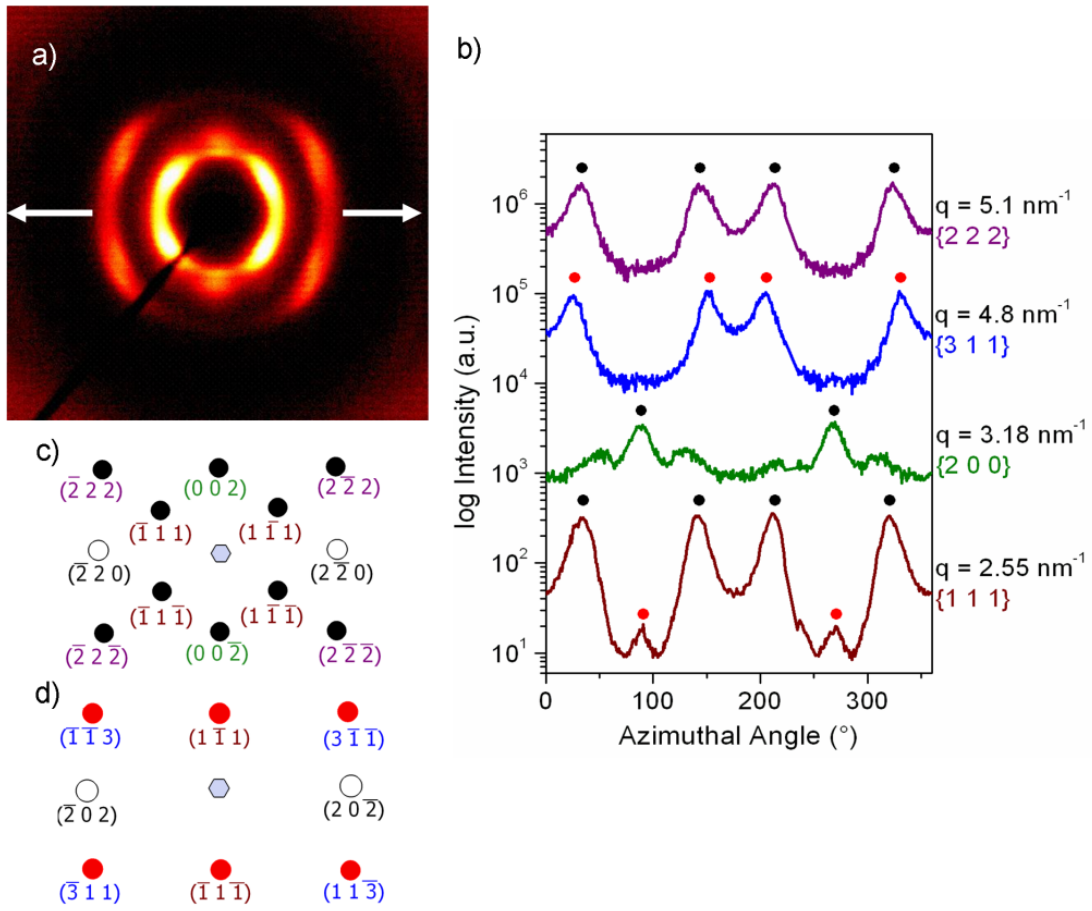

Figure 2.2 (a) Room temperature X-ray scattering data from a stretched film of p21gPA, where the arrows indicate the stretch direction and correspond to the <1 1 0> direction. (b) X-ray scattering intensity as a function of azimuthal angle extracted from (a) and the specified *q* values. Simulated diffraction patterns for single crystal FCC lattices when the beam is along the [1 1 0] direction (c) and along the [1 2 1] direction (d). The expected {2 2 0} points, which are not observed in the data due to a minimal in the form factor scattering, are represented as open circles. Black and red dots in (b) indicate whether the observed diffraction peak corresponds to the crystal orientation in (c) or (d), respectively.

In summary, the experimental X-ray scattering pattern from a stretched film of p21gPA is consistent with two coexisting FCC crystal orientations. These two crystal orientations have a common direction, namely the <1 1 0> direction, that is parallel to the stretch direction. These two crystal orientations were found to coexist across the stretched film and were found repeatedly when new films were stretched.

2.3.3 One-Dimensional X-ray Scattering at Elevated Temperature: Finally, X-ray scattering on isotropic p21gPA was performed at 155 °C, a temperature well above the reported T_m of this acid copolymer.[2] Figure 2.3 shows the one-dimensional X-ray scattering profile. X-ray scattering data at elevated temperature and room temperature are comparable with peak assignments consistent with a FCC lattice. The lattice parameter at 155 °C as determined using Equation 2.1 is 4.06 ± 0.03 nm, just 3% smaller than the room temperature lattice parameter. The cubic ordering of the PA aggregates in p21gPA clearly persists at elevated temperature, which confirms that the reported T_m corresponds to crystallization in the polyethylene matrix rather than ordering of the FCC lattice of aggregates. This observation is in marked contrast to the precise mono-substituted carboxylic acid copolymers wherein the hierarchical structure of layered acid dimers deteriorates significantly when the temperature was raised from room temperature to 120 °C.[3]

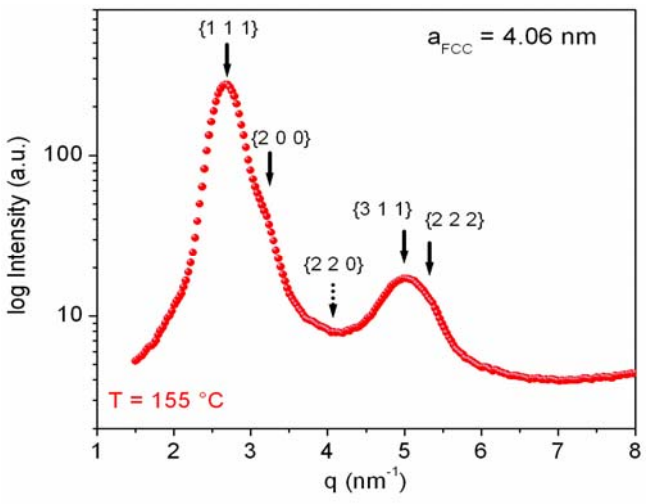

Figure 2.3 (a) X-ray scattering intensity as a function of q for p21gPA at 155 °C. Arrows indicate the allowed reflections for an FCC lattice with a_{FCC} = 4.06 nm. The {2 2 0} reflection is absent due to a minimum in the form factor for a sphere with R_{agg} = 1.1 nm.

2.4 Conclusions

The synthesis of linear polyethylene with pendant acid or ionic groups precisely spaced along the polymer chain has resulted in materials with hierarchical morphologies.[1,3] In this instance, X-ray scattering shows that geminal phosphonic acid substitution on the 21st carbon produces microphase separation with acid aggregates on a FCC lattice. This morphology persists at elevated temperature and the <1 1 0> crystal direction aligns with the stretch direction. This marks the first report of cubic packing in precise polyethylene-based acid copolymers.

2.5 References

1. Baughman, T. W.; Chan, C. D.; Winey, K. I.; Wagener, K. B. *Macromolecules* **2007,** 40, (18), 6564-6571.

2. Opper, K. L.; Markova, D.; Klapper, M.; Mullen, K.; Wagener, K. B. *Macromolecules* **2010,** 43, (8), 3690-3698.

3. Seitz, M. E.; Chan, C. D.; Opper, K. L.; Baughman, T. W.; Wagener, K. B.; Winey, K. I. *J. Am. Chem. Soc.* **2010,** 132, (23), 8165-8174.

4. Alam, T. M.; Jenkins, J. E.; Seitz, M. E.; Buitrago, C. F.; Winey, K. I.; Opper, K. L.; Baughman, T. W.; Wagener, K. B., ^{1}H MAS NMR spectroscopy of polyethylene acrylic acid copolymers and ionomers. In *NMR Spectroscopy of Polymers: Innovative Strategies for Complex Macromolecules*, Cheng, H. N.; Asakura, T.; English, A. D., Eds. American Chemical Society: Washington, DC, 2011; Vol. 1077, pp 115-131.

5. Phillips, P. J.; Emerson, F. A.; MacKnight, W. J. *Macromolecules* **1970,** 3, (6), 767-771.

6. Heiney, P. A. *Commission on Powder Diffraction Newsletter* **2005,** 32, 9-11.

7. Kinning, D. J.; Thomas, E. L. *Macromolecules* **1984,** 17, 1712-1718.

8. Hall, L. M.; Stevens, M. J.; Frischknecht, A. L. *Phys. Rev. Lett.* **2011,** 106, (12).

9. Brandrup, J.; Immergut, E. H., *Polymer Handbook*. John Wiley & Sons: New York, 1989.

10. Roy, S.; Ataol, T. M.; Muller-Plathe, F. *J. Phys. Chem. B* **2008,** 112, (25), 7403-7409.

Chapter 3

Morphology Trends in Precise Acid- and Ion-Containing Polymers at Elevated Temperature

3.1 Introduction

Polyethylene (PE) is the most prevalent synthetic polymer in the world due to its cost effectiveness, ease of production and range of available properties.[1] From a fundamental molecular point of view, linear PE is the simplest polymer chain and it is often used as the starting point for studies in polymer physics, particularly crystallization. From the structural simplicity of linear PE, alkyl pendant groups are the first step toward greater molecular complexity for the study of morphological and property variations.[2-4] By including polar or ionic pendant groups capable of secondary bonding, the morphologies and properties of PE-based copolymers become particularly interesting due to the propensity of the pendants to form physical crosslinks and microphase separate in the non-polar PE matrix.[5-11] These PE-based copolymers often yield improved adhesion, mechanical toughness, thermal stability and chemical resistance.[1, 5]

Most studies addressing the morphology and properties of PE-based copolymers with polar substituents have been carried out in materials that are far from ideal in that they are often highly branched and randomly functionalized with an uncontrolled number of carbon atoms between the pendant groups.[5-13] In 2007, the first report of a family of high molecular weight, precise copolymers of PE and acrylic acid (AA) resulting in carboxylic acid pendants was published.[14] Acyclic diene metathesis (ADMET)

polymerization was the synthetic route used to achieve this milestone, which yields copolymers with unprecedentedly well-defined morphologies.[14,15] More recently, the use of ADMET polymerization has been successfully extended to synthesize precise copolymers featuring phosphonic acid (PA)[16] and 1-methylimidazolium bromide (ImBr)[17] pendants, Figure 3.1.

Pendant Groups	Polymer Architecture
a. Carboxylic Acid (AA copolymer) 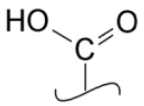	d. Precise Mono 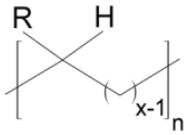 x = 9, 15 or 21
b. Phosphonic Acid (PA) 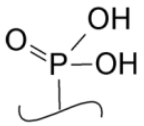	e. Precise Geminal 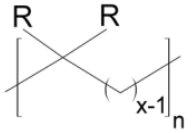 x = 15 or 21
c. 1-Methylimidazolium Bromide (ImBr) 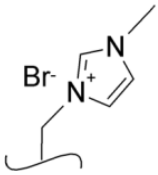	f. Pseudo-random 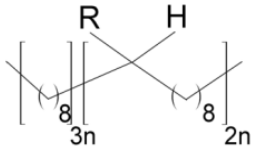

Figure 3.1: Pendant groups and polymer architectures of polyethylene-based copolymers.

The differences in morphologies and properties expected from precise copolymers with AA, PA and ImBr groups originate from the inherent differences of the pendants. For example, AA has only two hydrogen bonding sites compared to the three sites of PA, which could produce larger or more complex assemblies. In addition, PA is a stronger acid than AA (pKa = 2 vs. 5, respectively), and PA has been found to act as both a proton donor and acceptor.[18] These characteristics affect the ability of the polar groups to form larger microphase separated aggregates and to incorporate water molecules into the microdomains. The volume fraction (ϕ) of the pendant groups, another key parameter, can be estimated from the molecular weights and densities, and PA occupies nearly twice the volume of AA, as will be shown later in this study. Therefore, AA and PA copolymers with the same molar compositions can have dramatically different morphologies due to the differences in the volume fraction of the polar groups. In the case of ImBr, the positively charged imidazolium groups are covalently bonded to the linear PE chains and neutralized by Br anions. Therefore, although the ImBr groups are polar as are the acid pendants, these materials are ion-containing polymers or ionomers. A crystallographic study of 1-ethyl-3-methylimidazolium bromide (a small molecule equivalent of the ImBr pendant plus the methylene group linking it to the polymer backbone) reveals that each imidazolium ring can simultaneously form hydrogen bonds with three bromide anions.[19] Moreover, given that the size of the ImBr pendant group is nearly twice that of the PA pendant group, the ImBr copolymer morphologies are also

expected to differ considerably from the AA and PA copolymers at fixed molar concentrations.

There is growing evidence from molecular dynamics simulations that the microphase separated aggregates in acid-containing copolymers and ionomers assume non-spherical shapes. Such simulations typically correspond to either elevated temperature or high dielectric constant to promote polymer mobility and avoid polymer crystallization, and thus are pertinent to the current study. Hall *et al.* found discreet and percolated aggregates using coarse-grained molecular dynamics (MD) simulations for different chain architectures.[20,21] Using a nonpolarizable united-atom force field, Lin and Maranas' MD simulations of a Na-neutralized ionomer produced ion clusters in chain-like structures.[22] Finally, Bolintineanu *et al.* recently applied atomistic MD to explore ionic aggregates in precise AA copolymers neutralized with Li^+, Na^+, Cs^+, or Zn^{2+} cations and found a variety of shapes including compact isolated aggregates, branched string-like aggregates, and percolated structures.[23,24] When scattering profiles are computed from these simulations, the characteristic low angle peak is present. Interestingly, the scattering is seemingly unaffected by the significant changes in the aggregates' shape and size, although the peak position correlates well with nominal interaggregate spacings. While extracting aggregate size and shape information form X-ray scattering is an ongoing effort in our group, here we focus on the interaggregate spacing without specifying the shape or size of the aggregates.

In this chapter, a comprehensive study of the morphologies of precise AA, PA and ImBr copolymers at elevated temperatures via X-ray scattering is presented. In

Chapter 4, we report the morphologies of these copolymers at room temperature, where the crystallinity of the longer PE spacers significantly impacts the morphologies.[25] At high temperatures, all but one of the AA, PA and ImBr precise copolymers exhibit a liquid-like arrangement of microphase separated acid-rich or ion-rich aggregates within an amorphous PE-rich matrix. To illustrate the dramatic effect of precise pendant placement on the main polymer chain, the morphology of linear, pseudo-random copolymers (Figure 3.1f) also synthesized via ADMET will be presented. The polymer morphology of the precise copolymers will be considered as a function of carbon sequence length between pendant groups, size and volume fraction of the pendant species, and functional group configuration (single or geminal).

3.2 Experimental Section

3.2.1 Materials: Linear polyethylenes precisely functionalized with pendant groups on every 9th (22.2 mol% of the pending species), 15th (13.3 mol%) and 21st (9.5 mol%) carbon along the main chain were synthesized via ADMET polymerization. The synthesis, characterization and thermal properties of these copolymers with acrylic acid (AA),[14] phosphonic acid (PA),[16] and 1-methylimidazolium bromide (ImBr)[17] have been previously reported. A newly synthesized precise, geminal AA material is introduced in this article.

A complete list of the precise copolymers studied, along with their nomenclature is shown in Table 3.1. The nomenclature scheme is as follows. The letter *p* indicates the precise placement of pendant groups along the polymer chain. This is followed by a

number (x = 9, 15 or 21) that specifies the precise sequence of carbon atoms per pendant substitution, Figure 3.1d. For materials with two pendant groups on each functionalized carbon, the letter *g* is included to designate geminal substitution, Figure 3.1e. Finally, the copolymers are denoted as AA, PA or ImBr, Figure 3.1a-c. Note that for the acrylic acid (AA) copolymers, the pendant groups are carboxylic acids. Three pseudo-random materials synthesized via ADMET copolymerization of symmetric diene monomers and 1,9-decadiene[16,17] were also studied and their molecular structures are shown in Figure 3.1f. The letter *r* replaces *p* to indicate pseudo-random substitution and the number 21 denotes that, on average, there is one pendant per 21 carbon atoms, which makes it compositionally identical to its precise counterpart (9.5 mol% of the pendant species). Finally, two small alkanes with symmetrical substitutions of single or geminal PA were studied. These molecules are analogous to the monomeric repeat units of p21PA and p21gPA. They are denoted as 11,11PA and 11,11gPA, indicating that two *n*-undecanes are bonded to single- and geminal-substituted carbons, respectively.

Table 3.1 Nomenclature, Pendant Volume Fractions and Characteristic Lengths from X-ray Scattering for Twelve Precise Copolymers at $T > T_m$

Material	Pendant Vol. Fraction ($\phi_{pendant}$)	X-ray Scattering	
		T (°C)	d* (nm)
p9AA	0.20	120	1.05
p15AA	0.13	120	1.50
p21AA	0.10	120, 150	1.65, 1.63
p21gAA	0.18	120	1.80
p9PA	0.31	150	1.39
p15PA	0.21	150	1.75
p15gPA	0.35	150	2.01
p21PA	0.16	150	2.05
p21gPA	0.25	150	2.39 (a_{FCC} = 4.06)
p9ImBr	0.48	120	1.65
p15ImBr	0.36	120, 150	2.12, 2.10
p21ImBr	0.29	120	2.55

The volume fraction of the acid or ionic pendant groups ($\phi_{pendant}$) in each precise copolymer at elevated temperature ($T > T_{m,\,PE}$) was estimated using the general equation

$$\phi_{pendant} = \frac{N_{pendant} * V_{pendant}}{\left(N_{pendant} * V_{pendant}\right) + V_{PE}} \tag{3.1}$$

where $N_{pendant}$ reflects the number (1 or 2) of pendants per functionalized carbon, $V_{pendant}$ is the volume of one pendant, and V_{PE} is the volume corresponding to the amorphous PE spacer. $V_{pendant}$ and V_{PE} were calculated using the molecular weight and liquid density of

carboxylic acid (1.22 g/cm^3),[26] PA (1.23 g/cm^3),[27] ImBr (1.28 g/cm^3)[28] and amorphous PE (0.855 g/cm^3).[26] Volume fractions are reported in Table 1.

3.2.2 X-ray Scattering: For the AA and ImBr copolymers, samples were loaded into 1.0 mm diameter glass capillaries (Charles Supper Co. Special Glass 10-SG) which were then flame-sealed. X-ray scattering was performed in the Multi-angle X-ray Scattering (MAXS) Facility at the University of Pennsylvania using a Nonius FR591 rotating-anode generator operated at 40 kV and 85 mA. A bright, highly collimated beam was obtained via Osmic Max-Flux optics and triple pinhole collimation under vacuum. The scattering data were collected for 30 minutes using a Bruker Hi-Star multiwire two-dimensional detector at a sample-to-detector distance of 11 cm. The sample temperature was raised and maintained by a Linkham oven controlled via a Linkham TMS 94 temperature controller. The samples were heated to 120 °C and allowed to reach thermal equilibrium for 5 minutes prior to data collection.

For the PA copolymers, synchrotron X-ray scattering was conducted at beamline 5ID-D (DND-CAT) of the Advanced Photon Source (APS) at Argonne National Laboratory to improve the resolution of the relatively weak high-order scattering peaks. Two-dimensional data were collected using a Gemstar CCD detector at a sample-to-detector distance of 325.4 mm and X-ray energy of 17 keV. Collection times ranged from 0.5 to 10.0 seconds depending on the scattering intensity of the samples and to avoid saturation of the detector. The samples were loaded into aluminum DSC pans, and their temperature was controlled using a Linkham oven programmed to ramp from -40 to 150 °C at 10 °C/min and hold at 150 °C for 5 minutes. Two-dimensional data reduction and

analysis of data collected at the MAXS facility and APS were performed using the Datasqueeze software.[29]

All X-ray scattering data were collected well above the highest thermal transition (T_g, T_m) for all the copolymers.[14,16,17] The scattering profiles for the single AA copolymers had been previously published at 120 °C by Seitz *et al.* and are included here for effective comparison to the geminal AA, PA and ImBr copolymers.[15] For the PA copolymers, X-ray data were collected at 150 °C (the highest recommended temperature in air) to ensure the attainment of equilibrium melt morphologies, as their melting endotherms (manifested as double or extremely broad peaks) span temperature ranges as wide as 100 °C.[16] On the other hand, 120 °C was an appropriate collection temperature for the ImBr copolymers, which exhibited fast and complete melting at this temperature by DSC and DMA.[17] There is no significant temperature dependence in the inter-aggregate correlation peak (q^*) above the thermal transitions. For example, Table 3.1 reports the *d*-spacings ($d^* = 2\pi/q^*$) for p21AA and p15ImBr at 120 °C and 150 °C to vary by only ~ 1%. Therefore, morphological comparisons will be made between these materials irrespective of the temperatures (120 °C or 150 °C). In addition, variable elevated temperature studies where conducted on PA and ImBr samples up to 180 °C and found negligible differences in the intensity, shape and position of the ionomer peaks above the thermal transitions of the materials, see Figure B.1 in Appendix B.

3.3 Results and Discussion

3.3.1 Acid- and Ion-Rich Aggregates: The X-ray scattering profiles for eleven precise copolymers collected at elevated temperatures exhibit two peaks, Figure 3.2a. The peaks at $q \sim 14$ nm^{-1} correspond to the polyethylene amorphous halo. While room temperature solid-state ^{13}C NMR found ~44% of the backbone methylene groups of p21AA to be in the orthorhombic all-*trans* conformation and 0% for p9AA and p15AA, at the elevated temperatures ($T > T_m$) studied here, the PE segments are expect to be fully amorphous.[30] The low-angle X-ray scattering peaks at $q^* \sim 2 - 7$ nm^{-1} in acid- and ion-containing polymers arise from microphase separation of the acid or ionic groups into aggregates (Figure 3.2a). Additional experimental methods also provide evidence of microphase separation of the polar groups in PE-based copolymers. For the precise AA copolymers, FTIR[14] and ^{1}H NMR[31] show that all the carboxylic acid groups hydrogen bond with at least one other pendant. For PE-based PA copolymers, Phillips et al. showed through DMA and dielectric spectroscopy the formation of PA-rich regions.[12,32] For the precise ImBr ionomers, two thermo-mechanical transitions were detected by DMA, one for the PE matrix and another one for the ImBr regions.[17] The scattering intensity of the aggregate peaks is strongly dependent on the electron density contrast between the polar pendants and the PE matrix. For this reason, the AA copolymers show relatively weak scattering arising from the carboxylic acid pendants, whereas the PA and ImBr copolymers have more electron density contrast due to the presence of phosphorous and bromine atoms, respectively. Earlier studies have compared X-ray scattering from precise and pseudo-random AA copolymers at 120 °C and found that precise carboxylic acid

placement is required to produce a low angle scattering peak, because the precise copolymer architecture dictates a well-defined interaggregate spacing.[15]

The aggregates appear to have liquid-like order, although as discussed above the scattering data is insufficient to specify the shape or size of the aggregates. The average interaggregate spacings, defined as the center-to-center distances between aggregates, are extracted from the peak position ($d^* = 2\pi/q^*$) and recorded in Table 3.1 and Figure 3.2b. In contrast, at room temperature some of these precise copolymers exhibit multiple higher-order peaks associated with long-range order imposed by the semi-crystallinity of the PE segments.[14,15,25] To date, the only precise acid copolymer that maintains long-range order at elevated temperatures is p21gPA, which exhibits a face-centered cubic (FCC) packing of aggregates at 155 °C (the highest temperature suitable to avoid oxidation in air).[33] In the other eleven precise copolymers with polar substituent groups (acid or ionic), high temperatures melt any PE crystallites that may be present at room temperature to produce a common morphology type, namely liquid-like order of microphase-separated polar aggregates. The high-temperature condition allows a direct comparison between materials and facilitate an in-depth analysis of the effect of PE spacer length (9, 15 or 21 carbon-carbon bonds), size of the pendant group (carboxylic acid vs. PA vs. ImBr) and molecular architecture (single vs. geminal) on the characteristic lengths (d^*) of the microphase separated systems.

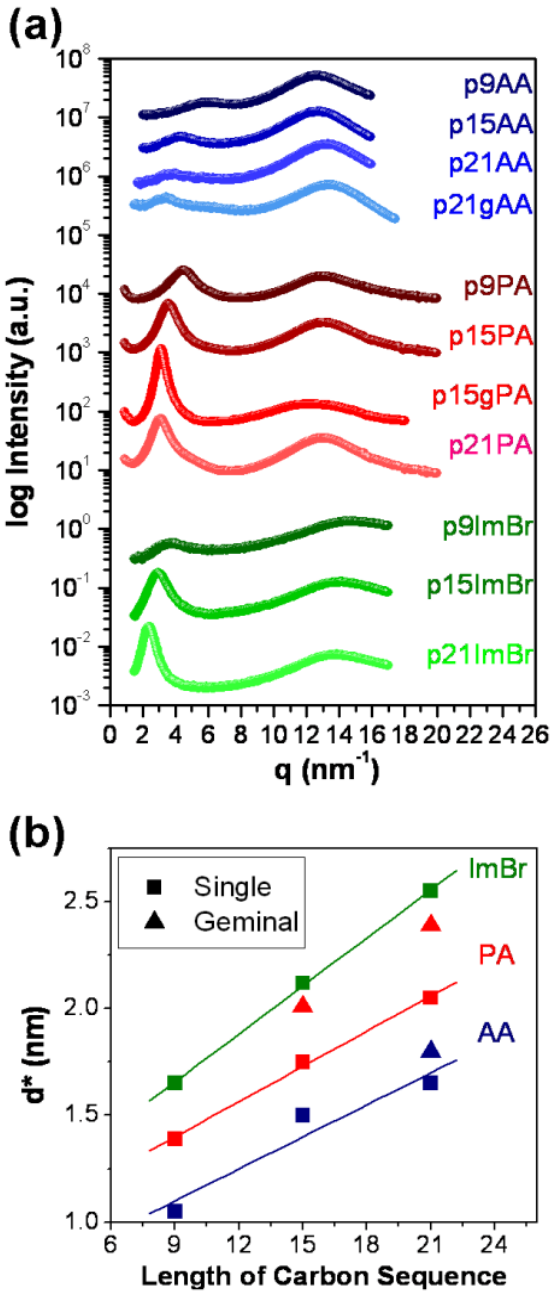

Figure 3.2 (a) Intensity vs. scattering vector (q) for precise AA, PA and ImBr materials exhibiting liquid-like morphologies above their thermal transitions. The curves are shifted vertically for clarity. (b) Characteristic lengths ($d^* = 2\pi/q^*$) determined from the low-angle peak as a function of PE spacer.

Within materials functionalized with the same pendant group, a clear trend in the evolution of the aggregate peak is observed in terms of position and sharpness. As expected, the peak positions shift toward higher q^*s (and consequently to smaller d^*s) as the PE spacer between pendants decreases from 21 to 15 to 9 carbon-carbon bonds, Figure 2b. This observation was previously reported for precise AA copolymers and Zn-neutralized AA ionomers.[15] Note that d^* systematically increases in the mono-substituted precise copolymers as the polar groups change from carboxylic acid to PA to ImBr, and geminal-substitution increases d^* relative to the corresponding mono-substitution, Figure 2b. Both Table 1 and Figure 2b include the correlation length of p21gPA, which exhibits an ordered arrangement of PA-rich aggregates rather than the liquid-like order observed in the other precise copolymers. The aggregate peaks in copolymers functionalized on every 21st and 15th carbons are also sharper than the peaks for the materials with pendants every 9th carbons. The sharpness of scattering peaks is inversely associated to the distribution of d-spacings between scatterers. Sharp scattering peaks in materials with pendants on every 21st and 15th carbon indicate that the aggregates have a narrower distribution of inter-aggregate separations. As the number density of functional groups increases and the length of the carbon spacer between polar groups (x) decreases, the polar groups still self-assemble into aggregates, but the uniformity of the liquid-like order decreases. For example, the sharp low-angle peak in p21ImBr ($\phi_{pendant}$ = 0.29) widens noticeably for p15ImBr, and becomes broad and weak for p9ImBr ($\phi_{pendant}$ = 0.48). The mono-substituted AA and PA copolymers also follow this trend.

We use a relative distance to facilitate comparisons between precise copolymers with various spacer lengths, pendant types and mono or geminal substitution. We define the relative distances in copolymers with aggregates that display liquid-like order as the interaggregate spacing ($d^* = 2\pi/q^*$) divided by the length of the PE spacer (21, 15 or 9 carbon-carbon bonds) in the all-*trans* conformation ($l_{\text{all-}trans}$). At the elevated temperatures used in this study ($T > T_g$, T_m), the PE segments assume amorphous conformations rather than all *trans* conformations, but this relative distance is useful for comparing this group of copolymers. Figure 3.3 shows the relative distances for the precise copolymers with mono-substitution as a function of pendant group type and spacer length. Note that the relative distances of p9PA, p9ImBr and p15ImBr exhibit $d^*/l_{\text{all-}trans} > 1$. As schematically illustrated in Figure 4, the interaggregate spacing (d^*) obtained by X-ray scattering, which originates from the center-to-center distance between scatterers (namely the microphase separated aggregates containing the pendant groups), can exceed the fully extended PE spacer ($l_{\text{all-}trans}$) when the volume fraction of the pendant groups is large.

From Figure 3.3 it is apparent that for each PE spacer length (or mol% of the pendant species), the average distance between aggregates increases as the size of the pendant groups increases from carboxylic acid to PA to ImBr. As Figure 3.4 suggests, this trend can be understood in terms of the volume fraction of pendant groups, wherein at a fixed PE spacer and mole fraction of pendant groups the larger pendant groups possess a larger total volume of acid- or ion-rich aggregates that correspond to larger d^*. For example, for mono-substituted precise copolymers with a PE spacer of 21, the pendant volume fraction increase from 0.10 to 0.16 to 0.29 as the pendant changes from

carboxylic acid to PA to ImBr with a corresponding increase in $d^*/l_{\text{all-}trans}$ from 0.62 to 0.77 to 0.95. Additionally, for copolymers with the same pendant group, $d^*/l_{\text{all-}trans}$ increases as the PE spacer length decreases corresponding to an increase in mol %. This may be counterintuitive considering the trend illustrated in Figure 3.2b where the interaggregate spacings d^* increase with the PE spacer length (as mol% decreases). However, for a fixed pendant group decreasing the PE spacer increases the pendant volume fraction that drives an increase in the relative distance. For example, for mono-substituted precise copolymers with PA pendant groups, the pendant volume fraction increase from 0.16 to 0.21 to 0.31 as the PE spacer decreases from 21 to 15 to 9 with a corresponding increase in $d^*/l_{\text{all-}trans}$ from 0.77 to 0.91 to 1.2. Moving beyond these trends in the interaggregate spacing as a function of PE spacer length, pendant group type, and volume fraction of pendant groups requires a detailed knowledge of the aggregate shape and shape diversity, as well as how the aggregate shape might change with these parameter.

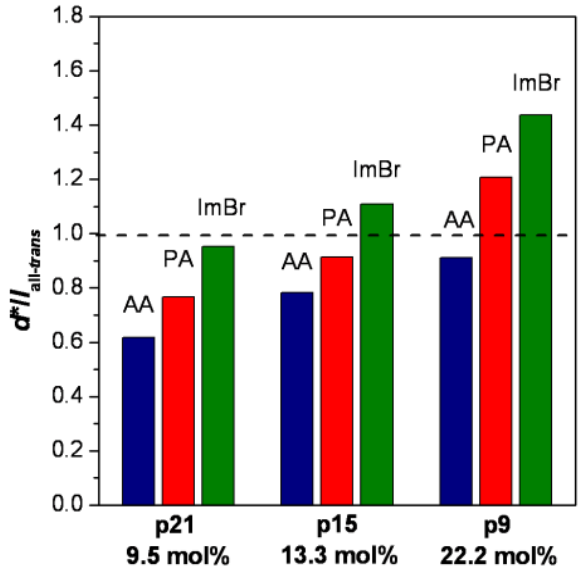

Figure 3.3 The effect of pendant size on the relative distance of mono-substituted precise AA, PA and ImBr copolymers at elevated temperature. The relative distances are the *d**-spacings from Figure 2b divided by the length of 9, 15 or 21 carbon-carbon bonds in all-*trans* chain conformation.

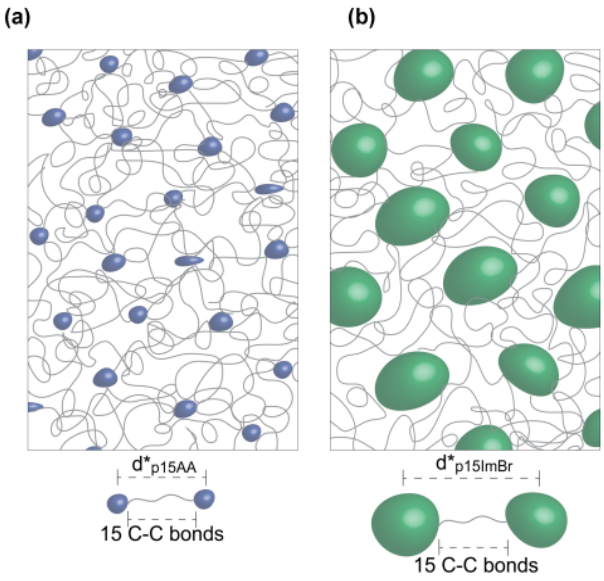

Figure 3.4 Schematic of amorphous (a) p15AA (ϕ= 0.13) and (b) p15ImBr (ϕ= 0.36). The colored shapes depict globular, discrete aggregates, not individual pendant groups. Although the PE spacer between pendants is the same (15 C-C bonds), the higher volume fraction in p15ImBr produces a substantially larger interaggregate, center-to-center distances (d^*), such that $d^*/l_{\text{all-}trans}>1$.

3.3.2 Mono and Geminal Configurations: The effect of geminal substitution on $d^*/l_{\text{all-}trans}$ is examined in Figure 3.5. At fixed PE spacer length and pendant type, the geminal-substituted precise copolymers have twice the number of pendant groups in the monomeric unit relative to the mono-substituted precise copolymers, consequently more and/or larger aggregates are expected to form. For p21gAA, p21gPA and p15gPA, $d^*/l_{\text{all-}trans}$ increases slightly compared to p21AA, p21PA and p15PA, strongly suggesting that the aggregates increase in size. This is consistent with the discussion above that correlates an increase in $d^*/l_{\text{all-}trans}$ to increases in pendant volume fraction. Further, for the PA

copolymers substituted on every 15th carbon atom, the stronger scattering intensity of p15gPA (Figure 3.2) implies that geminal substitution causes an increase in both size and number density of the aggregates.

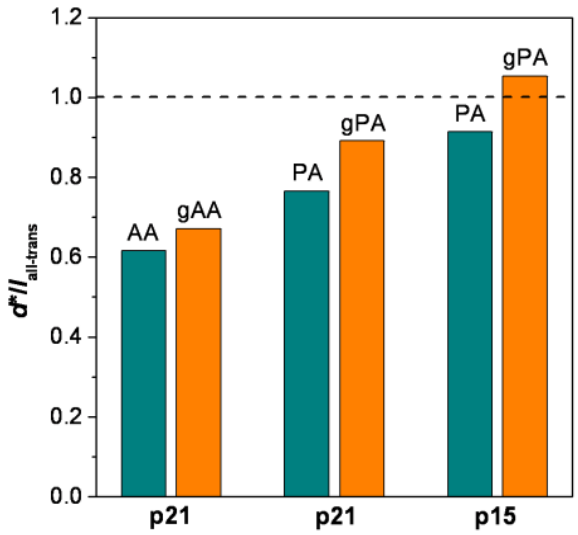

Figure 3.5 The effect of geminal substitution on the relative distance in AA and PA precise copolymers at elevated temperature. Note that p21gPA has FCC symmetry, but d^* is extracted from the main scattering peak and corresponds to the interaggregate spacing.

The amorphous halo (the broad feature between q = 9 – 17 nm^{-1}) is associated with scattering from correlations between polymer backbones and other short-range interactions. The amorphous halo for linear polyethylene, p21AA and p21gAA are quite similar at elevated temperature, Figure 3.6. In contrast, the geminal PA precise copolymers (p15gPA and p21gPA) exhibit amorphous halos significantly different from

the conventional shape exhibited by the single PA copolymers, Figure 3.6. Unlike p21gAA, which has a symmetrical amorphous halo with a maximum at ~14 nm^{-1} corresponding to ~ 0.45 nm, both geminal PA materials exhibit two overlapping characteristic length scales in the amorphous halo between 10 and 12 nm^{-1}. This binary amorphous halo suggests that two characteristic length scales are dominant in the amorphous region of the geminal PA materials: 0.47 and 0.54 nm.

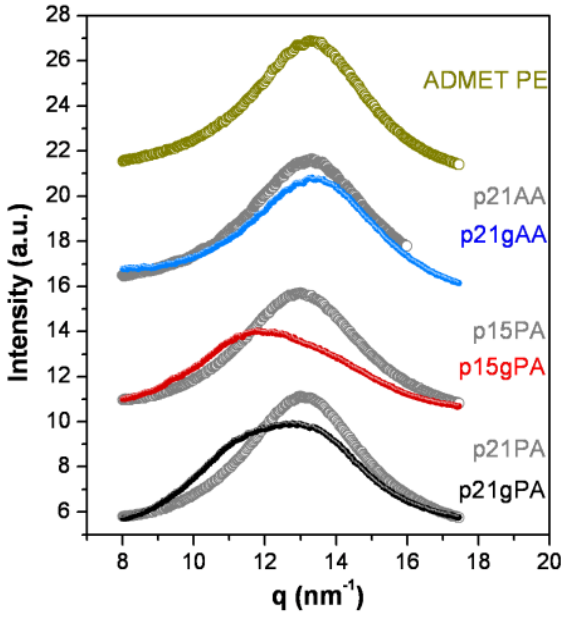

Figure 3.6 Wide-angle X-ray scattering at elevated temperature comparing the structure in the amorphous PE regions for single and geminal PA and AA materials. All single copolymers exhibit the typical scattering observed in amorphous PE synthesized via ADMET. The geminal PA copolymers (p21gPA and p15gPA) exhibit two characteristic length scales in the amorphous morphology.

We consider two explanations for the additional local length scale in the geminal PA copolymers. First, the new length scale of 0.54 nm might arise from the correlation distance between PA pendants connected to the same carbon atom. This hypothesis was tested using small molecules, namely 11,11PA and 11,11gPA, with two *n*-undecanes bonded to mono- and geminal-substituted carbons, respectively. These small molecules are liquid at room temperature and analogous to the monomeric repeat units of p21PA and p21gPA. As evident from the X-ray scattering data in Figure 3.7, both 11,11PA and 11,11gPA exhibit a unimodal correlation length at $q \sim 14$ nm^{-1}. Thus, we cannot assign the new correlation length found in p15gPA and p21gPA to a correlation distance between PA groups with geminal substitution. Alternatively, the larger length scale in the amorphous region for p15gPA and p21gPA might arise from a broader distribution in the packing of PE segments due to the steric constraints of geminal substitution. Relative to the geminal AA copolymer with two H-bonding sites per pendant, the PA pendant groups are larger and have three H-bonding sites. Steric hindrances and packing frustrations near the geminal-substituted PA pendant groups could increase local free volume and have interesting implications for local dynamics.

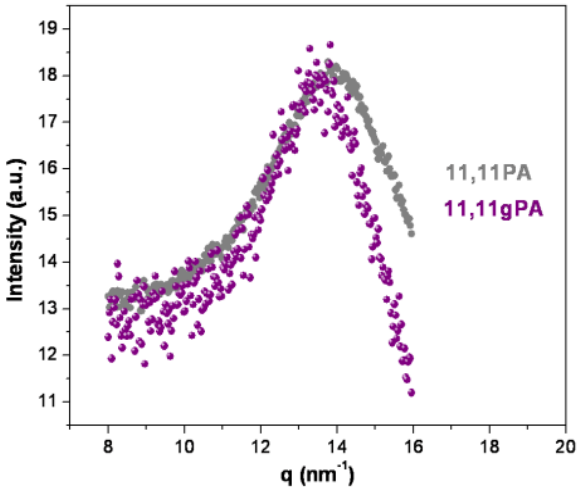

Figure 3.7 Room temperature X-ray scattering of 11,11PA and 11,11gPA, which are small molecules with mono- and geminal-substitution of PA pendant groups, respectively. The amorphous halo for 11,11PA is comparable to that of the mono-substituted precise copolymers (p15PA and p21PA, see Figure 3.6), while the amorphous halo for 11,11gPA exhibits one correlation length in distinct contrast to the behavior of geminal-substituted precise copolymers (p15gPA and p21gPA, see Figure 3.6)

3.3.3 Precise and Pseudo-Random Configurations: Finally, we compare interaggregate scattering from precise and pseudo random linear copolymers (Figure 3.1d-f). The behavior of the aggregate peaks in precise and pseudo-random mono-substituted AA copolymers has been examined in previous studies, where it has been shown that r21AA does not exhibit a correlation peak in X-ray scattering.[15] For PA and ImBr materials, X-ray scattering at elevated temperature are shown for r21PA, r21gPA and r21ImBr along with the corresponding precise copolymers, Figure 3.8. For r21PA there are losses in intensity and sharpness compared to p21PA arising from a wider

distribution of interaggregate spacings within morphologies with liquid-like order. This behavior is expected due to the wide distribution in PE segments separating the PA pendants. The peak maximum also shifts to slightly higher *q* indicating that, on average, the aggregates are closer to each other, perhaps because the minimum separation between pendant groups is smaller in r21PA than p21PA. In the geminal PA materials, the most striking effect due to pseudo-random functional group distribution is the loss of the FCC periodicity found in p21gPA. The aggregate peak in r21gPA indicates liquid-like packing, highlighting the importance of precise distribution of the associating groups along the polymer chain in producing long-range order. It is also worth noticing that at wide angles, r21gPA exhibits two overlapping characteristic length scales in the amorphous halo comparable to that of p21gPA. For r21ImBr, the aggregate peak also becomes broader (although not less intense) compared to p21ImBr, which is consistent with changes in r21PA and p21PA. However, unlike the acid copolymers, the peak maximum shifts to lower *q* indicating a longer average *d*-spacing between aggregates and might indicate a change in the shape of the aggregates.

Recent simulations of various acid- and ion-containing copolymers have found evidence of microphase separated aggregates of various shapes including nominally spherical aggregates and stringy aggregates.[20, 21, 23, 24] Specifically, a coarse-grained MD simulations study of sodium-neutralized ionomers found that precise functionalization results in spherical aggregates with liquid-like packing, while pseudo-random functionalization produces string-like aggregates.[21] A change in aggregate shape from spherical to string-like will produce larger aggregates with more polar groups per

aggregate, which in turns requires the aggregates to be further apart and corresponding shift of the low-angle scattering peak to lower *q*. As stated at the onset of this chapter, X-ray scattering data alone is insufficient to identify the shape and size of the ionic aggregates, so additional characterization tools are required to further explore how the carbon spacer length between pendant groups, the size and volume fraction of the pendant species, functional group configuration (single or geminal substitution), and functional group sequencing impact the shape of the aggregates. The X-ray scattering results presented here have laid a foundation for continued studies of these fascinating model copolymers.

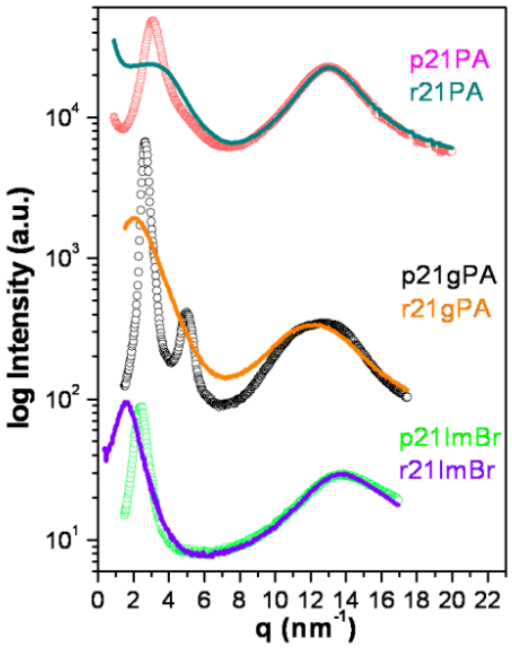

Figure 3.8 Intensity vs. X-ray scattering vector for precise vs. pseudo-random PA and ImBr copolymers. Data on the PA copolymers were collected at 150 °C, and for the ImBr materials at 120 °C.

3.4 Conclusions

The morphologies of twelve PE-based acid- and ion-containing precise copolymers and three pseudo-random copolymers were studied at elevated temperature via X-ray scattering. Eleven of the precise copolymers exhibit liquid-like order of the ionic aggregates, while p21gPA presents a cubic morphology. While the aggregate sizes and shapes were not ascertained, the average interaggregate distances (d^*) between aggregates with liquid-like order follow a number of trends, Figure 3.2b. For materials copolymerized with the same polar comonomer (AA, PA or ImBr), d^* increases as the separation of the pendants increases precisely from every 9th to every 21st carbon atom. For copolymers with the same spacer length, d^* increases as the size of the pendant increases from carboxylic acid to PA to ImBr. Also at a fixed spacer length, adding a second pendant group to change the architecture for mono to geminal substitution also increases d^*. These findings are consistent with the interaggregate spacing including both the nominal length of the PE segment and the aggregate size, Thus, d^* increases with overall volume fraction of pendant, which is controlled by the PE spacer length, the pendent volume and the chain architecture (mono- or geminal- substitution). The distinction between precise and pseudo-random placement is demonstrated in three copolymers, wherein the morphologies for precise copolymers (p21PA, p21gPA, p21ImBr) are much better defined in X-ray scattering.

In the geminal PA copolymers, two characteristic length-scales are observed in the scattering profiles corresponding to the amorphous PE matrices. This unusual feature

was not found in small molecular analogs and might be associated with defective packing of the PE chains near the acid aggregates and most likely arises from steric hindrances of the bulky PA groups; further study is necessary.

The synthesis of precise copolymers has been a great achievement in fundamental polymer synthesis and has produced morphologies with unprecedented uniformity. Moreover, these precise copolymers facilitate opportunities for direct comparison to simulations. Simulations along with characterization tools beyond X-ray scattering are expected to elucidate the remaining questions, such as the various sizes and shapes of the acid-rich and ionic aggregates. In Chapter 4, the room temperature morphologies of these copolymers are reported to include liquid-like and cubic morphologies similar to those described here at high temperatures, as well as layered aggregate morphologies that form at the onset of PE crystallinity and become anisotropic upon stretching.[25]

3.5 References

1. Baughman, T. W.; Wagener, K. B., Recent advances in ADMET polymerization. In *Metathesis Polymerization*, 2005; Vol. 176, pp 1-42.

2. Alamo, R. G.; Jeon, K.; Smith, R. L.; Boz, E.; Wagener, K. B.; Bockstaller, M. R. *Macromolecules* **2008,** 41, (19), 7141-7151.

3. Boz, E.; Wagener, K. B.; Ghosal, A.; Fu, R. Q.; Alamo, R. G. *Macromolecules* **2006,** 39, (13), 4437-4447.

4. Qiu, W. L.; Sworen, J.; Pyda, M.; Nowak-Pyda, E.; Habenschuss, A.; Wagener, K. B.; Wunderlich, B. *Macromolecules* **2006,** 39, (1), 204-217.

5. Eisenberg, A.; Kim, J.-S., *Introduction to Ionomers*. 1st ed. ed.; Wiley: New York, 1998.

6. Wakabayashi, K.; Register, R. A. *Polymer* **2005,** 46, (20), 8838-8845.

7. Wakabayashi, K.; Register, R. A. *Macromolecules* **2006,** 39, (3), 1079-1086.

8. Scogna, R. C.; Register, R. A. *Polymer* **2008,** 49, (4), 992-998.

9. Scogna, R. C.; Register, R. A. *Polymer* **2009,** 50, (2), 585-590.

10. Wu, Q.; Weiss, R. A. *Polymer* **2007,** 48, (26), 7558-7566.

11. Gao, Y.; Choudhury, N. R.; Dutta, N.; Shanks, R.; Weiss, R. *J. Therm. Anal. Calorim.* **2003,** 73, (1), 361-380.

12. Phillips, P. J.; Emerson, F. A.; MacKnight, W. J. *Macromolecules* **1970,** 3, (6), 767-771.

13. Grady, B. P. *Polym. Eng. Sci.* **2008,** 48, (6), 1029-1051.

14. Baughman, T. W.; Chan, C. D.; Winey, K. I.; Wagener, K. B. *Macromolecules* **2007,** 40, (18), 6564-6571.

15. Seitz, M. E.; Chan, C. D.; Opper, K. L.; Baughman, T. W.; Wagener, K. B.; Winey, K. I. *J. Am. Chem. Soc.* **2010,** 132, (23), 8165-8174.

16. Opper, K. L.; Markova, D.; Klapper, M.; Mullen, K.; Wagener, K. B. *Macromolecules* **2010,** 43, (8), 3690-3698.

17. Aitken, B. S.; Buitrago, C. F.; Heffley, J. D.; Lee, M.; Gibson, H. W.; Winey, K. I.; Wagener, K. B. *Macromolecules* **2012,** 45, 681-687.

18. Steininger, H.; Schuster, M.; Kreuer, K. D.; Kaltbeitzel, A.; Bingol, B.; Meyer, W. H.; Schauff, S.; Brunklaus, G.; Maier, J.; Spiess, H. W. *Phys. Chem. Chem. Phys.* **2007,** 9, (15), 1764-1773.

19. Elaiwi, A.; Hitchcock, P. B.; Seddon, K. R.; Srinivasan, N.; Tan, Y. M.; Welton, T.; Zora, J. A. *J. Chem. Soc.-Dalton Trans.* **1995**, (21), 3467-3472.

20. Hall, L. M.; Stevens, M. J.; Frischknecht, A. L. *Phys. Rev. Lett.* **2011,** 106, (12).

21. Hall, L. M.; Seitz, M. E.; Winey, K. I.; Opper, K. L.; Wagener, K. B.; Stevens, M. J.; Frischknecht, A. L. *J. Am. Chem. Soc.* **2012,** 134, (1), 574-587.

22. Lin, K. J.; Maranas, J. K. *Macromolecules* **2012,** 45, (15), 6230 - 6540.

23. Bolintineanu, D. S.; Stevens, M. J.; Frischknecht, A. L. *ACS Macro Lett.* **2013,** 2, (3), 206-210.

24. Bolintineanu, D. S.; Stevens, M. J.; Frischknecht, A. L. *Macromolecules* **2013**, DOI: 10.1021/ma400848m.

25. Buitrago, C. F.; Jenkins, J. E.; Opper, K. L.; Aitken, B. S.; Wagener, K. B.; Alam, T. M.; Winey, K. I. *Macromolecules*, Submitted.

26. Brandrup, J.; Immergut, E. H., *Polymer Handbook*. John Wiley & Sons: New York, 1989.

27. Roy, S.; Ataol, T. M.; Muller-Plathe, F. *J. Phys. Chem. B* **2008,** 112, (25), 7403-7409.

28. Kim, K. S.; Shin, B. K.; Lee, H. *Korean J. Chem. Eng.* **2004,** 21, (5), 1010-1014.

29. Heiney, P. A. *Comission on Powder Diffraction Newsletter* **2005,** 32, 9-11.

30. Jenkins, J. E.; Seitz, M. E.; Buitrago, C. F.; Winey, K. I.; Opper, K. L.; Baughman, T. W.; Wagener, K. B.; Alam, T. M. *Polymer* **2012,** 53, 3917-3927.

31. Alam, T. M.; Jenkins, J. E.; Bolintineanu, D. S.; Stevens, M. J.; Frischknecht, A. L.; Buitrago, C. F.; Winey, K. I.; Opper, K. L.; Wagener, K. B. *Materials* **2012,** 5, 1508-1527.

32. Phillips, P. J.; Emerson, F. A.; MacKnight, W. J. *Macromolecules* **1970,** 3, (6), 771 - 777.

33. Buitrago, C. F.; Opper, K. L.; Wagener, K. B.; Winey, K. I. *ACS Macro Lett.* **2012,** 1, (1), 71-74.

Chapter 4

Room Temperature Morphologies of Precise Acid- and Ion-Containing Polymers

4.1 Introduction

The current interest in acid- and ion-containing polymers is largely driven by their potential as ion conductors for energy storage or conversion, membranes for water purification or desalination, electroactive materials for actuators or sensors, and shape memory materials. New polymers are being synthesized and evaluated for these potential applications, but the guiding principles for designing and improving these materials remain elusive. In the past, robust correlations and even predictive models that relate chemical microstructure to nanoscale morphology and to macroscopic properties have been built upon studies that combine model polymers and careful study. Insights that have come from employing model polymers abound in polymer physics. The study of polymer dynamics advanced significantly thanks to polymers made by anionic polymerization with precise molecular weight control. The understanding of polymer crystallization has progressed in part by the ability to dictate the number and length of branching.

To advance the understanding of acid- and ion-containing polymers, we employ precise copolymers and, to date, our focus has been on their morphology. Acyclic diene metathesis polymerization (ADMET) produces linear, high molecular weight polyethylenes (PE) precisely copolymerized with acrylic acid (AA),[1] phosphonic acid

$(PA)^2$ and 1-methylimidazolium bromide (ImBr),[3] Figure 4.1. The polar pendants are substituted on every 9^{th}, 15^{th} or 21^{st} carbons in mono or geminal architecture. In a recent study, we probed the morphologies of twelve precise copolymers at elevated temperatures ($T > T_m$ or T_g), as well as three pseudo-random copolymers for comparison.[4] Eleven of the twelve precise copolymers exhibit liquid-like morphologies, wherein the PE matrix is amorphous and the acid or ion pendants form aggregates that arrange with liquid-like order. In contrast, one of the copolymers with two PA pendants on every 21^{st} carbon yielded a cubic morphology at high temperature, similar to the cubic structure it presents at room temperature.[5]

In this study, we focus on the room temperature morphologies of these twelve precise copolymers (Table 4.1) using a combination of solid-state ^{13}C NMR, DSC, and X-ray scattering. In addition to the geminal PA copolymer mentioned above,[5] the room temperature morphologies of three of these copolymers have been previously reported, specifically the mono-substituted AA copolymers.[1,6] From the earlier studies, three morphology types have been defined based on the nature of the acid or ionic aggregates resulting from microphase separation of the acid or ionic pendant groups and the PE matrix. When the PE segments are short, the aggregates pack with liquid-like order.[1,6] This chapter reports three more copolymers with this morphology and compares the interaggregate space as a function of spacer length and pendant type. When the PE segment is longer than 14 carbon atoms, the AA copolymer is semi-crystalline at room temperature and the pendants assemble into layers.[1,6] Upon drawing, this copolymer becomes anisotropic such that the PE chains and the acid layers orient, respectively,

parallel and perpendicular to the stretch direction. Here we report four more copolymers with a layered morphology, including two copolymers with ImBr pendants that display a different orientation when stretched. The third morphology type has cubic symmetry. The first report of cubic symmetry in a precise copolymer was in the AA copolymer functionalized on every 9th carbon and neutralized with 66 mol% Zn at high temperature (120 °C).[6] The lattice was determined to be body centered cubic (BCC) and the long-range order was lost upon cooling to room temperature. The second report of a cubic morphology was the face-centered cubic (FCC) symmetry found in the copolymer with two PA pendants on every 21st carbon. This FCC symmetry was observed both, at room and elevated temperatures.[5] In this chapter we report another example of a cubic morphology, again in a copolymer with geminal substitution of PA, although the long-range order is lost upon heating. Illustrative representations of the liquid-like, layered and cubic morphology types are presented in Figure 4.2.

Our intention is to build on the fundamental understanding of acid- and ion-containing polymers to facilitate the design of new chemical structures for targeted transport and mechanical properties. This extensive morphology study of precise AA, PA and ImBr copolymers is one piece of that much larger puzzle. *In situ* mechanical testing and X-ray scattering of some of these materials is already underway, and those studies will further elucidate the fundamental structure-property relationships in these model materials.

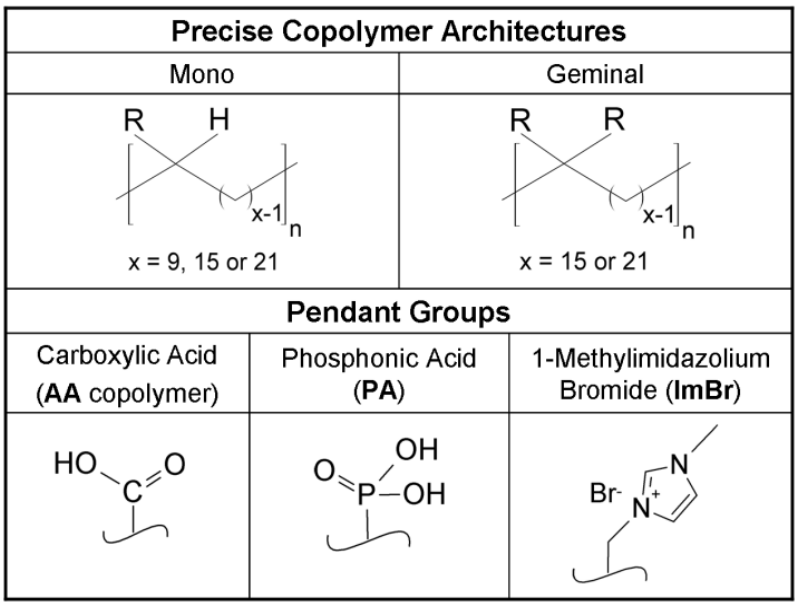

Figure 4.1 Precise polymer architecture and pendant groups in polyethylene-based copolymers.

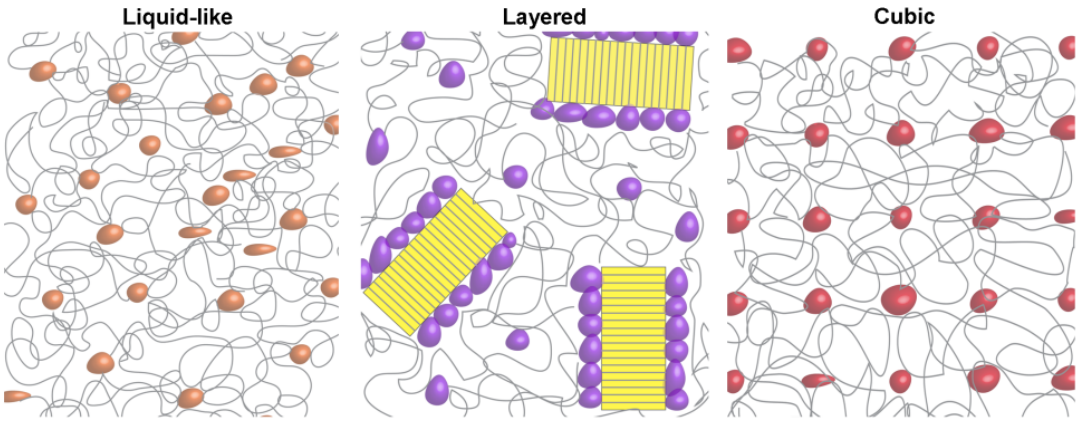

Figure 4.2 Morphology types of precise acid copolymers and ionomers at room temperature. The morphologies are characterized by the order of the aggregates (colored globules) in the PE matrix. PE crystals are represented in yellow, and the grey lines represent PE.

4.2 Experimental Section

4.2.1 Materials: The materials studied here are listed in Table 4.1 and have been the subject of a recent report describing their morphologies at elevated temperatures.[4] The nomenclature scheme is as follows: the letter *p* indicates the precise placement of pendant groups along the polymer chain. This is followed by a number (x = 9, 15 or 21) specifying the frequency of pendant substitution (every 9^{th}, 15^{th}, or 21^{st} carbon), Figure 4.1. For materials with two pendant groups on each functionalized carbon, the letter *g* stands for geminal substitution. Finally, the copolymerized species is denoted as AA (acrylic acid), PA (phosphonic acid) or ImBr (1-methylimidazolium bromide), Figure 4.1.

Table 4.1 Morphology Types and Morphological Parameters for Various Precise Copolymers at Room Temperature (20 °C)

Morphology Type	Precise Copolymer	Pendant Vol. Fraction ($\phi_{pendant}$)	Morphological Parameter (nm)
Liquid-like[a]	p9AA	0.20	1.01
	p15AA	0.13	1.43
	p9PA	0.31	1.38
	p15PA	0.21	1.77
	p9ImBr	0.48	1.85
Layered[b]	p21AA	0.10	2.54
	p21gAA	0.18	2.48
	p21PA	0.16	2.65
	p15ImBr	0.36	2.72
	p21ImBr	0.29	3.33
Cubic[c]	p15gPA	0.35	2.90 (BCC) or 2.06 (SC)
	p21gPA	0.25	4.10 (FCC)

Morphological parameters:

[a] $d^* = \frac{2\pi}{q^*}$ [b] $a_{layer} = d_h h$ [c] $a_{cub} = d_{hkl}(h^2 + k^2 + l^2)^{1/2}$

4.2.2 Sample Preparation: For this study, the precise copolymer samples were prepared for instrumental analysis in the following manner. Films for solid-state ^{13}C NMR and room temperature X-ray scattering were melt-pressed at 150 °C for 20 minutes in a Carver 4122 hot press. Note that the thermal transitions (T_g, T_m) of all the copolymers are below 150 °C (Table 4.2). The films were then subjected to rapid cooling via a heat exchanger using tap water. Stretched samples were produced by drawing a pressed film in hot air and then cooling at ambient temperature under tension. Both as-pressed and drawn films were aged at room temperature for at least 3 days before NMR

and X-ray scattering data collection. Because this sample preparation method varies from earlier methods, there may be discrepancies with earlier reports, particularly with respect to percent crystallinity.

4.2.3 Differential Scanning Calorimetry: Differential scanning calorimetry (DSC) data were obtained on a TA instruments Q2000 calibrated for temperature transitions and enthalpy changes using an indium standard. The samples weighed approximately 5 – 10 mg and were cut from the X-ray scattering samples aged at room temperature for 3 days. The heating thermographs on those samples were measured at a heating rate of 10 °C/min under a helium purge.

4.2.4 Solid-State ^{13}C MAS NMR Spectroscopy: All solid-state ^{13}C MAS NMR data were collected on a Bruker Avance 400 MHz wide bore spectrometer equipped with a 4mm double resonance MAS probe operating in $^{13}C/^{1}H$ mode. The samples were packed in a 4 mm zirconia rotor with Kel-F® cap. All experiments were performed with a 10 kHz spinning speed at 294 K. Chemical shifts were set to the downfield peak of the external secondary reference adamante (δ = +38.56 ppm). A 1 ms contact time was utilized during $^{1}H \rightarrow ^{13}C$ cross-polarization (CP) data collection, with a 5 s recycle delay and the CP conditions matched to the -1 spinning side band (ssb) of the Hartmann-Hahn profile. Directly detected ^{13}C quantitative data was collected utilizing 600 s recycle delay to allow for complete equilibration. Two-pulse phase-modulated (TPPM) ^{1}H decoupling was employed in all ^{13}C MAS experiments. The DMFIT software package was used to deconvolve the quantitative data.[7] Constraints for the spectral fits, such as chemical shift and line width, were extracted from ^{13}C CP data with either a ^{1}H spin-lock pulse prior to

cross-polarization or a ^{1}H dipolar filter (see Appendix C) to improve robustness of spectral simulations.

4.2.5 X-ray Scattering: X-ray scattering for the AA and ImBr copolymers was performed at the Multi-angle X-ray Scattering (MAXS) Facility at the University of Pennsylvania. For the PA copolymers, synchrotron X-ray scattering was conducted at beamline 5ID-D (DND-CAT) of the Advanced Photon Source (APS) at Argonne National Laboratory. Details on both experimental set-ups can be found in Buitrago *et al.*[4] Two-dimensional data reduction and analysis from data collected at the MAXS facility and APS were performed using the Datasqueeze software.[8]

4.3 Results and Discussion

As summarized in Table 4.1, the precise copolymers are readily divided into three morphology types, each of which will be presented separately using NMR, DSC and X-ray scattering to construct a unified description of their room temperature morphologies.

4.3.1 Liquid-Like Morphologies: The liquid-like morphologies in precise copolymers contain acid or ionic aggregates within amorphous PE such that the aggregates adopt a nominally liquid-like arrangement. At elevated temperatures ($T > T_m$) this morphology type dominates, being observed in eleven of the twelve precise acid- and ion-containing copolymers available.[4] At room temperature the liquid-like morphology type is prevalent when the monomeric unit in the precise copolymers contains just 9 or 15 carbons. Moreover, none of the precise copolymers substituted on every 21st carbon, nor the geminal substituted materials, fall into this morphology category. In copolymers with

pendant groups on every 9th or 15th carbon, the PE matrix is amorphous as the result of pendants disrupting PE crystallization, because pendants cannot be readily accommodated into crystalline PE and hydrogen bonding between the pendants decreases the diffusional motion necessary to crystallize.[1-3] Amorphous PE is required for the acid and ionic aggregates to assume liquid-like packing.

The five precise copolymers designated as having liquid-like morphologies at room temperature exhibit an amorphous PE matrix as strongly evidenced by ^{13}C CP MAS NMR, Figure 4.3a. As previously reported and shown here for completeness, the copolymers p9AA and p15AA exhibit a broad resonance centered at +30.5 ppm for the CH_2 carbons, indicating a non-crystalline, amorphous polymer backbone.[9] Their weaker resonance for CH carbons are seen at ~ +46.5 ppm. Similarly, p9PA and p15PA exhibit a large peak at ~ +30 ppm consistent with the CH_2 resonance of amorphous PE and a high ppm shoulder at ~+36 ppm that is attributed to the CH group. In p9ImBr, the large peak spanning from +25 to +35 ppm consists of overlapping resonances for the polyethylene backbone and the pendant groups. The largest portion of the resonance at +30.4 ppm is consistent with CH_2 in an amorphous phase. The ^{13}C CP MAS NMR data show that the PE matrices in all five liquid-like materials are consistent with PE in an amorphous phase, as summarized in Table 4.2.

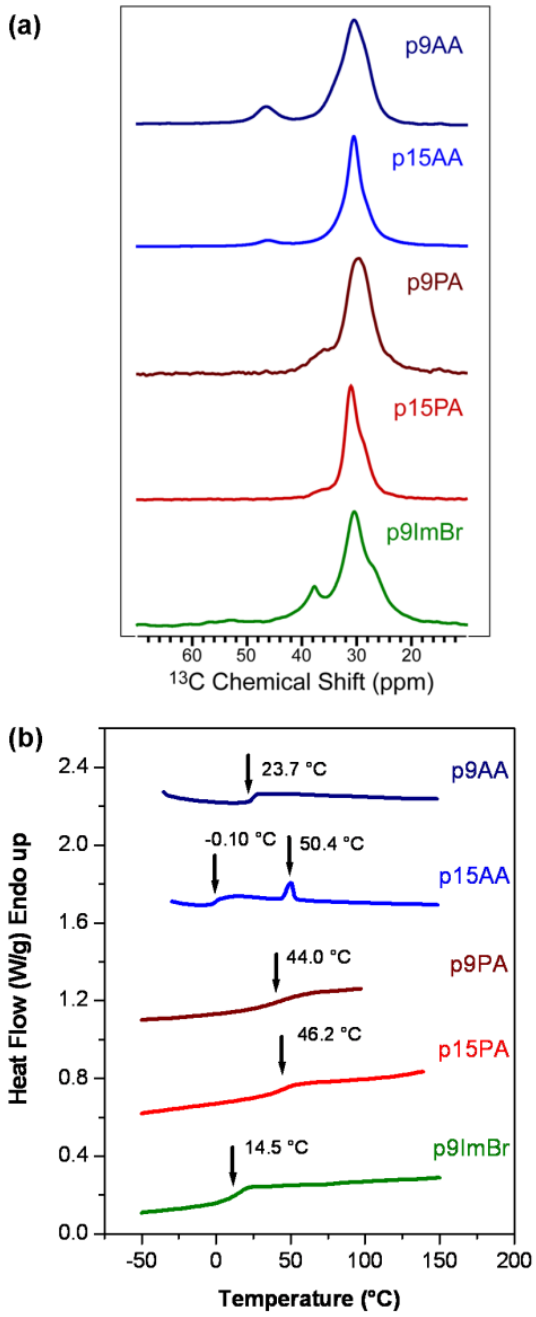

Figure 4.3 (a) ^{13}C CP MAS NMR spectra of five precise copolymers exhibiting liquid-like morphologies. (b) DSC thermographs of precise AA, PA and ImBr copolymers exhibiting liquid-like morphologies, where the black arrows denote the T_gs. The copolymer p15AA exhibits a small endotherm.

Table 4.2 Thermal Transitions (DSC) and Polyethylene Chain Structure (NMR) for Precise Acid Copolymers and Ionomers

		DSC Data (°C)		^{13}C NMR CH_2 δ (ppm)[a]		
		T_g	T_m	Orthorhombic Crystalline Trans	Amorphous Trans/Gauche	Gauche Defect
Liquid	p9AA	23.7			30.5	
	p15AA	-0.10	50.4		30.5	
	p9PA	44.0			29.6	
	p15PA	46.2			31.0	
	p9ImBr	14.5			30.4	
Layered	p21AA[b]		47.7	33.2 (35%)	30.8 (65%)	
	p21gAA[b]		46.1	33.2 (34%)	30.8 (60%)	27.3 (6%)
	p21PA[b]		47.4, 63.0	33.0 (23%)	31.2 (70%)	28.0 (7%)
	p15ImBr[c]		49.3, 70.1	32.6	30.9	
	p21ImBr[c]		88.7, 113.5	33.3	31.0	
Cubic	p15gPA	53.4			31.5	
	p21gPA	66.4			31.5	

[a] δ = chemical shift (error estimated ± 0.1 ppm)
[b] Component percentage in parenthesis
[c] Chemical Shift assignment not confirmed

The lack of PE crystallinity in those copolymers is confirmed by the DSC thermographs exhibiting glass transition temperatures (T_g) typical of amorphous PE, Figure 4.3b. While the DSC trace of p15AA has a weak endotherm at 50 °C suggesting ~ 1 wt% crystallinity; the heat of melting for this peak is very small (ΔH_m = 2.9 J/g) compared to the enthalpy of melting for crystalline PE (ΔH_m ~ 277.1 J/g).[10] Given the absence of crystallinity detected in p15AA by ^{13}C CP MAS NMR, we interpret the small endotherm as indicating an amorphous PE matrix that incorporates slight ordering in the

polymer chains. A similar trend has been observed in aged p15AA neutralized with Na and Cs, where X-ray scattering exhibits only amorphous halos but DSC shows both a T_g and a weak T_m endotherm; see Appendix C.

One-dimensional X-ray scattering profiles of the materials that exhibit liquid-like morphology at room temperature are shown in Figure 4.4. The typical scattering profiles for the liquid-like morphology exhibit only two broad peaks: the amorphous halo at scattering vector (q) ≈ 14 nm^{-1}, and a low-angle peak at q ≈ 2-8 nm^{-1} associated with interaggregate scattering from microphase separated associating groups.[11] Linear polyethylene synthesized by ADMET has been found to form orthorhombic crystals resulting in X-ray scattering reflections at q = 15.3 and 17.0 nm^{-1}.[12] The absence of those peaks in the copolymers in Figure 4.4 confirms that their PE segments are amorphous, in agreement with ^{13}C NMR, DSC and with previous observations in precise copolymers showing that the PE segments must be longer than 14 carbons to crystallize.[6]

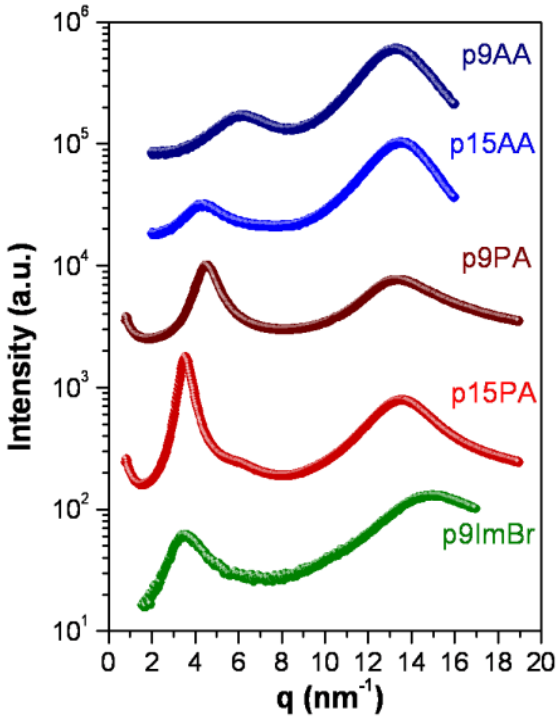

Figure 4.4 Room temperature X-ray scattering of precise AA, PA and ImBr copolymers featuring liquid-like packing of aggregates of the associating groups, as evidenced by the broad peaks at q between 2 and 8 nm^{-1}. Data is shifted vertically for clarity in this and subsequent figures.

The single scattering peak at low angles reflects a lack of long-range order of the aggregates. It has been demonstrated for acid- and ion-containing polymers[6, 13, 14] that this low-angle peak arises from the short-range order of domains with liquid-like packing, whose average separation, or d-spacing (d^*), can be obtained from the peak maximum (q^*) using the equation $d^* = 2\pi/q^*$. For copolymers with carboxylic acid and PA pendants, the low-angle peaks shift to lower q (higher d^*, Table 4.1) as their precise

separation increases from 9 to 15 carbons. This increase in the average separation of the aggregates is expected as the bridging segments between the pendants increases. This is also consistent with the composition of the pendant groups: as the level of functionalization decreases from every 9th carbon (22.2 mol% of the pendant species) to every 15th carbon (13.3 mol%), a smaller number of pendants per carbon produces fewer aggregates with longer distance between them.

For the precise copolymers substituted on every 9th carbon, *d** increases from 1.01 to 1.38 to 1.85 nm as the volume fraction of the pendant groups increases by changing the substituent from AA, PA to ImBr, respectively. The same trend is apparent for p15AA and p15PA, Table 4.1. For comparison, the length of 9 carbon-carbon bonds in the all-*trans* conformation is 1.15 nm. As described at length elsewhere for the liquid-like morphology of precise copolymers at elevated temperatures,[4] larger acid or ionic pendant groups apparently produce larger aggregates, so that the center-to-center distance between aggregates can readily exceed the all-*trans* length of the spacer. Upon heating from room temperature to 120 °C, *d** expands ~ 4% and ~ 5% for p9AA and p15AA, respectively, while the *d** values change ~ +/- 1% between room temperature and 150°C in p9PA and p15PA. These small changes in *d** suggest a modest change in the liquid-like morphology upon heating these AA and PA copolymers. In contrast, *d** contracts by ~ 11% when p9ImBr is heated from room temperature to 120°C, indicating a substantive change in the liquid-like morphology including a possible change the percentage of pendants in aggregates or in aggregate shape.

4.3.2 Layered Morphologies: The layered morphologies in precise copolymers contain acid or ionic pendants arranged in layers and accompanied by semi-crystalline PE. This morphology group includes all the copolymers with single pendants on every 21st carbon (p21AA, p21PA and p21ImBr), the geminal AA copolymer (p21gAA) and the precise ImBr copolymer substituted on every 15th carbon (p15ImBr). The semi-crystallinity of these five copolymers with layered morphologies is evidenced by both ^{13}C NMR and DSC; note that thermal history was rigorously controlled throughout the experiments, as detailed in the experimental description. Figure 4.5 shows both the ^{13}C CP MAS NMR spectra (left) and deconvolved quantitative direct ^{13}C MAS NMR data (right). Table 4.2 reports the chemical shifts and the relative amounts of CH_2 groups in orthorhombic crystalline, amorphous and gauche defect conformations. Note that the crystalline and amorphous phases could only be quantified for three of the layered morphologies. The copolymers p21AA, p21gAA and p21PA exhibit large CH_2 resonances spanning ~ +25 to +35 ppm, consisting of two or three distinct overlapping signals deconvolved into three peaks: amorphous, crystalline, and gauche defect. Both p21AA and p21gAA have ~ 35% crystallinity, while p21PA has 23%. As described above, the ImBr pendant group contains multiple overlapping resonances in the +25 to +40 ppm range. For both p15ImBr and p21ImBr, this region is deconvolved into four resonances, although their assignments are only speculation at this time. The resonances observed at ~ +31 most likely indicate an amorphous polyethylene backbone component, while the resonance at ~ +33 is consistent with a crystalline backbone. However, due to

the lack of constraints and chemical shift spectral assignment, the percent crystallinity in these two precise copolymers is not reported.

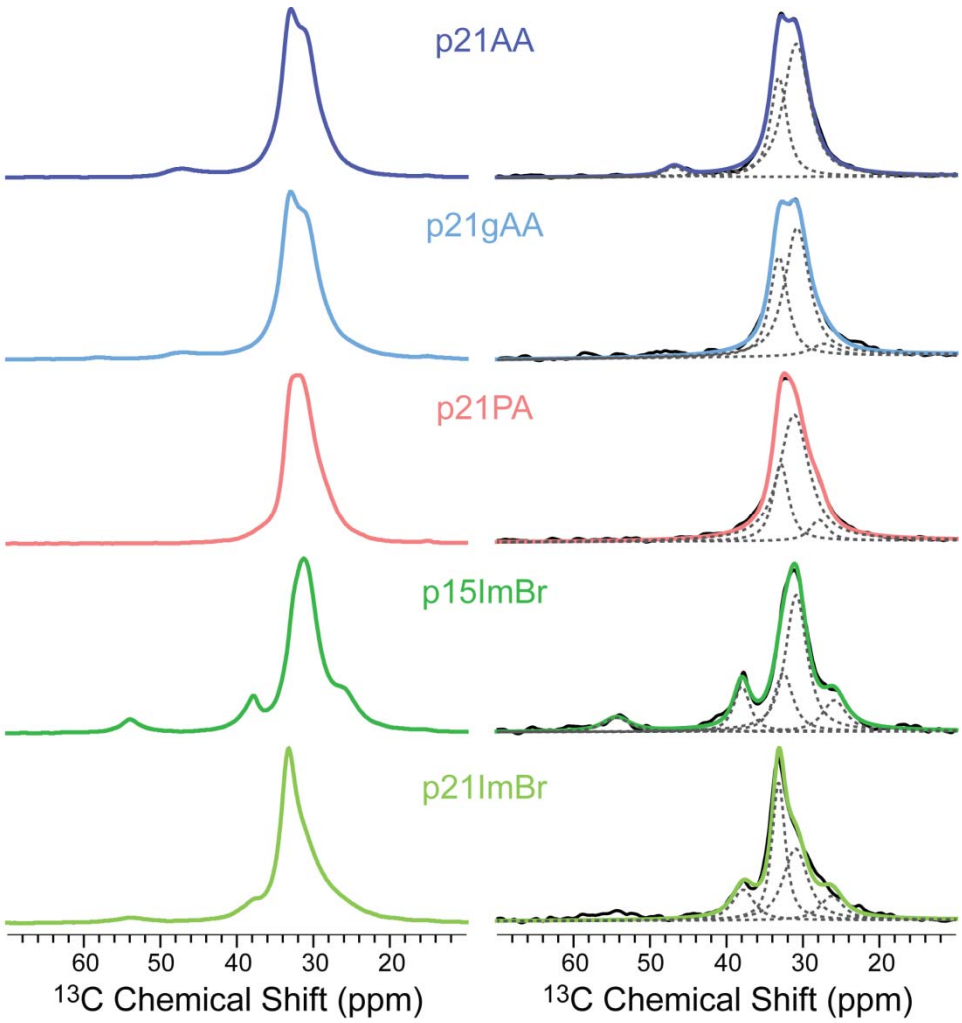

Figure 4.5 ^{13}C CP MAS NMR spectra (left) and deconvolved quantitative ^{13}C MAS NMR data (right) for five precise copolymers exhibiting layered morphologies.

DSC results for the five precise copolymers that exhibit layered morphologies display melting transitions for the PE crystallites over wide temperature ranges and often

with bimodal endotherms, Figure 4.6. The melting temperatures (see Table 4.2) for the copolymers are well below the reported T_m for linear PE synthesized by ADMET polymerization (130 °C).[12] The mono-substituted AA copolymer (p21AA) exhibits an endotherm with ΔH_m = 65.4 J/g, while the geminal AA copolymer (p21gAA) has weaker heat of melting (ΔH_m = 38.8 J/g). This difference is attributed to p21gAA having twice the number of pendants compared to p21AA, which limits the diffusional motion of the polymer chains and impedes crystallization. Interestingly, the ^{13}C NMR data indicate that p21AA and p21gAA have comparable crystallinity (~ 35%) suggesting that the enthalpy of melting the PE crystallites might differ between the various precise copolymers depending on the ability of the acid or ionic groups to reinforce the crystals. The bimodal melting behavior in the PA and ImBr precise copolymers has previously been attributed to the formation of primary and secondary crystallites originating from the slow crystallization kinetics of these materials due to the limited mobility imposed by the pendant associating groups.[2,3]

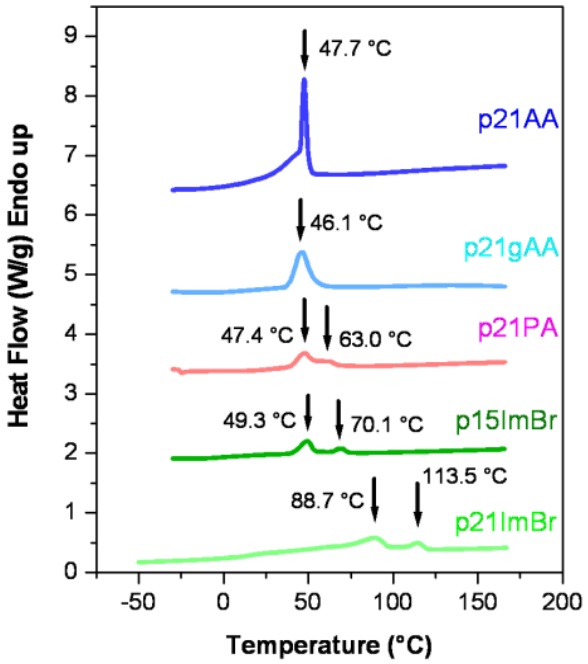

Figure 4.6 DSC thermograms of precise AA, PA and ImBr copolymers exhibiting layered morphologies. All materials have polyethylene segments long enough to form crystallites, and their T_ms are indicated by the black arrows.

Figure 4.7 shows X-ray scattering data for the five copolymers featuring layered arrangement of aggregates at room temperature. In addition to the amorphous peak, these copolymers exhibit a sharp X-ray scattering peak near 15 nm^{-1}, which is consistent with the {110} reflection for orthorhombic PE at 15.3 nm^{-1} and confirms the semicrystalline nature of the PE matrix.[12] In addition, multiple scattering peaks at low angles have positional ratios (q/q^*) of a layered morphology (1:2:3:4), indicating long-range order of the microphase separated acid- and ion-containing layered aggregates. The lattice parameter for layered morphology (a_{layer}) is calculated using $a_{layer} = d_h^* * h$, where h is the Miller index of the peak and d_h^* is its corresponding d-spacing from X-ray scattering.

Values for a_{layer} define the center-to-center distance of the layered aggregates and are given in Table 4.1.

There is only one precise copolymer with a pendant on every 15th carbon that exhibits the layered morphology, p15ImBr, which is unexpected given the previous claim that precise copolymers must have repeat units longer than 15 carbons to crystallize.[6] However, unlike the AA and PA pendants, each ImBr pendants has a CH_2 linker between the pendant and the polymer backbone (Figure 4.1) and this linker could provide extra mobility for the PE segment to crystallize. Moreover, studies of ionic liquids containing imidazolium bromide identify three H-bonding sites that assemble the ImBr groups into sheets.[15] The assembly of the ImBr pendants into sheets could also contribute to the ability of p15ImBr to form PE crystallites. For the copolymers functionalized on every 21st carbon with a single pendant, a_{layer} increases as the pendant size increases from AA (2.54 nm) to PA (2.65 nm) to ImBr (3.33 nm). Functionalization with geminal AA groups (which nearly doubles the volume fraction of acid groups and removes any tacticity on the pendants) does not have a dramatic effect on the morphology at room temperature.

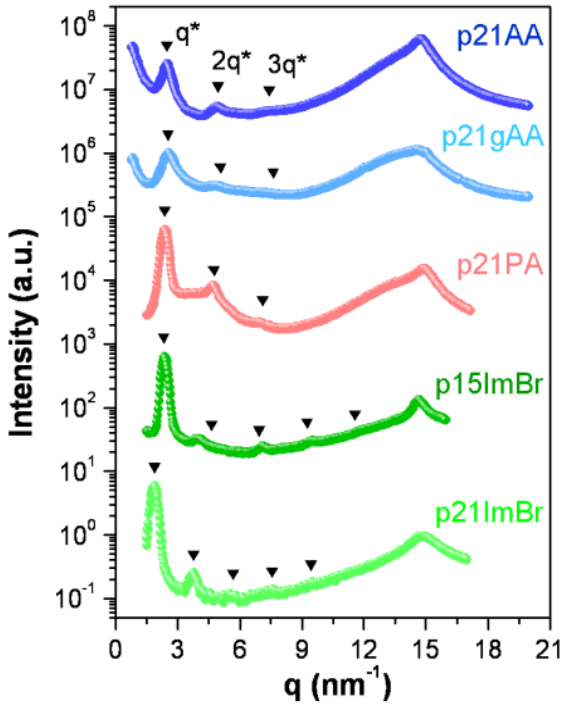

Figure 4.7 X-ray scattering of precise AA, PA and ImBr copolymers featuring layered microphase separated aggregates. Triangles indicate the expected higher order reflections (h = 1, 2, 3, 4, 5) calculated using the a_{layer} (Table 4.1). These copolymers have polyethylene segments that form crystallites, as indicated by the sharp reflections at q ~ 15 nm^{-1}.

The PE crystallites in semi-crystalline copolymers can be oriented by drawing the films. Figure 4.8 shows the two-dimensional X-ray scattering from isotropic and stretched samples of the semi-crystalline copolymers with layered morphologies and clearly demonstrates that stretching induces oriented morphologies. These images can be analyzed to give one-dimensional scattering patterns parallel and perpendicular to the draw direction, Figure 4.9. Two distinct behaviors are observed in Figures 4.8 and 4.9,

establishing a clear divergence of the two ImBr copolymers with layered morphologies from all previously observed morphologies of precise copolymers. This new layered morphology will be described following a description of the layered morphology in p21AA, p21gAA, and p21PA.

In the anisotropic patterns of the AA and PA copolymers (Figure 4.8a-c), the PE crystallinity reflection at wide angle aligns perpendicular to the drawing direction, which is expected from any of the {hk0} reflections of PE when the chain axis aligns parallel to the drawing direction.[16] This orientation of the PE crystallites relative to the stretch direction is confirmed in Figure 4.9, shown schematically in Figure 4.10a, and has been previously reported at room temperature for an acid-containing precise copolymer (p21AA) and several ion-containing precise ionomers (p21AA partially neutralized with zinc).[1,6] The multiple peaks at low angle align along the drawing direction, demonstrating that the layered acid groups are perpendicular to the polymer chains. This observation can be explained by aggregates of the associating groups decorating the crystallite surfaces and forming layers perpendicular to the drawing direction.[1] The layered morphology in Figure 4.10a is further supported by noting that the length of 21 carbon-carbon bonds in all-*trans* conformation (2.68 nm) in within 0.2 nm of a_{layer} (Table 4.1) for p21AA, p21gAA, and p21PA. It is also interesting to note that there are no discernable differences between p21AA and p21gAA (Figures 4.8a and 4.8b), suggesting that as long as the precise PE segment length remains the same, increased carboxylic acid content and loss of tacticity do not appear to have any effect on the formation of the layered morphology.

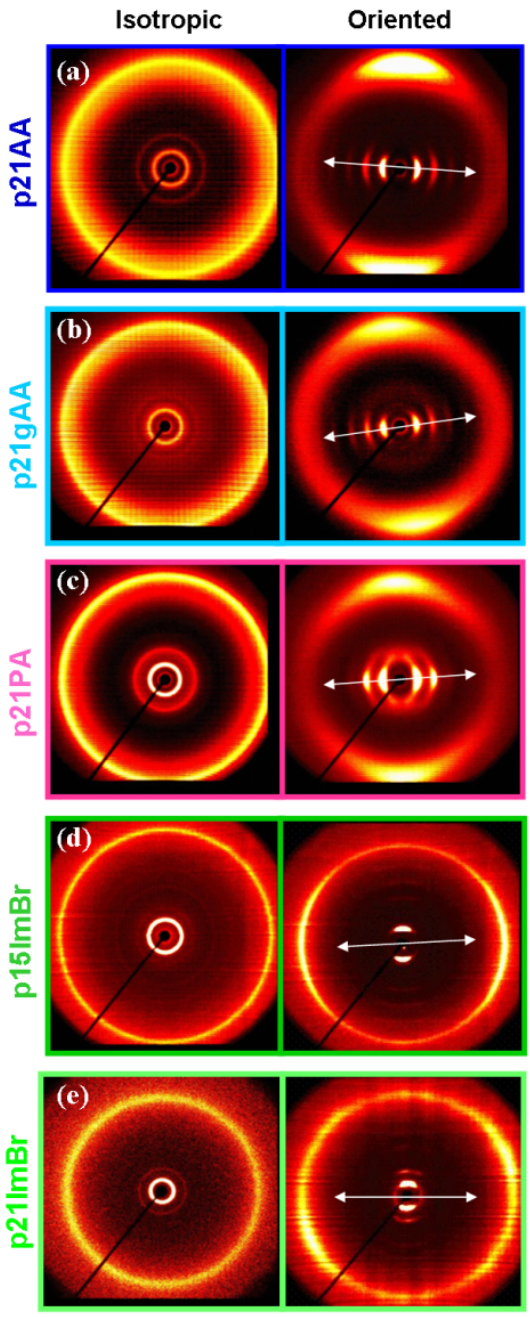

Figure 4.8 Two-dimensional X-ray scattering patterns of isotropic (left) and oriented (right) semicrystalline AA, PA and ImBr precise copolymers at room temperature: (a) p21AA, (b) p21gAA, (c) p21PA, (d) p15ImBr and (e) p21ImBr. The arrows indicate the draw direction in the oriented films.

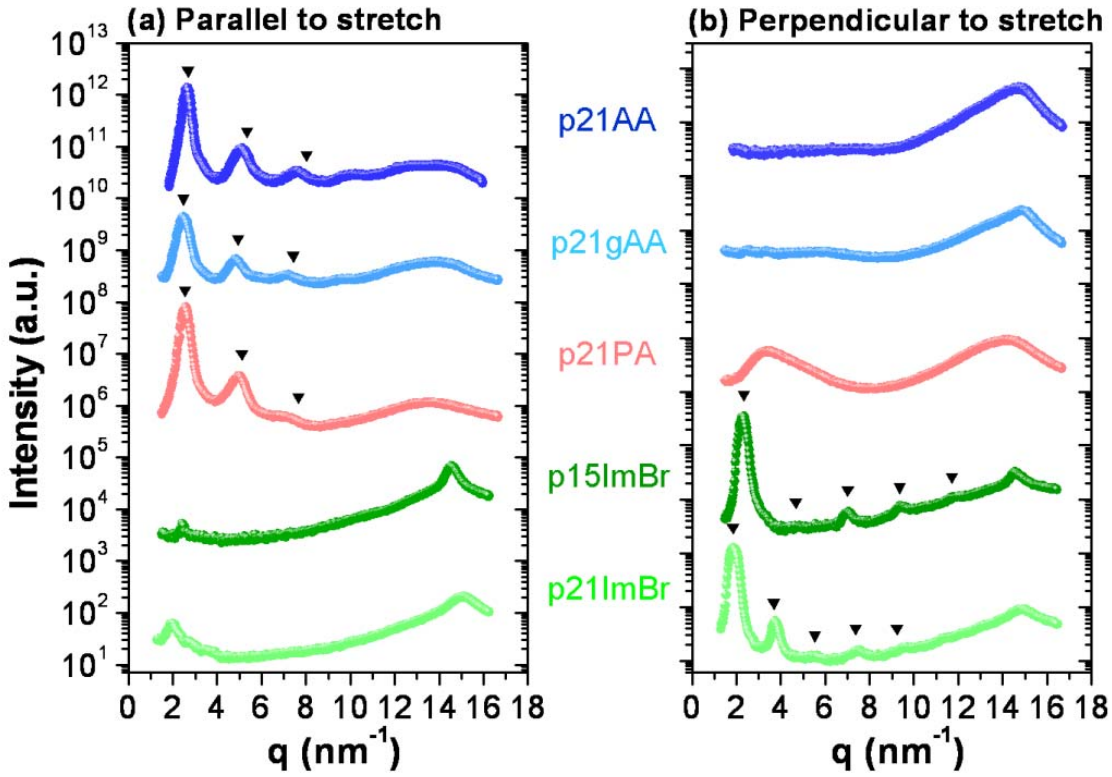

Figure 4.9 Intensity vs. scattering vector for semicrystalline AA and PA precise copolymers integrated (a) parallel and (b) perpendicular to the draw direction. Triangles indicate the expected higher order reflections (h = 1, 2, 3, 4, 5) calculated using the a_{layer} (Table 4.1).

Closer inspection of the one-dimensional patterns in Figure 4.9b for p21PA reveals an additional broad single peak with a maximum at q = 3.36 nm^{-1} perpendicular to the drawing direction. Similar peaks are not present in p21AA and p21gAA, because the scattering contrast from carboxylic acid groups is weaker. A plot of intensity vs. azimuthal angle for the drawn p21PA sample at q = 3.36 nm^{-1} (available in Appendix C)

suggests that this peak remains isotropic even though the layered morphology is anisotropic. Specifically, this correlation peak coexists with the high-ordered lamellar peaks parallel to the stretch for p21PA in Figure 4.9a, although it goes almost undetected due to its much weaker intensity. This broad isotropic scattering peak at q = 3.63 nm^{-1} (d = 1.87 nm) represents aggregates much closer to each other than the layers (a_{layer} = 2.65 nm) and corresponds to a liquid-like morphology of ionic aggregates in the amorphous domains. A similar coexistence of a layered morphology associated with the PE crystallites and a liquid-like morphology associated with the amorphous domains was previously observed in precise Zn-neutralized ionomers.[6]

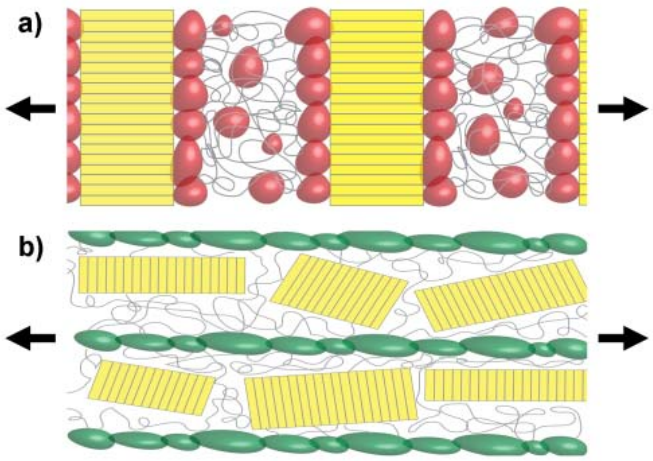

Figure 4.10 (a) Oriented p21PA showing PA aggregates (red) self-assembled into layers associated to PE crystallites (yellow) and with liquid-like order in the amorphous PE. (b) Oriented p21ImBr having aggregates of ImBr (green) in layers that form during deformation at high temperature and PE crystallites that form between the layers upon cooling. The center-to-center spacings between the PA and ImBr layers are 2.65 nm and 3.33 nm, respectively (Table 4.1). The black arrows indicate the direction of the stretch.

The layered morphologies in p15ImBr and p21ImBr are contrary to all previous observations in precise acid- and ion-containing polymers.[1,6] Stretching the copolymers functionalized with ImBr groups produces anisotropic two-dimensional scattering profiles, where the peaks corresponding to the microphase separated pendant groups align perpendicular to the stretching direction (Figure 4.8d and 4.8e). In addition, the peaks at wide angle corresponding to PE crystallinity gain intensity along the drawing direction, indicating that in this case the PE segments preferentially crystallize with the chain axis perpendicular to the stretch direction. A comparison of the 2D scattering patterns in Figure 4.8 for the ImBr-containing copolymers with the AA- and PA-containing copolymers shows less alignment of both the PE crystallites and the layers in the copolymers with ImBr pendants. The lower extent of alignment is also evident in Figure 4.8, where the PE crystalline peak (q ~ 15 nm^{-1}) is observed both parallel and perpendicular to the stretch, although it is more pronounced along the stretch direction. Also, the correlation peaks between the ImBr layers show strong and multiple higher order reflections perpendicular to the stretch direction, but one low angle peak is also evident along the stretch direction.

We propose that the distinct layered morphology in p15ImBr and p21ImBr is the consequence of strong interactions between the ImBr groups at elevated temperature and the propensity for these pendants to assemble in layers. As referenced earlier, ImBr-containing molecules have three H-bonding positions between an imidazolium ring and the small bromide anions that also contribute to forming planar assemblies.[15] *In-situ*

small angle X–ray scattering on 1-alkyl-3-methylimidazolium bromides with alkyl chains ranging from 12 to 20 carbons detected transitions from crystal to liquid crystalline phases below 100 °C.[17] In these molecules the liquid crystalline mesophases contain planar assemblies of the ImBr groups, and this self-assembled structural motif persists even when the alkyl chains have melted. In addition, DMA experiments on p9ImBr, p15ImBr and p21ImBr conducted by Aitken *et al.* suggest microphase separation of the ImBr pendant in these copolymers at elevated temperature.[3] From these findings, we conclude that the planar aggregates of ImBr groups maintain their structural integrity at elevated temperatures even when the PE segments are amorphous. These ImBr aggregates align to form layers parallel to the stretching direction in p15ImBr and p21ImBr at elevated temperatures, and upon cooling under fixed strain, the PE segments form crystals between the ImBr layers. Confined PE crystallization between the ImBr layers aligned parallel to the drawing direction produces crystallites with their chain segments preferentially aligned perpendicular to the stretch, although with only modest alignment. In contrast, the less strongly associated acid groups in the AA and PA copolymers are dissociated during deformation at high temperature, such that the PE segments take most of the mechanical load of the stretch and align parallel to the force. Unfortunately, there are insufficient quantities of the ImBr-containing copolymers for a thorough investigation of their high-temperature mechanical properties at this time.

4.3.3 Cubic Morphologies: The geminal-substituted copolymers with PA pendants (p15gPA and p21gPA) exhibit cubic order of PA aggregates at room temperature. As with the liquid-like and layered morphologies above, NMR and DSC results that

characterize the PE matrix will be presented before the X-ray scattering results. In the ^{13}C NMR data (Figure 4.11a), p15gPA and p21gPA do not exhibit any distinctly crystalline or amorphous phases (see quantitative NMR in Appendix C), indicating that these materials are in an intermediate phase on the NMR timescale. The chemical shift of the CH_2 resonances in these two materials is at a slightly higher ppm than the resonance observed in the purely amorphous materials. The DSC results shown in Figure 4.11b are similarly ambiguous (note the small scale on the *y*-axis (0 - 0.60 W/g) indicating that the transitions are weak. The thermogram for p15gPA exhibits a T_g at 53.4 °C, a broad endotherm at ~ 61.0 °C, and a smaller endotherm at 140 °C. The thermogram of p21gPA has an endotherm onset at ~ 66.4 °C and the endotherm continues to 125 °C with a maximum at 75.4 °C. The only clear information conveyed by DSC is that the PE matrices of the geminal PA copolymers undergo thermal transitions above 50 °C, but their nature is unclear. Because there is no evidence of PE crystallinity in the X-ray scattering results, the thermal transitions for the cubic morphologies are reported as glass transitions in Table 4.2.

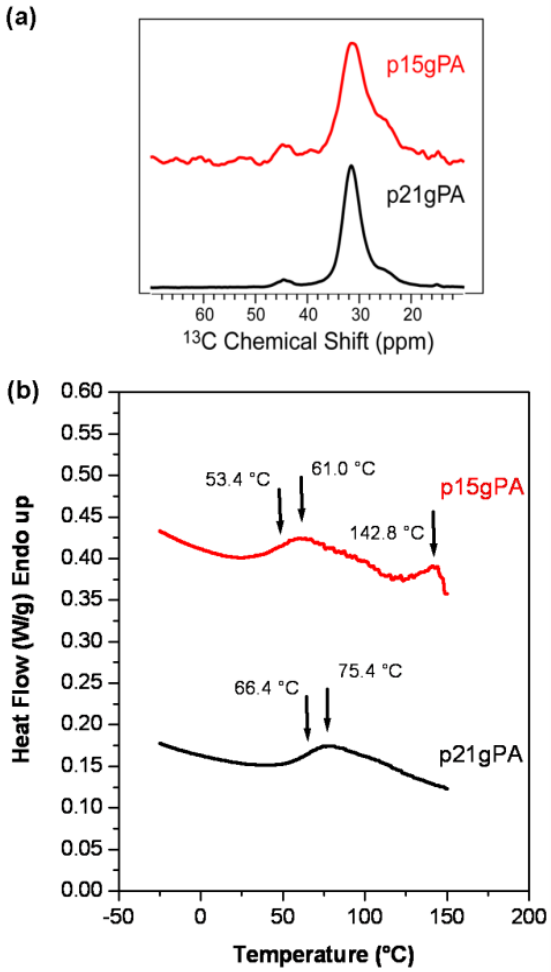

Figure 4.11 (a) ^{13}C CP MAS NMR spectra of copolymers with cubic morphologies. (b) DSC thermographs of p15gPA and p21gPA. The black arrows indicate weak thermal transitions.

Buitrago *et al.* recently published a detailed description of the morphology of p21gPA.[5] Within the spatial resolution of the MAXS facility at UPenn, we demonstrated that the microphase separated aggregates of PA arrange in a face-centered cubic (FCC) lattice. This morphology is confirmed in Figure 4.12 with the improved resolution of the

synchrotron X-ray scattering profile at room temperature. The lattice parameter ($a_{cub,\ FCC}$) of p21gPA, shown in Table 4.1, was determined using

$$d_{hkl} = \frac{a_{cub}}{\left(h^2 + k^2 + l^2\right)^{1/2}} \tag{4.1}$$

where d_{hkl} is the Bragg distance for each set of {h k l} Miller indices. The calculated lattice parameter from Figure 4.12 is $a_{cub,\ FCC}$ = 4.10 nm, within 2% of the previously reported $a_{cub,\ FCC}$.

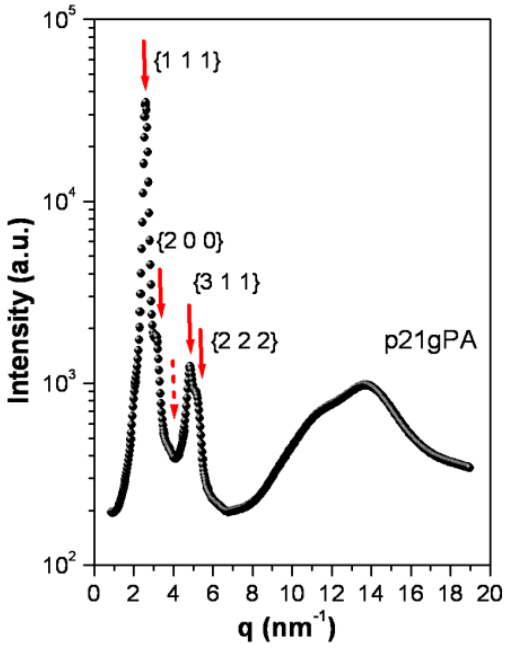

Figure 4.12 Room temperature synchrotron X-ray scattering of p21gPA, the precise copolymer with geminal PA groups on every 21st carbon. The solid red arrows indicate FCC ($a_{cub,\ FCC}$ = 4.10 nm) peaks observed in the pattern. The dotted arrow indicates the position of the expected {2 2 0} peak that coincides with a minimum in the form-factor of spherical aggregates of radius 1.1 nm.[5]

Synchrotron X-ray scattering also provided sufficient angular resolution to identify the morphology of p15gPA, the precise copolymer with two PA groups on every 15th carbon atom (Figure 4.13). Four distinct peaks with positional ratios (q/q^*) of 1:2:√5:√8 are observed at low q in the range between 2 – 10 nm^{-1}. These peak positions are consistent with both simple cubic (SC) and body-centered cubic (BCC) lattices of PA aggregates. These two crystal lattices are characterized by their nearly identical scattering profiles, with the most known difference being that the SC pattern does not allow the $q/q^* = \sqrt{7}$ peak. The observed peaks were used to extract $a_{cub,\ SC}$ and $a_{cub,\ BCC}$ from Eq. (4.1) assuming that the rest of the expected reflections (√2, √3, √6 and √9 in the case of SC and BCC; and √7 for BCC only) were undetected. The exceptional agreement of the data with both of these morphologies is illustrated by the inset in Figure 4.13.

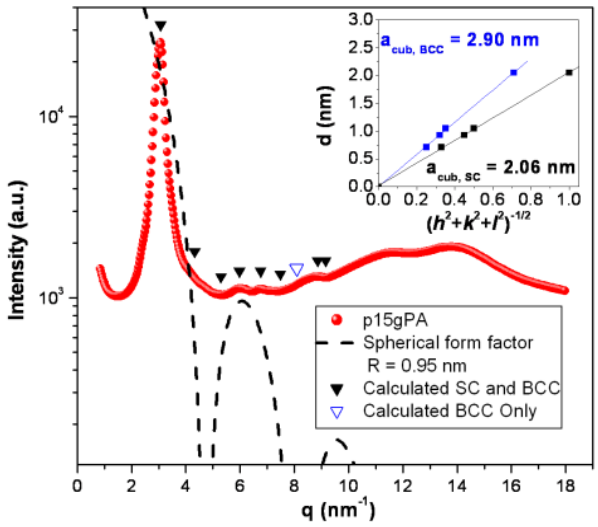

Figure 4.13 Synchrotron X-ray scattering of p15gPA, the precise material with geminal PA groups on every 15th carbon. The black triangles indicate the expected reflection for SC ($a_{cub,\ SC}$ = 2.06 nm) and BCC ($a_{cub,\ BCC}$ = 2.90 nm) lattices. For BCC, an additional expected peak is indicated with an open blue triangle. The inset shows the good agreement of equation (1) and the observed peaks with q/q* = 1:2:√5:√8. The two missing peaks corresponding to √3 and √6 match with minima in the form factor of spherical aggregates of radius ~ 0.95 nm (black dashed line).

The lattice parameters ($a_{cub,\ SC}$ and $a_{cub,\ BCC}$) were used to calculate the expected *q* positions of the first 9 allowed scattering reflections for both morphologies and are indicated by inverted triangles in Figure 4.13. For a cubic lattice, it is reasonable to approximate the PA aggregates as spheres. The nominal volume fraction of PA pendant groups in p15gPA from stoichiometry is ϕ_{p15gPA} = 0.35,[4] which was used to estimate the aggregate sizes for the simple and body-centered cubic lattices:

$$R_{agg,SC} = a_{SC}\left(\frac{3\phi_{p15gPA}}{4\pi}\right)^{1/3} \quad (4.2)$$

$$R_{agg,BCC} = a_{BCC}\left(\frac{3\phi_{p15gPA}}{8\pi}\right)^{1/3} \quad (4.3)$$

For SC packing $R_{agg,SC}$ is 0.90 nm and for BCC packing it is 1.00 nm, so the form factor scattering shown in Figure 4.13 corresponds to an intermediate radius of 0.95 nm. Two of the expected peaks at q = 4.33 and 8.09 nm^{-1} coincide with shoulders in the scattering data and are near the first minimum in the form factor scattering. The expected peaks at q = 5.30 and 7.49 nm^{-1} are missing from the scattering and coincide with the second minimum from the spherical form factor scattering. The radii calculated from Eq. 4.2 and Eq. 4.3 are sufficiently small to fit in the SC and BCC structures with the lattice parameters reported in Table 4.1. The structural characterization of the cubic morphology found in p21gPA was facilitated by stretching the material to form an anisotropic structure. Regrettably, the p15gPA sample exhibited very low ductility at all reasonable temperatures to avoid degradation. Thus, we conclude that p15gPA consists of PA aggregates in either a SC or BCC lattice. The copolymer p15gPA is only the second PE-based acid-containing copolymer to display a cubic lattice.

From the results to date, we find that both geminal substitution and a PA pendant are required to produce a cubic morphology. Note that p21gAA forms a layered morphology, as dictated by PE crystallization. While carboxylic acid groups can form only two H-bonds, phosphonic acids can form three, thereby causing additional steric hindrances, particularly when combined with geminal substitution. The steric hindrance

caused by geminal PA pendants is sufficient to suppress PE crystallization in both p15gPA and p21gPA. The PE segments in these copolymers appear to be sufficiently long to allow the PA aggregates to assemble into a periodic cubic lattice.

4.4 Conclusions

The room temperature morphologies are reported for twelve PE-based precise copolymers with carboxylic acid, phosphonic acid, or imidazolium bromide pendant groups. The morphologies were categorized by the symmetry of the acid- or ion-aggregates to be liquid-like, layered, or cubic morphologies as summarized in Table 4.1.

1) The liquid-like morphologies exhibit amorphous PE which is typical when the PE spacer is short corresponding to high pendant content. The characteristic interaggregate spacing in this morphology type increases with both the length of the PE spacer and the size of the pendant group. These room temperature liquid-like morphologies are comparable to the liquid-morphologies that dominate at elevated temperatures.
2) The layered morphologies were found to be highly susceptible to alignment by stretching, which was used to distinguish two categories of layered morphologies. In the AA and PA copolymers with a long PE segments (21 carbons), PE crystallization dominates the morphology and acid aggregates decorate the surfaces of the lamellae. In these materials, stretching the samples aligns the polymer chains such that the acid layer aggregates are perpendicular to the stretch direction. In contrast, when the interaction between pendants is stronger, as found

for ImBr groups, the aggregates form layers as a response to the deformation, and the PE subsequently crystallizes with the PE segments perpendicular to the stretch direction. The layered morphologies dominate when the PE segments are long and are strongly influenced by the pendant type.

3) Two precise copolymers exhibit cubic symmetry. The steric hindrance resulting from PA pendants with three H-bonding sites and geminal substitution appear to be required for this novel morphology with unprecedented symmetry for an acid-containing polymer.

Finally, we reiterate that these morphologies are distinguishable in part due to the remarkable molecular control afforded by ADMET polymerization. Looking forward, the impact of other pendant groups, particularly sulfonic acids, would be of interest, as well as how these distinct morphologies impact mechanical and transport properties both at room and elevated temperature. *In situ* mechanical testing and X-ray scattering of some of these materials are already underway, and the resulting data will further elucidate the fundamental structure-property relationships in these model materials to facilitate the rational design of specialty polymers.

4.5 References

1. Baughman, T. W.; Chan, C. D.; Winey, K. I.; Wagener, K. B. *Macromolecules* **2007,** 40, (18), 6564-6571.

2. Opper, K. L.; Markova, D.; Klapper, M.; Mullen, K.; Wagener, K. B. *Macromolecules* **2010,** 43, (8), 3690-3698.

3. Aitken, B. S.; Buitrago, C. F.; Heffley, J. D.; Lee, M.; Gibson, H. W.; Winey, K. I.; Wagener, K. B. *Macromolecules* **2012,** 45, 681-687.

4. Buitrago, C. F.; Alam, T. M.; Opper, K. L.; Aitken, B. S.; Wagener, K. B.; Winey, K. I. *Macromolecules*, Submitted.

5. Buitrago, C. F.; Opper, K. L.; Wagener, K. B.; Winey, K. I. *ACS Macro Lett.* **2012,** 1, (1), 71-74.

6. Seitz, M. E.; Chan, C. D.; Opper, K. L.; Baughman, T. W.; Wagener, K. B.; Winey, K. I. *J. Am. Chem. Soc.* **2010,** 132, (23), 8165-8174.

7. Massiot, D.; Fayon, F.; Capron, M.; King, I.; Le Calve, S.; Alonso, B.; Durand, J. O.; Bujoli, B.; Gan, Z. H.; Hoatson, G. *Magn. Reson. Chem.* **2002,** 40, (1), 70-76.

8. Heiney, P. A. *Comission on Powder Diffraction Newsletter* **2005,** 32, 9-11.

9. Jenkins, J. E.; Seitz, M. E.; Buitrago, C. F.; Winey, K. I.; Opper, K. L.; Baughman, T. W.; Wagener, K. B.; Alam, T. M. *Polymer* **2012,** 53, 3917-3927.

10. Brandrup, J.; Immergut, E. H., *Polymer Handbook*. John Wiley & Sons: New York, 1989.

11. Eisenberg, A.; Kim, J.-S., *Introduction to Ionomers*. 1st ed. ed.; Wiley: New York, 1998.

12. Sworen, J. C.; Smith, J. A.; Berg, J. M.; Wagener, K. B. *J. Am. Chem. Soc.* **2004,** 126, (36), 11238-11246.

13. Taubert, A.; Winey, K. I. *Macromolecules* **2002,** 35, (19), 7419-7426.

14. Benetatos, N. M.; Smith, B. W.; Heiney, P. A.; Winey, K. I. *Macromolecules* **2005,** 38, (22), 9251-9257.

15. Elaiwi, A.; Hitchcock, P. B.; Seddon, K. R.; Srinivasan, N.; Tan, Y. M.; Welton, T.; Zora, J. A. *J. Chem. Soc.-Dalton Trans.* **1995**, (21), 3467-3472.

16. Yan, S. K.; Lieberwirth, I.; Katzenberg, F.; Petermann, J. *J. Macromol. Sci.-Phys.* **2003,** B42, (3-4), 641-652.

17. Bradley, A. E.; Hardacre, C.; Holbrey, J. D.; Johnston, S.; McMath, S. E. J.; Nieuwenhuyzen, M. *Chem. Mat.* **2002,** 14, (2), 629-635.

Chapter 5

Direct Comparisons of the Morphologies of Precise Ionomers as Predicted by X-ray scattering and Atomistic MD Simulations

5.1 Introduction

In spite of the long standing interest of polymer scientists in ionomers, a definitive picture of their morphologies has not been attained by current experimental methods.[1,2] Among the biggest impediments hindering success in this objective are the structural heterogeneity of traditional ionomers and the inherent difficulty to obtain direct images of their nanoscale morphologies. Lately, a significant advance towards overcoming these obstacles was made by the successful synthesis of polyethylene (PE)-based precise ionomers via acyclic diene metathesis (ADMET) polymerization.[3-6] In contrast to the structurally irregular commercial PE-based ionomers synthesized by high-pressure free radical polymerization, the ADMET materials feature a strictly linear polymer chain functionalized with carboxylate anions at precise sequences of carbon atoms.

The structural regularity and simplicity of ADMET ionomers have resulted in an unprecedented improvement in the quality of data obtained by common experimental characterization techniques such as X-ray scattering, DSC and ^{13}C NMR.[3,4,7,8,9] For instance, Zn-neutralized precise AA ionomers feature much sharper and more intense X-ray scattering peaks in comparison to commercial ionomers.[4] In the case of unneutralized acid copolymers, the precise AA materials have an X-ray scattering inter-aggregate separation peak that is absent in the commercial varieties.[3,9] In addition, DSC and ^{13}C

NMR data suggest that precise copolymers with halogen pendants undergo a crystallization process typical of homopolymers due to the large crystalline regions, and to the uniform distribution of the halogens between the crystalline and amorphous phases.[7,8]

Extracting a quantitative description of the morphologies from scattering profiles relies on analytical models based on simplifying geometrical assumptions. The most common model used in the interpretation of ionomer morphology is the Modified Hard-Sphere (MHS) model, which assumes monodisperse spherical ionic aggregates with liquid-like order and a separation of closest approach that is greater than the aggregate diameter.[10-13] To implement the MHS model, it is advisable to validate its assumptions through direct visualization of aggregates. High-angle annular dark-field scanning transmission electron microscopy (HAADF-STEM) has been successfully implemented for direct imaging of ionic aggregates in some ionomer systems.[14-22] This technique captures micrographs that are two-dimensional projections of ionic aggregates (~ 1 nm) densely arranged in 3-D and featuring a considerable amount of overlap between the aggregates. Thus, compact aggregates may be indistinguishable from elongated ones in the transmission images, especially because the micrographed samples are typically ≥ 50 nm. Therefore, transmission electron microscopy methods are prone to distorting the size and arrangement of ionic aggregates.

The development of precise ionomers has allowed for the use of simulation methods to complement the morphological information obtained from experimental techniques.[23-26] Since precise ionomers are structurally simple and homogeneous, they

serve as model materials for molecular dynamics (MD) simulations. Atomistic MD simulations of precise ionomer systems provide real-space representations that serve as alternatives to direct imaging of ionomer morphology through microscopy. Recently, coarse-grain and atomistic MD simulations have suggested that the assumption of monodisperse, spherical aggregates in melt ionomer morphology is unrealistic in many cases.[23-26] Instead, a wide variety of aggregate morphologies have been reported depending on the frequency of pendant groups along the polyethylene chain, the architecture of the pendant groups, and the type of neutralizing cation. Among those morphologies, there is a prevalence of string-like aggregates, which can percolate the simulation boxes at higher ionic contents.

In this work, we study the melt morphology of three precise poly(ethylene-*co*-acrylic acid) copolymers and eight precise ionomers by X-ray scattering and atomistic MD simulations. Direct comparisons of X-ray scattering profiles with the structure factors of simulated systems are in excellent agreement and confirm that these techniques complement one another. In addition, the suitability of the MHS model is tested and contrasted with a new model for string-like or cylindrical ionic aggregates.

5.2 Experimental Methods

5.2.1 Materials: Linear poly(ethylene-*co*-acrylic acid) copolymers with precise comonomer distribution were synthesized via ADMET polymerization. These precise copolymers are denoted pxAA (x = 9, 15 or 21), where x indicates the number of carbons in the PE segment per acid functionalization. Details of their synthesis and

characterization have been previously described.[3] A general neutralization procedure begins by dissolving the precise AA copolymers in a 1:4 mixture of 1,4-dioxane and 1-butanol (30mL) under nitrogen. A magnetic stir bar was added and complete dissolution was obtained upon heating at 90°C for 3 hours. During that time, 0.44 mmol of the metal salt was weighed under a dry and inert atmosphere. Lithium and sodium acetate salts were soluble in 1:2 mixtures of 1,4-dioxane and 1-butanol while cesium acetate was soluble in 1:1 mixtures of 1,4-dioxane and 1-butanol. For complete dissolution, a small stir bar was added, the vial closed and heated to 90°C for 30 minutes. The salt solution was added to the addition funnel and was allowed to drip dropwise into the vigorously stirring polymer solution at 90°C. Cloudiness was observed upon partial addition. After stirring for 3 hours at 90°C and cooling to room temperature, the fine precipitate coagulated into larger pieces. No further changes or additions in solvent were necessary. Lithium and sodium precipitate were free while cesium precipitate adhered to the bottom of the flask. The precipitate was filtered and dried at 80°C overnight.

The extent of neutralization achieved from the solution neutralization procedure was determined by inductively coupled plasma elemental analysis performed by Galbraith Laboratories (Knoxville, TN) on samples with masses ranging from 5 – 21 mg. The error is estimated at ~7 % in the reported mol % neutralization. The neutralized samples are denoted with *y*M where *y* is the mol% neutralization determined from the elemental analysis and M stands for the neutralizing cation (Zn, Li, Na, or Cs). The materials studied are summarized in Table 5.1.

5.2.2 X-ray Scattering: The X-ray scattering apparatus consists of a Nonius FR591 rotating-anode generator operated at 40 kV × 85 mA, pin-hole focusing optics, an evacuated flight path, and a Bruker HiSTAR multiwire two-dimensional detector. Data were acquired at sample-detector distances of 9 cm, corresponding to a q ($q=(4\pi/\lambda)\sin\theta$) range of ~1-17 nm^{-1}. 2D data reduction, analysis and MHS model fitting were performed using the Datasqueeze software.[27] For temperature studies, sample-filled capillaries were loaded into a Linkham oven and temperature was controlled via a Linkham TMS 94 temperature controller. Samples were heated at 10 °C/min from room temperature to 120 °C and held at least 5 minutes prior to data collection to ensure thermal equilibrium was achieved. Data were collected for 1 hour at each temperature. An empty capillary was run under the same conditions and was used for background subtraction. Calibration of the scattering vector (q) was done using silver behenate.

5.2.3 Scattering Models: The models used to acquire quantitative information from X-ray scattering profiles and from simulated structure factors are described below. Since these two expressions are equivalent, $I(q)$ will be used to refer to both. The general form of the models is the following:

$$I(q) = I_{Model}(q) + I_L(q) + C \tag{5.1}$$

where $I_{Model}(q)$ is the model used to fit the aggregate peak, $L_1(q)$ is a Lorentzian used to capture the polyethylene amorphous halo and C is an constant that accounts for instrumental background. The form of the MHS model ($I_{MHS}(q)$), which approximates acid and ion rich aggregates as spheres, has been described elsewhere.[10-13] The

independent fitting parameters for the MHS model are the aggregate radius R, the radius of closest approach R_{ca}, and the number density of aggregates n.

A new model is introduced here that approximates the geometry of the aggregates as cylinders rather than spheres; therefore, we will call it the modified hard-cylinder (MHC) model. The expression for the MHC model ($I_{MHC}(q)$) is a multiplicative function composed of expressions for the form factor ($P(q)$), the structure factor ($S(q)$) and the overall magnitude of the intensity (A). The form factor for a cylinder of radius R and length L is the following:[28]

$$P(q) = \int_0^{\pi/2} d\alpha \left[\frac{2J_1(qR\sin\alpha)}{qR\sin\alpha} \frac{\sin\left(\frac{1}{2}qL\cos\alpha\right)}{\frac{1}{2}qL\cos\alpha} \right]^2 \sin\alpha \tag{5.2}$$

where $J_1(x)$ is the first order Bessel function. The structure factor is motivated by the work of Gapinski *et al.* who used a structure factor from the PRISM theory for polymers,[29] and the resulting expression is:

$$S(q) = \frac{1}{1 + \beta\Phi(2qR_{ca})P_o(q, L - 2R_{ca})} \tag{5.3}$$

in this expression, P_o is the form factor for an infinitely thin rod:[28]

$$P_o(q, L) = \frac{2}{qL^2}\left[qLSi(qL) + \cos(qL) - 1\right] \tag{5.4}$$

$Si(x)$ is the sine integral:

$$Si(x) = \int_0^x \frac{\sin t}{t} dt \tag{5.5}$$

and

$$\Phi(x) = 3\frac{\sin(x) - x\cos(x)}{x^3} \tag{5.6}$$

Finally, $\beta = (1 - S(0))/S(0)$. If we think of the scattering as being literally from a bunch of rods, the value for $S(0)$ from the literature can be used:[30]

$$S(0) = \frac{(1 - B - C)^4}{(1 + 2(B + C))^2 + 2D(1 + B + 5C/4)} \tag{5.7}$$

where $B = \pi R_{ca}^2 Ln$, $C = 4\pi R_{ca}^3 n/3$, $D = \pi R_{ca} L^2 n/2$, and n is the number density of the rods. In addition to the fitting parameters R, R_{ca} and n; the MHC model also estimates the cylindrical length L.

5.3 Simulation Methods

Simulations were performed by Dr. Dan Bolintineanu, Dr. Mark Stevens and Dr. Amalie Frischknecht at Sandia National Laboratories. All p9AA systems contained 200 polymer molecules, while the p15 and p21 copolymers contained 120 and 80 molecules, respectively. In all cases, all polymer molecules contained four repeat units. All simulations were carried out using the OPLS-AA fully atomistic force field.[31] Lithium, sodium and cesium nonbonded parameters correspond to values given by Jensen and Jorgensen,[32] whereas zinc parameters were obtained from the work of Hoops *et al*.[33] The LAAMPS software package was used for all simulations,[34] with a real-space nonbonded cutoff of 12 Å and the particle-particle particle-mesh (PPPM) solver for electrostatics.[35] A Langevin thermostat with a 100 fs damping parameter was used to maintain a constant temperature of 120 °C. The integration time step was set to 1.0 fs in all cases. All systems were constructed by initially placing polymer chains and free ions in random locations on a simple cubic lattice at a low density. The simulation box was subsequently isotropically compressed to a density of approximately 1 g/cm^3 during 0.5 ns of simulation time. An

additional 2 ns simulation was carried out at a constant pressure of 1 atm in the *NPT* ensemble to allow each system to reach its equilibrium density. The equilibrated dimensions of the cubic simulation boxes ranged from 60 to 65 Å per side. The box dimensions were subsequently fixed, and production runs were carried out in the *NVT* ensemble for at least 35 ns for each system. In all cases, the first 5 ns were discarded for the purposes of the subsequent analyses. Unless otherwise stated, sampling for all the analyses was carried out at 10 ps intervals.

Structure factor profiles are calculated from the simulations and represent an average morphology throughout the runs. These structure factors include atomic scattering factors, which enables direct comparisons to X-ray scattering data. Therefore, although simulated structure factors are commonly denoted as $S(q)$, the general symbol for scattering intensity $I(q)$ will be used here to facilitate comparisons. The total structure factor is computed from Fourier transforms of the pairwise radial distribution functions:

$$I(q) = S(q) = \sum_i c_i f_i^2 + 4\pi\rho \int_0^\infty \frac{\sin(qr)}{qr} r^2 \sum_{i,j} c_i c_j f_i f_j (g_{ij}(r) - 1) dr \tag{5.8}$$

here, i and j are indices used to count atomic species (four in this case: counterion, oxygen, carbon and hydrogen), g_{ij} is the radial distribution function between species i and j, ρ is the total number density of the system, c is the mole fraction and f is the atomic scattering function for each species. The atomic scattering functions f_i are based on the empirical fits of Waasmaier and Kirfel,[36] which take the form:

$$f_i = a_i + \sum_{k=1}^{5} b_{ik} \exp(-d_{ik}(q/4\pi)^2) \tag{5.9}$$

where a_i, b_{ik} and d_{ik} are tabulated sets of coefficients for each atomic (ionic) species i.

5.4 Results and Discussion

The eleven materials discussed in this study are summarized in Table 5.1. Their morphologies were studied at 120 °C by X-ray scattering and atomistic MD simulations. In the simulations, acid- and ion-rich aggregates only consist of oxygens, hydroxyl hydrogens and neutralizing cations. One aggregate is defined as containing at least two hydrogens or metal cations. Morphology characterizations for all materials, performed by visual inspection of the real space simulation snap shots, are also reported in Table 5.1. Depending on the shape and size of the aggregates, the materials are sorted into the following categories:[25,26] "compact, isolated" (CI), "short, stringy" (SS), "long, stringy" (LS), "partially percolated" (PP) and "fully percolated" (FP).

Table 5.1 Precise Acid Copolymers and Ionomers Synthesized by ADMET Polymerization and Characterized at 120 °C

Sample #	Nomenclature	Real Space Morphology[a]
1	p9AA	SS/CI
2	p9AA-43%Li	LS
3	p9AA-33%Na	LS/PP
4	p9AA-24%Cs	FF/PP
5	p15AA	SS/CI
6	p15AA-45%Li	SS
7	p15AA-34%Na	LS/SS
8	p15AA-31%Cs	LS/SS
9	p15AA-82%Zn	CI/SS
10	p21AA	CI/SS
11	p21AA-56%Zn	CI

[a] Real space morphologies obtained by visual inspection of the simulation images. Abbreviations are as follows: "compact, isolated" (CI); "short, stringy" (SS); "long, stringy" (LS); "partially percolated" (PP); "fully percolated" (FP).

MD simulations and X-ray scattering data for selected systems that illustrate the different aggregate morphologies are shown in Figure 5.1. The snap shots used to characterize the real space morphologies from the simulations are shown in Figure 5.1a-c. Only the atoms present in aggregates are shown, and the different colors represent distinct aggregates. The system p21AA-56%Zn in Figure 5.1a has a comparatively small content of aggregates because it features long PE spacers (effectively decreasing the number of functional groups) and is neutralized with divalent cations (Zn^{+2}). These factors limit aggregate size to produce CI aggregates by visual inspection. A system

featuring shorter spacer lengths and partial neutralization with small monovalent cations (Li^+) is shown in Figure 5.1b, p9AA-43%Li. These larger aggregates are elongated to efficiently exclude non-polar segments and avoid unfavorable entropic configurations of the PE chains.[25] Consequently, this system is composed of extended, branched aggregates characterized as LS. Figure 5.1c depicts a system with short PE segments and neutralized with large cations (Cs^+), p9AA-24%Cs. This system features percolated aggregate networks (PP/FP).

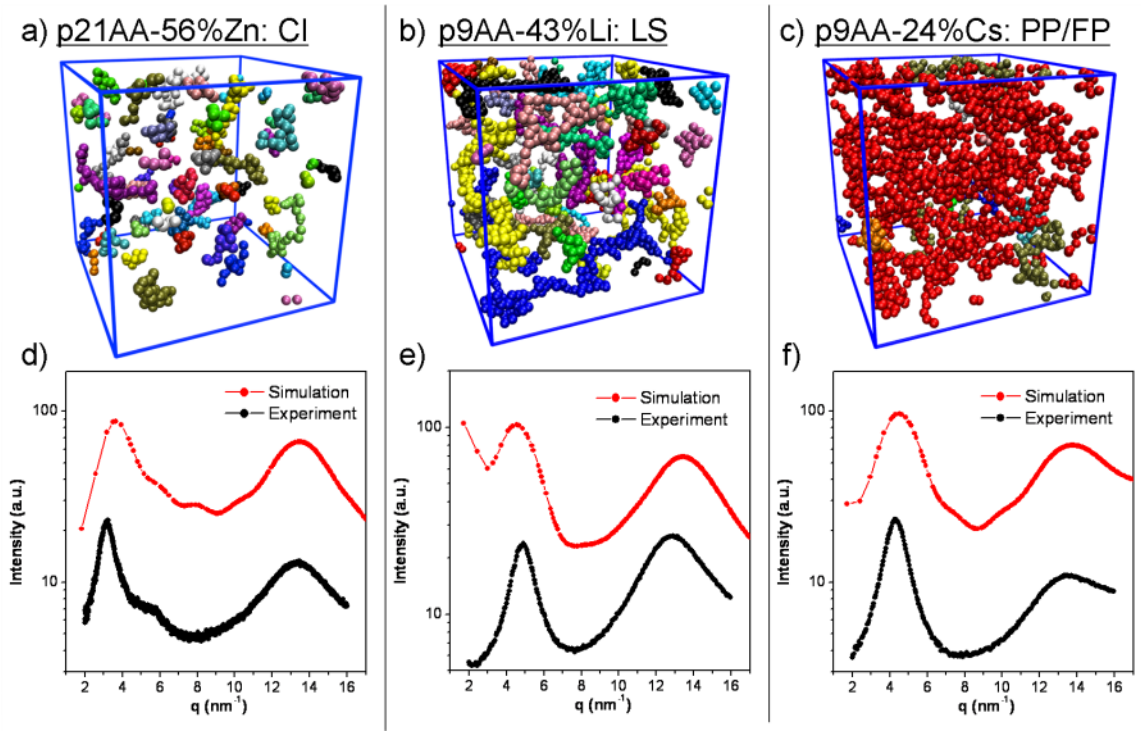

Figure 5.1 Morphology data from simulations and experiments. (a-c) Snap shots from simulated systems after ~35 ns at 120 °C. Only aggregates with two or more counterions are shown. Different colors represent distinct aggregates. (d-f) Comparisons of structure factor profiles extracted from simulations (red) and X-ray scattering profiles from experiments (black) at 120 °C. Intensity shifted for clarity.

Structure factors from simulations and X-ray scattering profiles from experiments are presented in Figure 5.1d-f. As noted in Section 5.3, these expressions represent equivalent reciprocal space data, and therefore both will be denoted as $I(q)$. Despite the three distinct real-space morphologies in Figure 5.1a-c, the I(q) profiles in Figure 5.1d-f are remarkably similar. The reciprocal space data feature both a prominent aggregate peak at $q^*_{agg} \sim 3 - 6$ nm^{-1}, and a broad amorphous halo at $q^*_{am} \sim 13$ nm^{-1}. The aggregate

peak has previously been proven by coarse-grained MD simulations to arise from inter-aggregate scattering in the case of CI aggregates, and from inter- and intra-aggregate scattering for extended stringy aggregates.[23] Previous simulations of precise ionomers have demonstrated that the *d*-spacings ($d^* = 2\pi/q^*$) from aggregate peaks are dictated by the precise polyethylene segments forming bridges and close loops between aggregates.[23]

In order to justify the complementary use X-ray scattering and MD simulations, the peak positions and relative intensities of the I(q) profiles obtained from both methods must be compared. Quantitative data from scattering models and from the real-space snap shots also add confidence to the analysis of the morphologies. The positions of the maxima for the aggregate peaks (q^*_{agg}) and the amorphous halos (q^*_{am}) in all of the tested systems show excellent agreement between experiments and simulations, Figure 5.2. Note that the discrepancy found in Fig. 5.2b corresponds to the simulations overestimating q^*_{am} by 4%, which corresponds to ≤ 0.02 nm in real space at the high angle region. Due to this spectacular reproduction of the experimental data by the simulations, it is reasonable to conclude that despite the similarities between the X-ray scattering profiles in Figure 5.1d-f, the morphologies of the experimental systems vary as a function of spacer length, counterion and neutralization level in the same manner as the simulated snap shots (Figure 5.1a-c).

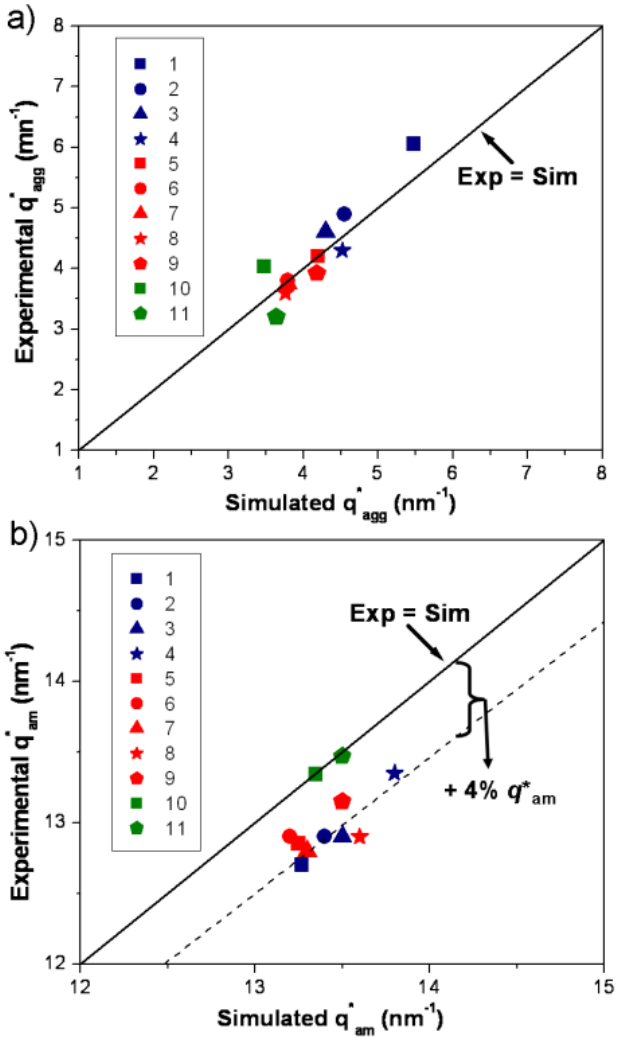

Figure 5.2 Peak maxima correspondence for (a) the aggregate peak (q^*_{agg}) and (b) the amorphous halo (q^*_{am}) between experimental and simulated ionomer systems. The legend indicates each sample by the numbers given in Table 5.1. Blue, red and green markers correspond to p9, p15 and p21 materials, respectively.

While there is excellent agreement in q^*_{agg} and q^*_{am} between simulated and experimental I(q) profiles, subtle differences exist in the broadness of the aggregate peaks

and in the relative intensity of the aggregate peaks with respect to the amorphous halos. Currently, there is no definitive reason to explain the differences in aggregate peak broadness. It is likely that the force-fields posses limited capabilities to completely replicate experimental data. In addition, the simulation boxes (~ 220 nm^3) are much smaller than the volume probed by X-ray scattering (~ 0.5 mm^3). Therefore, while the predicted ionic aggregates have satisfactory shape and separations as evidenced by the correspondence in q^*, the sampling in the simulation boxes is too small to obtain a sharper distribution of those features. The comparison of relative intensities (I^*_{agg}/I^*_{am}) between simulations and experiments is shown in Figure 5.3. With a few exceptions, the comparison points are within ~ 30% from the x = y line indicating strong agreement. System 8 (p15AA-31%Cs) deviates by ~ 60%. Whereas there is excellent agreement for the acid forms (squares), there is a trend of increasing I^*_{agg}/I^*_{am} in the experiments as the ionomer neutralizing cation varies from Li (circles) to Na (triangles) to Cs (stars). However, this tendency is not observed in the simulations, pointing out to a possible source of systematic error. At the moment, we do not have a definitive reason for these differences.

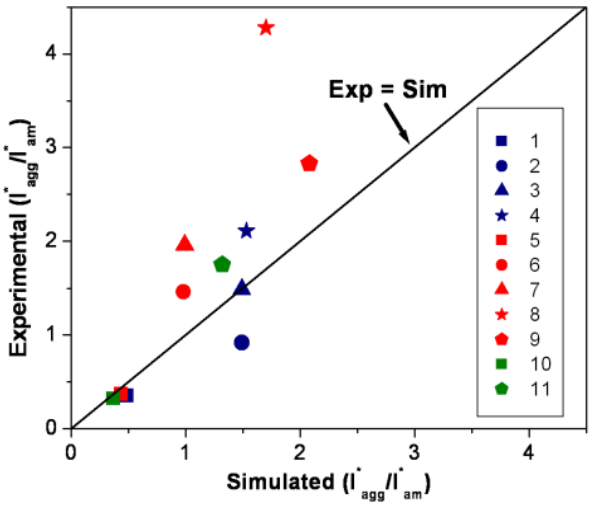

Figure 5.3 Relative intensity of the ionomer peak (I^*_{agg}) with respect to the amorphous halo (I^*_{am}) for precise acid copolymers and ionomers obtained from experiments and simulations. Blue, red and green markers correspond to p9, p15 and p21 materials, respectively.

Next, we fit I(q) profiles from atomistic MD simulations and from X-ray scattering experiments to analytical models of the morphologies and compare them to cluster analysis from the simulations. While representative figures will be presented to illustrate the discussion points, atomistic MD simulation data and X-ray scattering from all the systems in Table 5.1 are available in Appendix D. Two analytical models have been utilized, approximating ionic aggregates as being either spherical (MHS) or cylindrical (MHC). As illustrated in Figure 5.4 for a system with CI/SS morphology (p15AA-82%Zn), the MHS model can fit both simulated and experimental I(q) profiles. In particular, visual inspection of Figure 5.4c reveals that the MHS model captures the sharp main peak and the shoulder at ~ 6.8 nm^{-1} in the experimental data. We expect that

the spherical model can describe SS morphologies better than the cylindrical model because the SS aggregates are more compact than isolated in the time-averaged simulations.

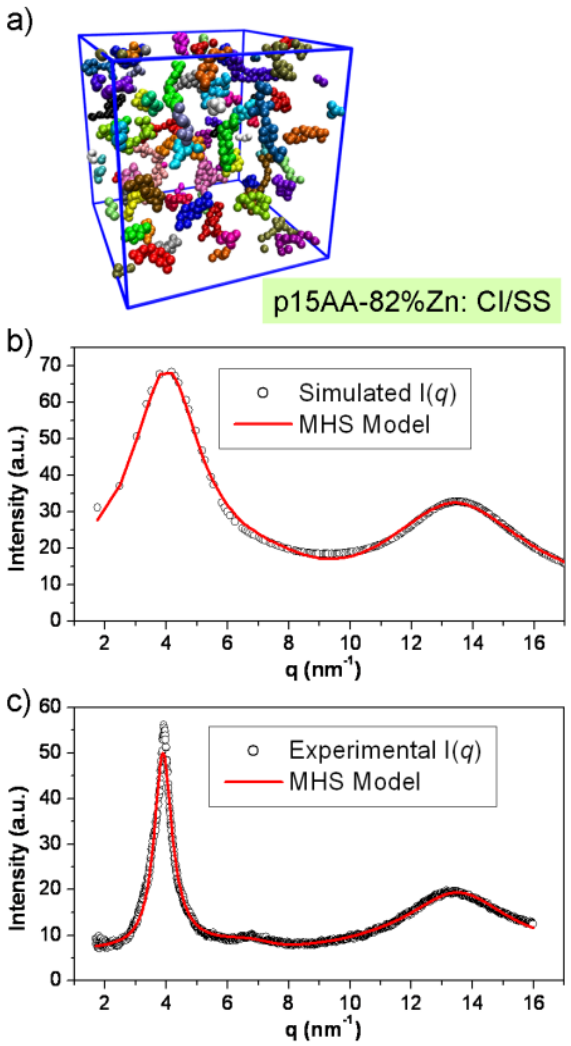

Figure 5.4 (a) Real-space CI/SS morphology of p15AA-82%Zn. Spherical (MHS) model fit to (b) Simulated and (b) experimental I(q) profiles.

A comparison of the quantitative data from the MHS model to simulated and experimental p15AA-82%Zn (CI/SS) and p21AA-56%Zn (CI) is shown in Table 5.2. The data obtained from these fits are compared to values acquired from the simulated real-space systems. As expected from the overall shape of the I(q) profiles, the MHS model results in slightly different parameters for experiments and simulations. For both systems and relative to the experiments, the simulations underestimate R by 24% and R_{ca} by 19%. Conversely, although both models predict comparable values for n, there is no clear trend in their deviation. Comparisons to real space cluster analysis support the accuracy of the parameters calculated from the MHS model.

Table 5.2 MHS Fit Parameters from X-ray Scattering and Atomistic MD Simulations Compared to Cluster Analysis from Real Space Simulations

	p15AA-82%Zn (CI/SS)			**p21AA-56%Zn** (CI)		
	MHS Model		Real-space Sim.	MHS Model		Real-space Sim.
	Exp.	Sim.		Exp.	Sim.	
R (nm)	0.50	0.38	0.41	0.50	0.37	0.46
R_{ca} (nm)	0.88	0.72	0.76	1.02	0.82	1.01
n (nm^{-3})	0.17	0.15	0.14	0.09	0.12	0.04

The real-space image in Figure 5.4a suggests the adequacy of the MHS model to describe p15AA-82%Zn. If such an image were not available, the cylindrical (MHC) model could be forced through the data. As revealed just by visual inspection of Figure 5.5, p15AA-82%Zn is not well-described by this model. More importantly, the cylindrical model predicts parameters that deviate considerably from real-space: R (0.32

nm), R_{ca} (0.65) and n (0.05) deviate from the real-space values by 22%, 14% and 64%, respectively.

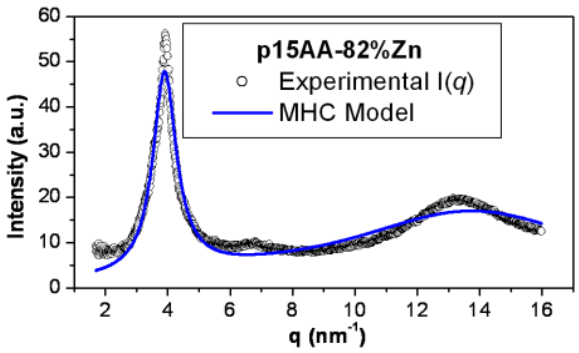

Figure 5.5 X-ray scattering of p15AA-82%Zn fit with the MHC model (blue line).

When atomistic MD generates LS, PP or FP aggregate morphologies, the MHC model is expected to yield more realistic numerical values than the MHS model. Figure 5.6 illustrates examples of the MHC model fit to a system with LS morphology, p9AA-43%Li. Quantitative data obtained form experimental and simulated I(q) using the MHC model for p9AA-43%Li (LS) and p9AA-33%Na (LS/PP) are shown in Table 5.3. Again, the experimental and simulated values from the fit are in good agreement, except for the parameter L which can be regarded as a persistence length for extended aggregates. The calculated L from the simulations is extremely unreliable because the box size is just ~ 6 nm per side.

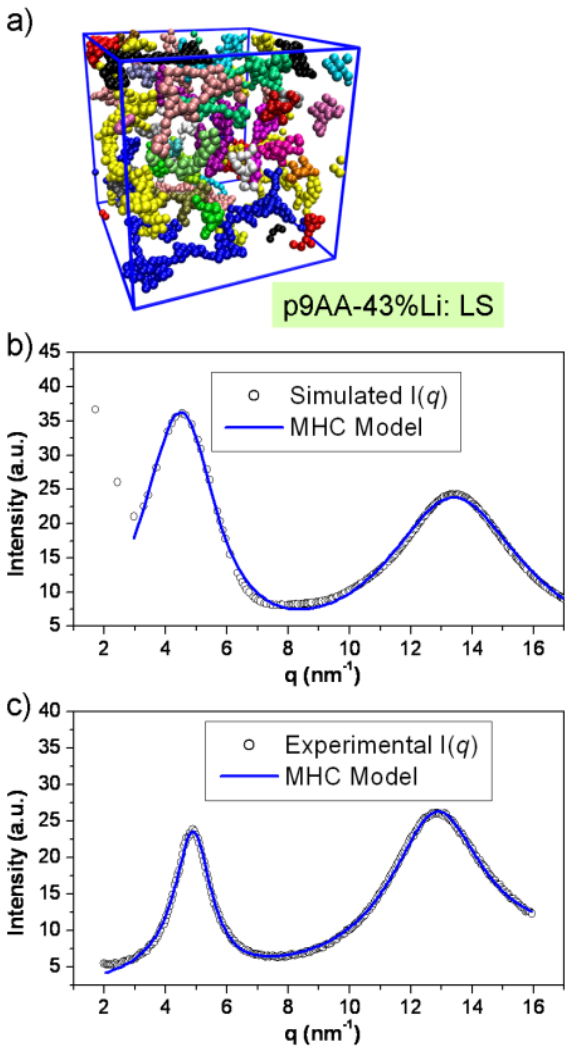

Figure 5.6 (a) Real-space LS morphology of p9AA-43%Li. Cylindrical (MHS) model fit to (b) Simulated and (b) experimental I(q) profiles.

Table 5.3 MHC Fit Parameters from X-ray Scattering and Atomistic MD Simulations

	p9AA-43%Li (LS)		**p9AA-33%Na** (LS/PP)	
	MHC Model		MHC Model	
	Exp.	Sim.	Exp.	Sim.
R (nm)	0.37	0.34	0.37	0.34
R_{ca} (nm)	0.51	0.51	0.55	0.52
L (nm)	4.94	3.24	5.28	3.43
n (nm^{-3})	0.11	0.12	0.09	0.10

Unfortunately, real space cluster analysis cannot be carried out in string-like systems because the aggregates often stretch out of the simulation boxes and their center of mass cannot be calculated accurately. However, representative manual measurements from the LS p9AA-43%Li are consistent with the MHC model. In particular, Table 5.3 indicates that R is 0.34 nm and R_{ca} is ~ 51 nm for the MHC model. The MHS model can also be force fit to this system, yielding R ~ 0.45 nm and R_{ca} ~ 66 nm. A close look to an aggregate from the p9AA-43%Li simulated system in Figure 5.7a shows specific aggregate radii of 0.17 nm and 0.28 nm, although it is clear from the illustration that R can be slightly larger. That picture coincides more with the MHC model than with the MHS model. In Figure 5.7b, several inter- and intra-aggregate distances from simulated p9AA-43%Li are shown. Since those aggregates are elongated, the distances are measured from the interior of random segments of the aggregates. Distances of 1.32, 1.49 and 1.25 nm are measured, corresponding to radii of 0.66, 0.745 and 0.625. At least one of those inter-aggregate radii are smaller than R_{ca} from the MHS model for p9AA-43%Li

(0.66nm). R_{ca} from the MHC model (0.51 nm) appears to be more consistent with the aggregates in Figure 5.7.

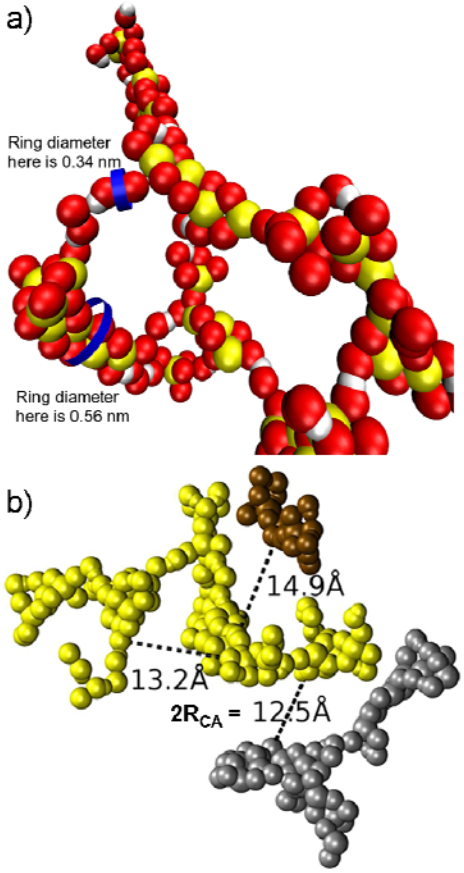

Figure 5.7 Close-up to aggregates from p9AA-43%Li. (a) Aggregate diameters, corresponding to 2R, are explicitly indicated. (b) Inter- and intra-aggregate distances measured from the interior of the aggregates are indicated. These distances correspond to $2R_{ca}$. Illustrations courtesy of Dan S. Bolintineanu.

5.5 Conclusions

The melt morphology of three precise AA copolymers and eight ionomers obtained by neutralizing them with Zn, Li, Na and Cs are studied by X-ray scattering and atomistic MD simulations. The simulations predict that the aggregate shapes can vary from compact to stringy to percolated in these systems. The aggregate shape can change as a function of PE segment length, cation type and level neutralization. Direct comparisons of experimental X-ray scattering profiles and the structure factors from the simulations are in excellent agreement. This concurrence suggests that precise AA copolymers and ionomers form aggregates that can range from compact, isolated to stringy to percolated structures. However, it is not possible to determine the shape of the aggregates by X-ray scattering alone, as profiles from compact or stringy aggregates are often indistinguishable. Modeling the scattering profiles by approximating the aggregates as spheres (MHS) or cylinders (MHC) was completed and the fitting parameters compared to the real-space representations of the simulations. When real space snap-shots from simulations predict CI or SS morphologies, the MHS model fits the experimental and simulated data much better than the MHC model, and the values of R and R_{ca} are in good agreement with the real space simulations. While both the MHS and MHC models fit the I(q) data then the real space simulations exhibit string-like morphologies, the values of R and R_{ca} are more consistent with the simulated aggregates.

5.6 References

1. Eisenberg, A.; Kim, J.-S., *Introduction to Ionomers*. 1st ed. ed.; Wiley: New York, 1998.

2. Grady, B. P. *Polym. Eng. Sci.* **2008,** 48, (6), 1029-1051.

3. Baughman, T. W.; Chan, C. D.; Winey, K. I.; Wagener, K. B. *Macromolecules* **2007,** 40, (18), 6564-6571.

4. Seitz, M. E.; Chan, C. D.; Opper, K. L.; Baughman, T. W.; Wagener, K. B.; Winey, K. I. *J. Am. Chem. Soc.* **2010,** 132, (23), 8165-8174.

5. Opper, K. L.; Markova, D.; Klapper, M.; Mullen, K.; Wagener, K. B. *Macromolecules* **2010,** 43, (8), 3690-3698.

6. Aitken, B. S.; Buitrago, C. F.; Heffley, J. D.; Lee, M.; Gibson, H. W.; Winey, K. I.; Wagener, K. B. *Macromolecules* **2012,** 45, 681-687.

7. Alamo, R. G.; Jeon, K.; Smith, R. L.; Boz, E.; Wagener, K. B.; Bockstaller, M. R. *Macromolecules* **2008,** 41, (19), 7141-7151.

8. Boz, E.; Wagener, K. B.; Ghosal, A.; Fu, R. Q.; Alamo, R. G. *Macromolecules* **2006,** 39, (13), 4437-4447.

9. Buitrago, C. F.; Alam, T. M.; Opper, K. L.; Aitken, B. S.; Wagener, K. B.; Winey, K. I. *Macromolecules*, Submitted.

10. Yarusso, D. J.; Cooper, S. L. *Macromolecules* **1983,** 16, (12), 1871-1880.

11. Yarusso, D.; Cooper, S. L. *Polymer* **1985,** 26, (3), 371-378.

12. Kinning, D. J.; Thomas, E. L. *Macromolecules* **1984,** 17, 1712-1718.

13. Ding, Y. S.; Hubbard, S. R.; Hodgson, K. O.; Register, R. A.; Cooper, S. L. *Macromolecules* **1988,** 21, (6), 1698-1703.

14. Benetatos, N. M.; Chan, C. D.; Winey, K. I. *Macromolecules* **2007,** 40, (4), 1081-1088.

15. Batra, A.; Cohen, C.; Kim, H.; Winey, K. I. *Macromolecules* **2006,** 39, (4), 1630-1638.

16. Benetatos, N. M.; Winey, K. I. *J. Polym. Sci. Pt. B-Polym. Phys.* **2005,** 43, (24), 3549-3554.

17. Kirkmeyer, B. P.; Puetter, R. C.; Yahil, A.; Winey, K. I. *J. Polym. Sci. Pt. B-Polym. Phys.* **2003,** 41, (4), 319-326.

18. Kirkmeyer, B. P.; Weiss, R. A.; Winey, K. I. *J. Polym. Sci. Pt. B-Polym. Phys.* **2001,** 39, (5), 477-483.

19. Winey, K. I.; Laurer, J. H.; Kirkmeyer, B. P. *Macromolecules* **2000,** 33, (2), 507-513.

20. Taubert, A.; Winey, K. I. *Macromolecules* **2002,** 35, (19), 7419-7426.

21. Kirkmeyer, B. P.; Taubert, A.; Kim, J.-S.; Winey, K. I. *Macromolecules* **2002,** 35, (7), 2648-2653.

22. Benetatos, N. M.; Winey, K. I. *Macromolecules* **2007,** 40, (9), 3223-3228.

23. Hall, L. M.; Stevens, M. J.; Frischknecht, A. L. *Phys. Rev. Lett.* **2011,** 106, (12).

24. Hall, L. M.; Seitz, M. E.; Winey, K. I.; Opper, K. L.; Wagener, K. B.; Stevens, M. J.; Frischknecht, A. L. *J. Am. Chem. Soc.* **2012,** 134, (1), 574-587.

25. Bolintineanu, D. S.; Stevens, M. J.; Frischknecht, A. L. *ACS Macro Lett.* **2013,** 2, (3), 206-210.

26. Bolintineanu, D. S.; Stevens, M. J.; Frischknecht, A. L. *Macromolecules* **2013**.

27. Heiney, P. A. *Commission on Powder Diffraction Newsletter* **2005,** 32, 9-11.

28. Pedersen, J. S. *Adv. Colloid Interface Sci.* **1997,** 70, 171-210.

29. Gapinski, J.; Szymanski, J.; Wilk, A.; Kohlbrecher, J.; Patkowski, A.; Holyst, R. *Langmuir* **2010,** 26, (12), 9304-9314.

30. Cotter, M. A.; Martire, D. E. *J. Chem. Phys.* **1970,** 52, (4), 1909-&.

31. Jorgensen, W. L.; Maxwell, D. S.; TiradoRives, J. *J. Am. Chem. Soc.* **1996,** 118, (45), 11225-11236.

32. Jensen, K. P.; Jorgensen, W. L. *J. Chem. Theory Comput.* **2006,** 2, (6), 1499-1509.

33. Hoops, S. C.; Anderson, K. W.; Merz, K. M. *J. Am. Chem. Soc.* **1991,** 113, (22), 8262-8270.

34. Plimpton, S. *J. Comput. Phys.* **1995,** 117, (1), 1-19.

35. Hockney, R.; Eastwood, J., *Computer Simulation Using Particles*. Taylor and Francis: New York, 1989.

36. Waasmaier, D.; Kirfel, A. *Acta Crystallogr. Sect. A* **1995,** 51, 416-431.

Chapter 6

Conclusions and Future Work

6.1 Conclusions

The synthesis of precise acid copolymers and ionomers provides an invaluable opportunity to acquire elusive fundamental knowledge in polymer physics. These materials can be regarded as high molecular weight, linear polyethylene (PE) chains functionalized with polar (acidic or ionic) pendant groups at specific sequences of carbon atoms along the polymer backbones. The structural simplicity of these materials lends exceptional control over the polymer microstructure, allowing scientists to focus on the effect of specific variables on the morphology and properties. Moreover, precise model materials can be simulated for direct comparisons to experimental results and to attain complementary molecular-level information. This dissertation presents the first comprehensive study of the morphologies at room and elevated temperatures for all the precise acid copolymers and ionomers synthesized to date. Among the most interesting aspects of this study is the discovery of new morphologies for acid- and ion-containing polymers with unprecedented long-range order in three dimensions.

In Chapter 2, the morphology of one precise acid copolymer functionalized on every 21st carbon atom with two phosphonic acid groups (p21gPA) is studied at room temperature (20 °C) and 155 °C by X-ray scattering. The scattering profiles at both temperatures feature higher order peaks consistent with face-centered cubic (FCC) packing of aggregates, marking the first report of three-dimensional long range order in

acid copolymers. The calculated FCC lattice parameters (a_{FCC}) are 4.19 nm and 4.06 nm at 20 °C and 155 °C, respectively. Further evidence of FCC packing is obtained from a drawn p21gPA sample that exhibits two FCC crystal orientations with a common <1 1 0> crystallographic direction.

Chapter 3 is a comprehensive study of the elevated temperature ($T > T_g$, T_m) morphologies of precise materials copolymerized with acrylic acid (AA), phosphonic acid (PA) and 1-methylimidazolium bromide (ImBr). At high temperatures, all but one of the AA, PA and ImBr precise copolymers (p21gPA) exhibit a liquid-like arrangement of microphase separated acid-rich or ion-rich. These liquid-like morphologies are ideal for making direct comparisons as a function of carbon sequence length between pendant groups (every 9^{th}, 15^{th} or 21^{st} carbon substitution), size and volume fraction of the pendant species, and functional group configuration (single or geminal). As expected, X-ray scattering shows that the inter-aggregate spacing (d^*) increases with the length of the PE segments and the size of the pendant species. However, a relative distance obtained by dividing d^* by the PE segment lengths in all-t*rans* conformation ($l_{\text{all-}trans}$) reveals additional morphological information that is independent of PE segment length. The relative distance in precise copolymers increases with content of pendant groups (decreasing PE segments and geminal configuration), suggesting growth in the aggregate sizes.

In Chapter 4, the morphologies of the same precise copolymers examined in Chapter 3 are studied at room temperature. In this case, three morphology types are defined based on the arrangement of the microphase-separated acid or ionic aggregates in

the PE matrix. (1) The liquid-like morphology is observed when the PE segments are short enough to inhibit PE crystallinity. This morphology is identified by a single broad aggregate peak in X-ray scattering and an amorphous CH_2 resonance in ^{13}C NMR. (2) The layered morphology occurs in the presence of PE crystals, which form when the segments are longer than 15 carbon-carbon bonds. PE crystallinity is evidenced by a reflection in wide-angle X-ray scattering and by the orthorhombic CH_2 resonance in ^{13}C NMR. The layered arrangement of the aggregates results in several higher order peaks with layered symmetry in X-ray scattering. Upon drawing, the layered materials become anisotropic such that the PE chains and the acid layers orient perpendicular to each other. Two cases are observed: layer orientation parallel (AA and PA) and perpendicular (ImBr) to the stretch direction. This morphology type is exclusively observed in precise acid copolymers and ionomers. (3) The cubic morphology, described in detail in Chapter 2, is the third morphology identified at room temperature. Although the aggregates have three-dimensional long-range order, the PE segments appear to pack defectively, resulting in an intermediate resonance between amorphous and crystalline in ^{13}C NMR. The cubic morphology only occurs when the pendants are geminal PA groups and the PE segments are long and flexible enough to allow aggregate assembly into periodic structures.

In Chapter 5, complementary experimental and simulation methods are used to study the morphologies of precise AA ionomers with metal cations in the melt (120 °C). The simulations predict that the aggregate shapes can vary from compact to stringy to percolated in these systems. The aggregate shape can change as a function of PE segment length, cation type and the level neutralization. In addition, it is shown that hydrogen

bonding and the coordination geometries of the ions in the aggregates have a major influence in the morphology. Through these comparisons with experiments, it was found that the low angle X-ray scattering peak in acid copolymers and ionomers arises from inter- and intra-aggregate interference scattering. In other words, the interaggregate spacing (d^*) measures the distances between distinct aggregates, and between segments of elongated (often branched) aggregates. Furthermore, it is not possible to determine the shape of the aggregates by X-ray scattering alone, as profiles from compact or stringy aggregates are often indistinguishable. Modeling of the scattering profiles by approximating the aggregates as spheres or as cylinders are compared and their pertinence evaluated with the help of real space representations of the simulations.

6.2 Future Work

6.2.1 Morphology of Precise Ionomers as a Function of Neutralization Level: The morphologies of ionomers of polyethylene copolymerized with AA have been studied experimentally as a function of spacer length (carboxylic acid/carboxylate pendants on every 9^{th}, 15^{th} or 21^{st} carbon atom)[1-3] and neutralizing cation (H^+, Li^+, Na^+, Cs^+ and Zn^{2+}).[2,3] Many of these changes produce remarkable effects on the morphology, including instances of the layered and cubic morphologies.[1,2] However, the effect of neutralization level on the morphology has not been examined due to limited sample quantities. Thanks to work carried out by the group of Dr. Joseph Cordaro from Sandia National Laboratories, large quantities of p9AA, p15AA and p21AA have recently become

available. These materials can easily be neutralized with metal cations following known methods.[3]

It is expected that for any neutralizing cation, changes in the level of neutralization will produce surprising evolutions of the aggregate morphologies. In a recent report of atomistic MD simulations of ionomer melts,[4] Cs-neutralized systems progressed with increasing neutralization from "long, stringy" (LS) at 10% Cs, to "partially percolated" at 25% Cs, and to "fully percolated" (FP) at 75% Cs. However, the Zn-neutralized systems went from forming LS aggregates at 10% Zn, to "short, stringy" (SS) at 43% Zn, and to SS/"compact, isolated" (CI) at 100% Zn. Upon examination of the local structure, it was determined that hydrogen bonding is not essential to aggregate propagation in the Cs systems because the large counterions allow many different coordination geometries and diminishes Coulombic repulsion. However, the Zn systems tend to form solely zinc-oxygen motifs due to the highly localized charge of the cations. In this systems, the Zn atoms tend to be well-separated and connected by hydrogen-bonded strands, Figure 6.1.[4,5]

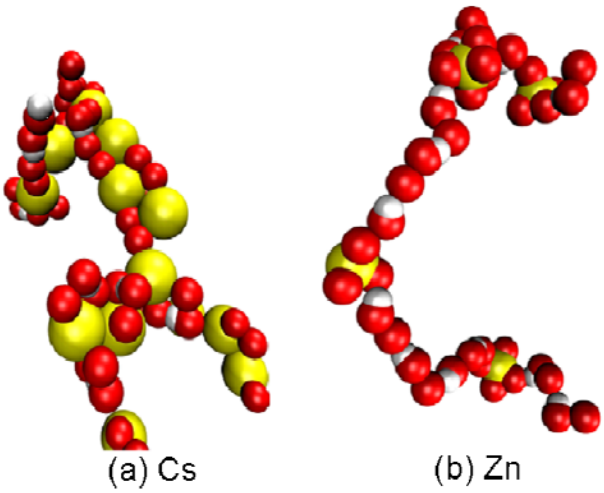

Figure 6.1 Single aggregates from a precise AA copolymer (p9AA) with 43% neutralization with (a) Cs and (b) Zn. Oxygen atoms are shown in red, counterions in yellow, and hydrogen atoms in white. Adapted from reference 4.

Through X-ray scattering and NMR spectroscopy, the ionomer morphologies as a function of neutralization level can be explored at room and elevated temperatures. Sequential changes in the neutralization levels are expected to elucidate the underlying causes for cubic ordering of aggregates. Many variables can be studied independently in a way that has not been possible before. For example, the volume fraction of pendant groups and aggregates can be varied in a controlled way without changing pendant species or configurations. In addition, the role of hydrogen bonding can also be quantified by gradual neutralization of the acid group (carboxylic acid) with increasing level of metal cations. This detailed study of hydrogen bonding and ionic aggregation in the evolution of precise ionomer morphology will benefit from Fourier transform infrared spectroscopy (FTIR) and dielectric relaxation spectroscopy (DRS).

6.2.2 FTIR and DRS of Precise Acid Copolymers and Ionomers: Currently, FTIR and DRS experiments of precise acid copolymers and ionomers are being carried out in collaboration with Prof. James Runt at the Pennsylvania State University. These studies are aimed at extending the morphology examinations provided in this dissertation; therefore, careful sample preparation is essential to match the thermal history of the samples for X-ray scattering, ^{13}C NMR and DSC. In addition, DRS can also provide experimental information about dynamics. The materials under investigation currently include the precise AA copolymers and Li-neutralized ionomers, and the precise ImBr ionomers.

Through FTIR, the local environment of the polar pendant groups can be quantified. A preliminary study of the AA copolymers shows that, although the great majority of carboxylic acid groups participate in hydrogen bonding, there is a small population of isolated acids that increases with higher content of pendants, Figure 6.2. In MD simulations of precise AA ionomers neutralized with Li, the composition of the aggregates has been identified as an essential factor in the shape of the aggregates.[6] FTIR can quantify how the hydrogen bonded acid groups contribute in the evolution of compact aggregates into string-like and into percolated aggregates.

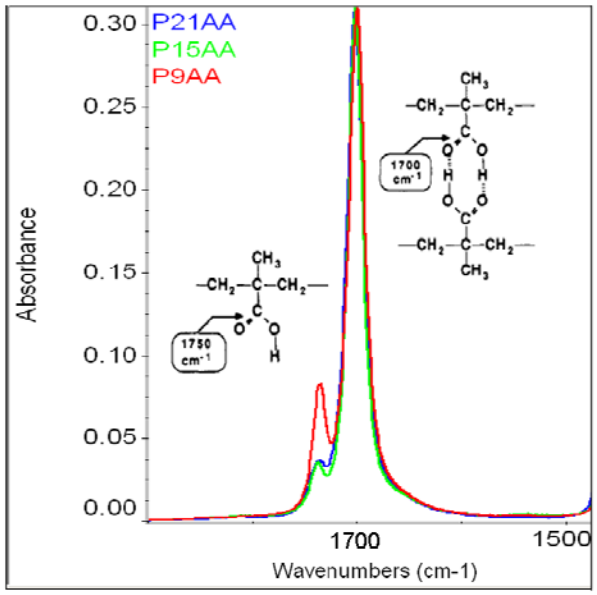

Figure 6.2 FTIR of precise AA copolymers with pendant groups on every 21st (p21AA), 15th (p15AA) and 9th (p9AA) carbon atom. The intense band at 1700 cm^{-1} indicates hydrogen bonded carboxylic acids. The smaller band at 1750 cm^{-1} can quantify the amount of isolated carboxylic acids in the samples. Data courtesy of Hanqing (Elaine) Masser.

Through DRS, the arrangement of the ionic aggregates in semi-crystalline materials can be evaluated. Preliminary data for ImBr samples show relaxations associated to Maxwell – Wagner – Sillar (MWS) interfacial polarization, which are typically observed in multiphase systems with different dielectric constants and conductivities.[6] Variable temperature DRS measurements detected transitions in the MWS relaxations for semicrystalline precise ImBr at temperatures that correspond to the melting of PE crystals (T_m). This observation suggests that below T_m, there is significant ion accumulation in the systems, presumably at the interfaces of the PE crystals. This

explanation is consistent with our description of the layered morphologies in semicrystalline precise ionomers.

The dynamics of precise AA and ImBr materials can also be examined experimentally over wide ranges of frequency and temperature using DRS. The relaxations associated with the amorphous, crystalline and restricted mobility phases are expected to change with pendant content and level of neutralization. In addition, relaxations associated to rearrangement of ionic aggregates can potentially be detected, as reported previously for sulfonated polystyrene ionomers.[7-9] Finally, the conductivity of direct current (σ_{DC}) can also be calculated.

6.2.3 Mechanical Testing of Precise Acid Copolymers and Ionomers: The strong interactions of polar groups in PE-based acid copolymers and ionomers result in remarkable mechanical properties. In this dissertation, their morphologies have been studied through experimental and simulation methods. These morphologies are extremely uniform (lamellar thickness, aggregate separation, etc.) as a consequence of the microstructural precision obtained from ADMET polymerization. This unprecedented morphological uniformity, which is reproducible from sample to sample, provides a perfect opportunity for rigorous structure – property relationships in acid- and ion-containing polymers. In particular, tensile tests are already in progress to probe the elastic modulus and yield stress as a function of carbon atoms between pendants, pendant type, cation type and level of neutralization.

For precise materials with varying lengths of PE segments between pendant groups, preliminary data in Figure 6.3 show spectacular improvements in the elastic

modulus as the PE segment length increases. This result can be explained by the formation of PE crystals for segments longer than 14 carbon-carbon bonds.[2] However, the variation in mechanical properties when the pendant groups are changed from carboxylic to phosphonic acid is yet to be studied. Precise acid copolymers with PA pendants are expected to exhibit much higher modulus and yield stress. These properties seem to be reinforced with geminal pendant functionalizations. Possible clues towards reconciling the pendant group type with mechanical properties are given by examining the morphologies prior and after tensile deformation. For example, p21gAA and p21gPA have geminal functionalizations on every 21st carbon of carboxylic and phosphonic acid, respectively. Anisotropic samples of these materials reveal a layered morphology for p21AA and a cubic morphology for p21gPA. The difference is most likely related to the increased number of hydrogen bonding sites for PA (3) relative to carboxylic acid (2).

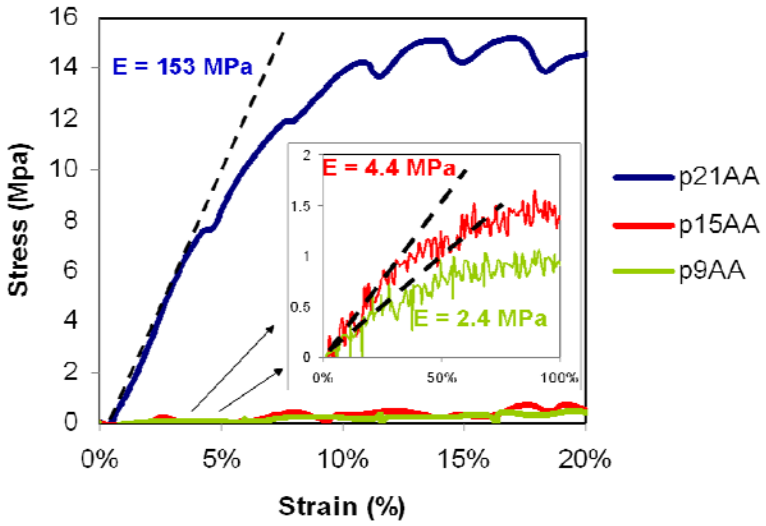

Figure 6.3 Tensile mechanical data for precise AA copolymers functionalized on every 21st (p21AA), 15th (p15AA) and 9th (p9AA) carbon atom. The elastic modulus (E) is indicated for each species. Data courtesy of L. Robert Middleton.

The evolution of both the morphology and mechanical properties will be examined closely using *in situ* X-ray scattering and tensile deformation. This work has already started at the Advanced Photon Source at Argonne National Laboratories. Through real time coupling of deformation and scattering, changes in crystal size, orientation, and unit cell orientation are being correlated to features observed in the stress-strain curves. In addition, structural changes during stress relaxation are also being monitored. Synchrotron radiation provides rapid data collection, such that intermediate and transient morphologies are captured.

6.2.4 Morphology and Properties of Precise Copolymers with Sulfonic Acid Pendants: A major motivation for the development of precise acid copolymers and

ionomers is the rational design of solid polymer electrolytes for batteries and fuel cells. One of the main microstructural details that can be fine-tuned in precise copolymers to optimize the desired properties is the pendant type. In fact, the precise acid copolymers developed by Wagener and co-workers have been targeted to study the effect of acid strength on the morphology and properties.[1,10] The pendant groups studied in this dissertation are relatively weak acids, with pKa = 5 for carboxylic acid and pKa = 2 for PA. Another weak acidic pendant that is planned is boronic acid, with a pKa = 9. However, the most attractive pendant group from the point of view of the properties is sulfonic acid, a strong acid with pKa = -2. The strength of sulfonic acid is one of the biggest factors in the success of Nafion as a proton conducting membrane in PEM fuel cells.

Wagener's group is currently taking the final steps on the synthesis of precise sulfonic acid copolymers functionalized on every 9^{th}, 15^{th}, and 21^{st} carbon via ADMET. This level of precision has never been attained in sulfonic acid copolymers, and it is expected to help elucidate the mechanism of ion conduction in Nafion, a highly-branched polymer with randomly placed acidic pendants. In addition, previous work with the AA and PA copolymers indicates highly organized morphologies that, if also present in the sulfonic acid precise copolymers, would have interesting implications for the properties. Similarly, data from property measurements such as ionic conductivity or polymer dynamics are also expected to be well-defined and easy to interpret. Anisotropic morphologies such as the layered structure, which is expected to form in the sulfonic acid

precise copolymers with long PE spacers, could be oriented to align the acid-rich layers to promote ion transport.

An integral part of the research of the precise sulfonic acid copolymers is atomistic MD simulations, for which the force fields have already been developed in the groups of Drs. Amalie Frischknecht and Mark Stevens from Sandia National Laboratories. The simulations will not only provide information about the morphology (shape and arrangement of the aggregates), but about the molecular processes involved in ion transport. It is believed that Nafion uses water in a vehicle mechanism to transport protons.[11] However, previous work with AA copolymers and ionomers in the melt (in the absence water) detects ionic diffusion in these materials through a process of aggregates coalescing, exchanging ions and breaking. On the other hand, "ion-hopping" of isolated ions from one aggregate to another through the non-polar matrix was not observed. It will be very interesting to study the potential of dry sulfonic acid membranes, which will extend their operational temperature above 100 °C. It is probable that the sulfonic acid materials have higher proton diffusion than the AA ionomers due to the strong acidity of sulfonic acid.

6.3 References

1. Baughman, T. W.; Chan, C. D.; Winey, K. I.; Wagener, K. B. *Macromolecules* **2007,** 40, (18), 6564-6571.

2. Seitz, M. E.; Chan, C. D.; Opper, K. L.; Baughman, T. W.; Wagener, K. B.; Winey, K. I. *J. Am. Chem. Soc.* **2010,** 132, (23), 8165-8174.

3. Buitrago, C. F.; Bolintineanu, D. S.; Seitz, M. E.; Stevens, M. J.; Frischknecht, A. L.; Winey, K. I. *In Preparation*.

4. Bolintineanu, D. S.; Stevens, M. J.; Frischknecht, A. L. *Macromolecules* **2013**, DOI: 10.1021/ma400848m.

5. Bolintineanu, D. S.; Stevens, M. J.; Frischknecht, A. L. *ACS Macro Lett.* **2013,** 2, (3), 206-210.

6. Atorngitjawat, P.; Runt, J. *Macromolecules* **2007,** 40, (4), 991-996.

7. Castagna, A. M.; Wang, W.; Winey, K. I.; Runt, J. *Macromolecules* **2010,** 43, 10498-10504.

8. Castagna, A. M.; Wang, W.; Winey, K. I.; Runt, J. *in preparation Macromolecules* **2010**.

9. Castagna, A. M.; Wang, W.; Winey, K. I.; Runt, J. *Macromolecules* **2011,** 44, (8), 2791-2798.

10. Opper, K. L.; Markova, D.; Klapper, M.; Mullen, K.; Wagener, K. B. *Macromolecules* **2010,** 43, (8), 3690-3698.

11. Schuster, M.; Rager, T.; Noda, A.; Kreuer, K. D.; Maier, J. *Fuel Cells* **2004,** 5, (3), 355-365.

Appendix A

Dynamic Mechanical Analysis and Rheology of Precise Ionomers Containing 1-Methylimidazolium Bromide

The literature is full of dynamic mechanical investigations of materials with no structural control, giving rise to incomplete and sometimes contradictory conclusions about the effect of physical cross-links on viscoelasticity.[1] One of the most fundamentally important characteristics of the ADMET materials is the homogeneous molecular weight between associating groups in the polymers, which is the variable that controls the chain relaxation time. Here, precise ionomers with 1-methylimidazolium pendants were characterized by dynamic mechanical analysis (DMA) in an effort to understand the impact of regioregularity and spacer length on the matrix and ionic aggregate glass transitions. In addition, the viscoelastic response of the same materials was examined via melt rheology a function of temperature and frequency, producing time-temperature superposition curves.

DMA thermographs of melt-pressed p9ImBr, p15ImBe, p21ImBr, r21ImBr and linear PE synthesized via ADMET are shown in Figure A.1. The DMA data were acquired with a Rheometrics Solids Analyzer (RSAII) at a frequency of 0.16 Hz and a maximum strain set to 3% under a nitrogen purge. A static load of 100 gmf was applied initially and was then adjusted to 125% of each measured dynamic load. This adjusted load was necessary to prevent sample buckling. Mechanical data were collected starting at -50.0 °C and every 20 s thereafter, while the temperature increased at a rate of 3.0

°C/min. Each sample film was pressed from a mold at ~10 °C higher than its maximum thermal transition reported by DSC.[2] The film dimensions were approximately 53 mm long, 6mm wide, and 0.3 mm thick; exact dimensions for each sample deviated slightly but were accurately measured and used in DMA calculations.

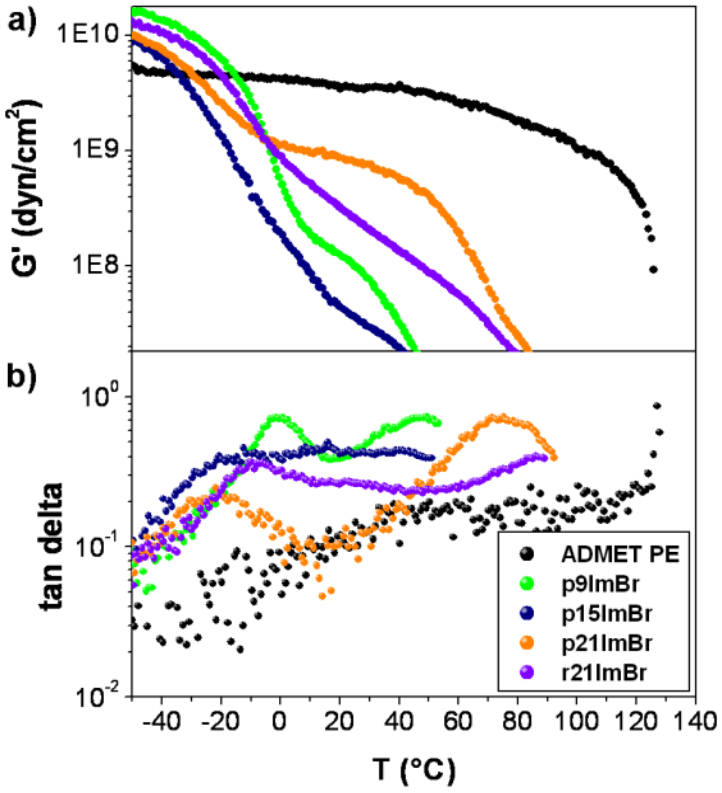

Figure A.1. (a) Storage modulus (G') as a function of temperature for linear polyethylene with various levels of imidazolium bromide substitutions. (b) tanδ as a function of temperature for the same materials.

All the precise imidazolium based ionomers exhibit a sharp decrease in storage modulus (G') by 0 °C. This transition is associated to the onset of chain mobility in the

amorphous region, and is accompanied by a peak in tanδ. The absence of this response in the DMA of linear PE is related to its high degree of crystallinity. Semicrystalline p21ImBr exhibits an intermediate plateau attributed to the presence of small crystallites and small aggregates acting as physical crosslinks. Although compositionally identical, r21ImBr and p21ImBr have very different behaviors in this rubbery regime. P9ImBr and p15ImBr have higher volume fractions of ImBr groups, which should increase the number of aggregates and crosslinks. Ironically, ImBr groups not only give rise to higher crosslink density but also to higher free volume due to the bulkiness of the imidazolium groups, resulting in a greater decrease in modulus. All the ImBr polymers have second tanδ peaks, all varying in position and area. These peaks most likely indicate chain relaxation in phase separated aggregates.

For melt rheology, the samples were hot-pressed in molds of 15mm x 7mm x 0.4mm. Hot-pressing temperatures were ~ 15 ˚C above the highest thermal transition for 30 minutes and 1 metric ton. Rheological measurements were carried out with a RSAII in shear sandwich geometry. Samples were tested under liquid nitrogen for rapid cooling and to prevent the degradation of the precise ionomers. Each run was carried out in a temperature range between 80˚C and 200˚C, well above the highest thermal transition (Tg or Tm) and below their decomposition temperatures.[2] Frequency (ω) was set out from 100 to 0.1 rad/s. To relate the time and temperature dependence of the viscoelastic properties of the materials, time-temperature superposition curves were made using a reference temperature of 140° C and shifting the logarithmic frequency axis by a value called the shift factor (a_T).

In Figure A.2, the storage moduli of all imidazolium bromide ionomers follow typical polymer behavior as a function of frequency. Namely, it increases with the frequency. This means that at higher frequencies the material behaves more like an elastic solid than a viscous liquid. This trend can be attributed to the time needed for the polymer chain to relax under an applied stress. For instance, at slow strain frequencies the polymers initially resist the applied stress, but due to chain motion similar to liquid flow, the materials deform and reduce the stress. At higher frequencies, the polymers do not have enough time to move and therefore resist the stress in an elastic manner. Using a reference frequency of 10 rad/s we can see that the magnitude of G' is different for most of the precise ionomers. This trend indicates that the different concentrations of ImBr ionomers have varying effects on the dynamic mechanical properties. The materials with low ImBr concentrations (r21ImBr and p21Imbr) have more solid like behavior than the materials with higher ImBr concentrations. This can be attributed to better cohesion between the polymer chains resulting in less free volume in the bulk material. On the other hand, a higher concentration of large ImBr groups creates a lot of free volume in the material which results in a softer material with liquid like behavior. An interesting phenomenon is observed by comparing p9Imbr and p15ImBr. Although the p9ImBr material has higher ion concentration its G' is higher than p15ImBr. This discrepancy with the previous explanation can be attributed to a high degree of ionic interaction between the ImBr groups making the material more solid like.

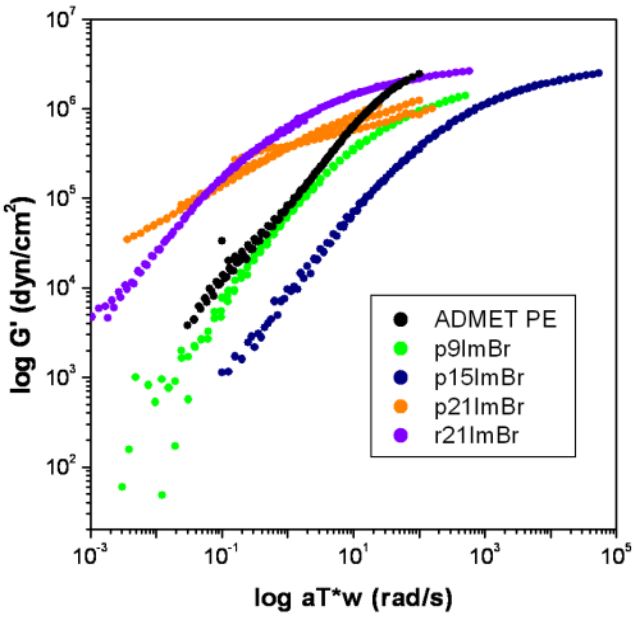

Figure A.2. Master Curve of the storage modulus (G') for precise imidazolium bromide ionomers.

Conclusion

The dynamic mechanical properties of precise imidazolium bromide-based copolymers were inspected using DMA and melt rheology. This is the first time that any properties of precise ionomers have been examined. DMA found clear evidence of microphase separation as indicated by two instances of chain relaxation in temperature ranges between -50 °C and 130 °C. The semicrystalline ionomers (p21ImBr and r21ImBr) experienced gradual transitions from glassy to rubbery phases due to the melting of crystallites. In p21ImBr, this transition is characterized by a plateau that suggests that all the crystals melt at the same temperature, when the curve decreases rapidly. On the other hand, the pseudo-random version of this material, r21ImBr,

experiences a transition in the form of a shallow slope due to irregular crystals melting at different temperatures. In most of the cases examined in this study, the viscoelastic properties of ionomers with imidazolium bromide groups were improved relative to linear PE. Whereas at high frequencies all materials have comparable moduli, the semicrystalline materials experienced an increase in the modulus at low frequencies indicating the effective role of ionic groups as physical crosslinks. On the other hand, the amorphous ionomers have a lower modulus compared to PE, hypothetically due to their greater content of ImBr groups creating extra free volume.

References

(1) Eisenberg, A.; Kim, J.-S., *Introduction to Ionomers*. 1st ed. ed.; Wiley: New York, 1998.

(2) Aitken, B. S.; Buitrago, C. F.; Heffley, J. D.; Lee, M.; Gibson, H. W.; Winey, K. I.; Wagener, K. B. *Macromolecules,* **2012,** *45*, 681-687.

Appendix B

Additional Information for Chapter 3

This appendix contains variable temperature X-ray scattering for p15ImBr and r21gPA, and ^{31}P MAS NMR results for precise and pseudo-random copolymers containing phosphonic acid groups.

X-ray scattering data in Figure B.1 show that neither the aggregate peak intensity, shape nor position vary appreciably for of ImBr and PA copolymers above their thermal transition up to 180 °C. Therefore, it is sufficient to explain the morphology and d* trends for the 12 copolymers in this study at one elevated temperature.

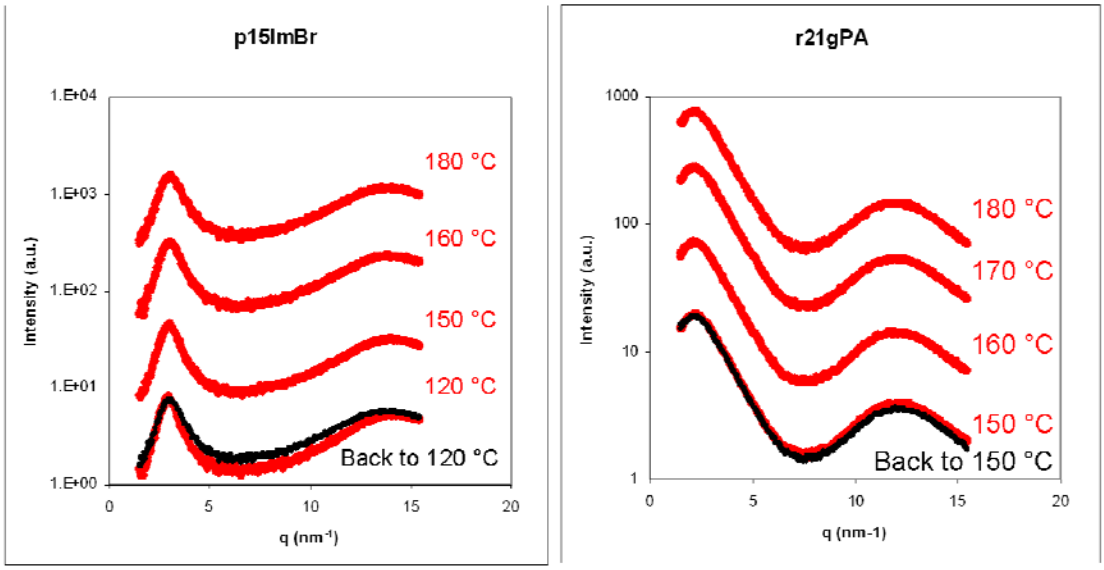

Figure B.1 Multiple temperature X-ray scattering for p15ImBr and r21gPA well above their highest transition temperatures.

As discussed in the main body of Chapter 3, the chemical shift at room temperature is ~ 36 ppm for mono-substituted copolymers (p9PA, p15PA, p21PA and r21PA) and ~ 28 ppm for geminal-substituted copolymers (p15gPA and p21gPA). The NMR resonances narrow upon heating and are fully reversible upon cooling, thereby demonstrating the absence of anhydride formation.

*S*olid state magic angle spinning (MAS) ^{31}P NMR spectra were obtained on an Avance-III Bruker 600 instrument (14.1 T), operating at an observed frequency of 242.9 MHz. A 4-mm broadband MAS probe, spinning at 10 kHz, using a single pulse Bloch decay sequence with high power ^{1}H decoupling was used for all samples. Typical experimental conditions included a 60-s recycle delay, 64-scan averages, a 96-kHz spectral width and a 4-μs $\pi/2$ excitation pulse. The ^{31}P chemical shift was referenced to the secondary standard $NH_4H_2PO_3$ at δ = +0.8 ppm with respect to neat phosphoric acid δ = 0 ppm. The variable temperature ^{31}P MAS NMR spectra were obtained on an Avance-I Bruker 400 instrument (9.6 T) at 162.0 MHz with a 4-mm probe and a 6-kHz spinning speed. The samples were ramped from 25 ^{o}C (room temperature) to 120 ^{o}C in 5 ^{o}C increments with a 300-s equilibrium time at each step. Higher sample temperatures and stable spinning speeds were not accessible with current hardware.

The local environment of the PA pendants in the different PA copolymers was also probed using ^{31}P MAS NMR. The ^{31}P MAS NMR spectra are shown in Figure B.2 and reveal only a PA single environment. For p9PA, p15PA, p21PA and r21PA this resonance occurred at δ = ~ +36 ppm, consistent with δ = + 33 reported for PA in poly(vinylphosphonic acid) (PVPA),[1] δ = +35 to +38 ppm in solution for PVPA,[2] and

+33 ppm[3] and +34.8 ppm[4] for PA polymers in solution. In contrast, p15gPA and p21gPA exhibit a single resonance at δ = +28 ppm that was assigned to the geminal PA environment.

Conversion of PA groups into anhydrides has been reported in some materials,[1,3] with a new resonance appearing at δ ~ + 25 ppm. To explore this possibility, variable temperature ^{31}P MAS NMR was monitored during a thermal cycle between 25 ^{o}C and 120 ^{o}C for select polymers: p21PA, p21gPA, r21PA. The observed NMR line width decreases rapidly with increasing temperature until ~80 ^{o}C due to polymer melting, followed by a more gradual decrease in line width up to 120 ^{o}C. The variation of the line width as a function of temperature is shown in Figures B.3, B.4 and B.5. This narrowing can also be seen by comparing the 25 ^{o}C and 120 ^{o}C MAS spectra (Figure B.6) and cooling these polymers back to room temperature results in approximately the same line shape observed prior to the thermal cycle. For p21gPA there is a slight increase in the line width, demonstrating some increase in disorder with this additional thermal treatment. Only a single ^{31}P resonance is observed for these materials during the entire thermal cycle, and there is no change in the chemical shift following this heating. These results confirm that these polymers (p21PA, p21gPA, r21PA) contain either PA or geminal PA pendants, and more importantly, that the thermal treatment employed does not result in the formation of anhydrides.

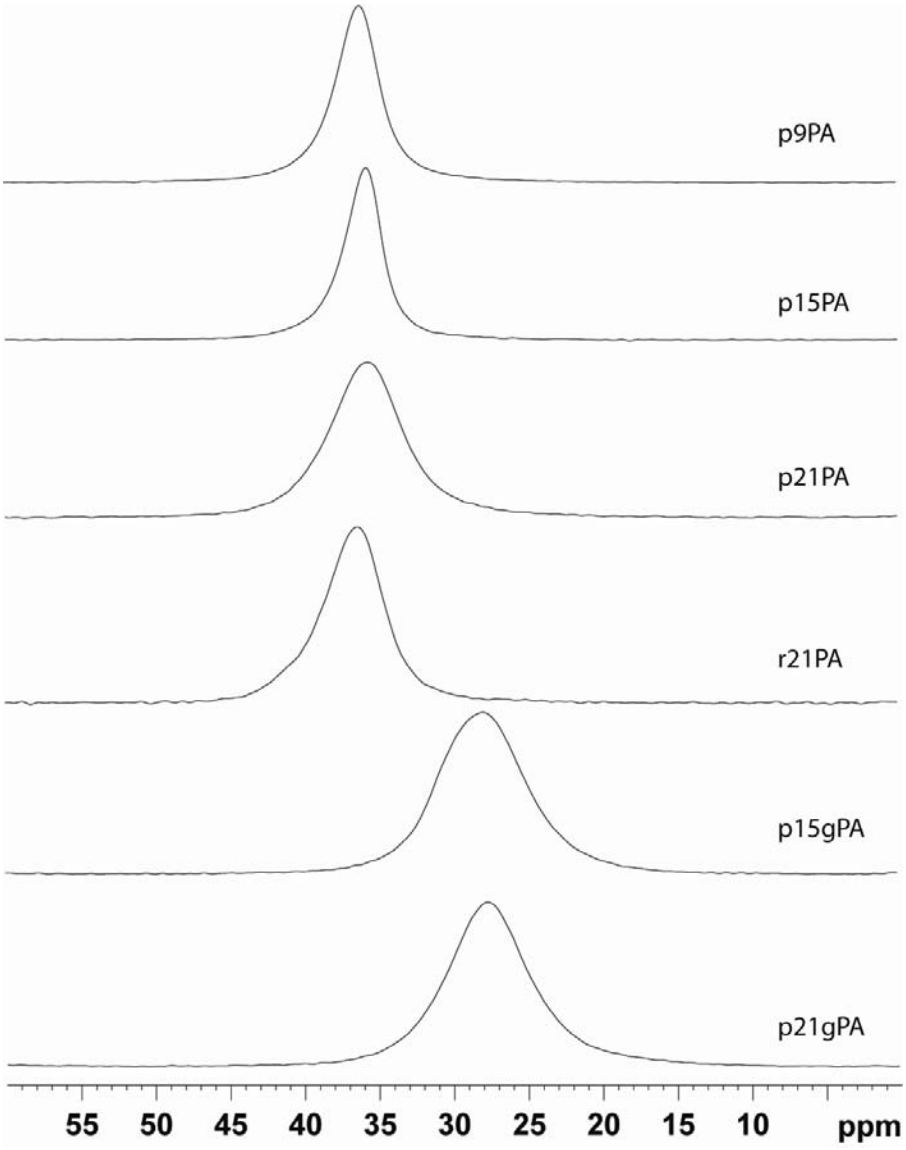

Figure B.2 ^{31}P MAS NMR of the different precise and pseudo random PA polymers at room temperature.

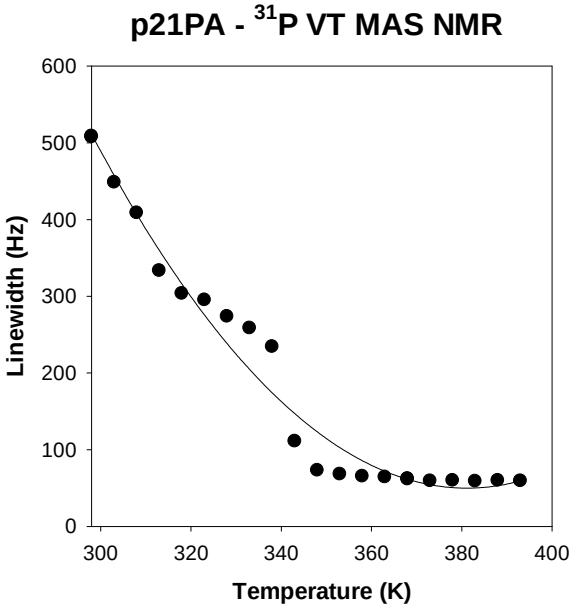

Figure B.3 The variable temperature ^{31}P MAS NMR line width for the p21PA copolymer. The line is for a visual guide only.

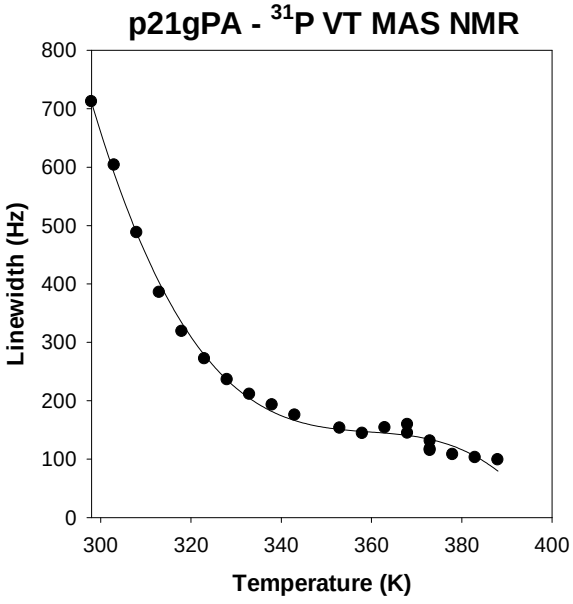

Figure B.4 The variable temperature ^{31}P MAS NMR line width for the p21PA copolymer. The line is for a visual guide only.

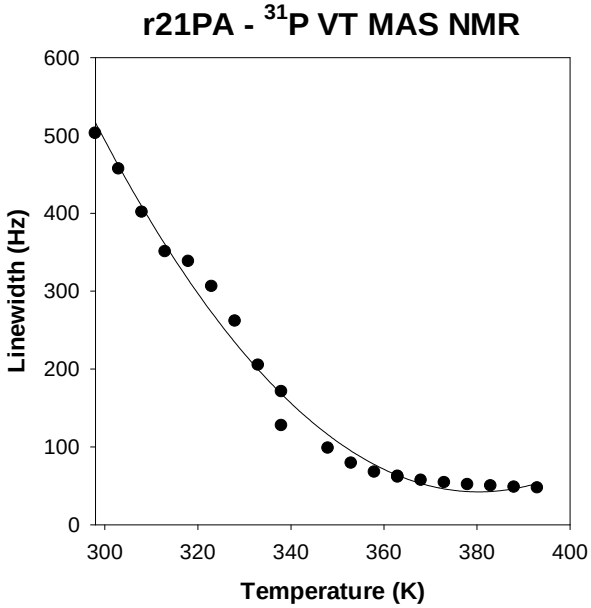

Figure B.5 The variable temperature ^{31}P MAS NMR line width for the r21PA copolymer. The line is for a visual guide only.

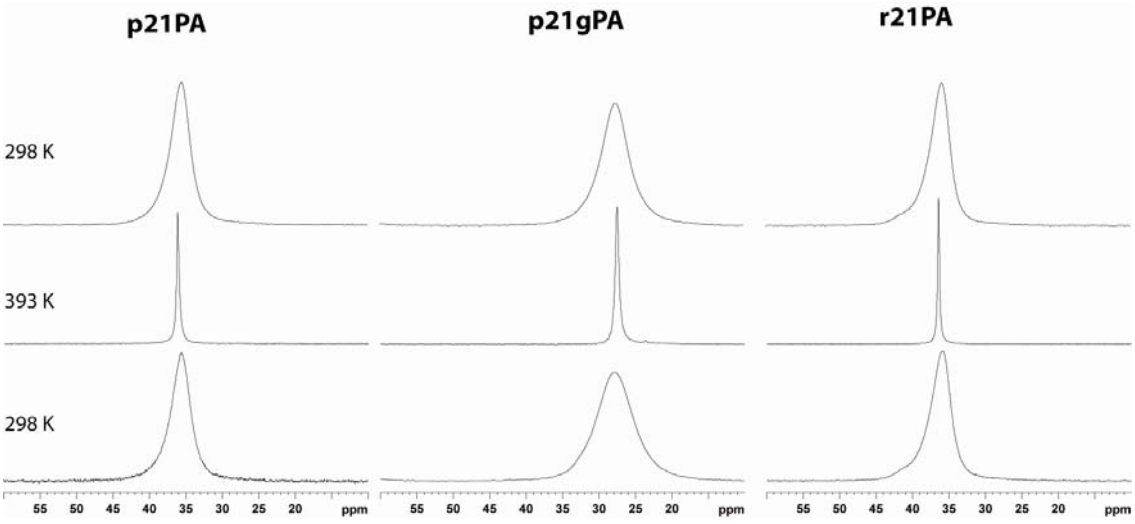

Figure B.6 Variable temperature ^{31}P MAS NMR spectra of PA copolymers before heating (top), at an elevated temperature (middle, 120 ^{o}C) and upon returning to room temperature (bottom).

References

1. Kaltbeitzel, A.; Schauff, S.; Steininger, H.; Bingol, B.; Brunklaus, G.; Meyer, W. H.; Spiess, H. W. *Solid State Ion.* **2007,** 178, (7-10), 469-474.

2. Komber, H.; Steinert, V.; Voit, B. *Macromolecules* **2008,** 41, 2119-2125.

3. Lee, Y. J.; Bingol, B.; Murakhtina, T.; Sebastiani, D.; Meyer, W. H.; Wegner, G.; Spiess, H. W. *J. Phys. Chem. B* **2007,** 111, (33), 9711-9721.

4. Opper, K. L.; Fassbender, B.; Brunklaus, G.; Spiess, H. W.; Wagener, K. B. *Macromolecules* **2009,** 42, (13), 4407-4409.

Appendix C

Additional Information for Chapter 4

This appendix contains X-ray scattering, ^{13}C NMR and DSC data that reinforce some of the conclusions in Chapter 4. Figure C.1 proves that, after sufficient annealing, p15AA copolymers and ionomers display a small DSC endotherm (notice the small range in y-axis) despite lack of any sign of crystallinity in X-ray scattering.

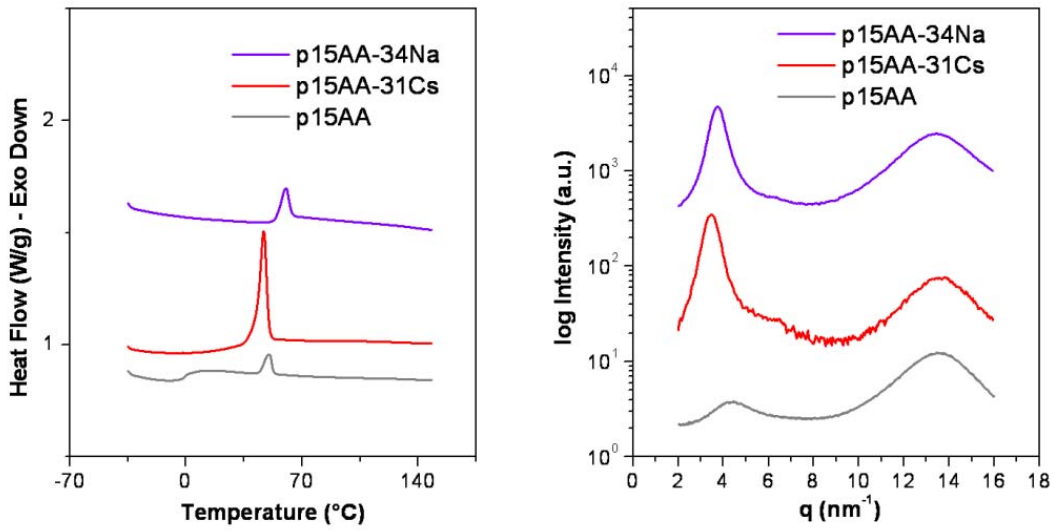

Figure C.1 DSC (left) and X-ray scattering (right) of p15AA acid copolymers and partially neutralized ionomers with 34% Na (violet line) and 31% Cs (red line).

Each one of the high order peaks for stretched p21PA is integrated azimuthally and are shown in Figure C.2. The peaks with 1:2:3 symmetry have maxima at 0° and 180°. However, the 3.36 nm^{-1} peak gains intensity at azimuthal angles of 0, 65, 117, 180,

251 and 296°. Close inspection of the anisotropic 2D scattering pattern in Figure 4.7c reveals that the small peaks at 0 and 180° are inevitable traces from the much stronger signals at q = 2.58 nm^{-1}. In addition, since no rigorous measure of the degree of crystal orientation was made in the stretched samples, it is expected that ill-aligned crystals may give rise to layered aggregates at acute angles with respect to the stretch direction. That is clearly the case for the peaks at azimuthal angles of 65, 117, 251, and 296°, since Figure 4.7c shows that the additional scattering bleeds off from the main lamellar peak parallel to the stretching direction into those angles. With that said, the intensity vs. azimuthal angle pattern at q = 3.36 nm^{-1} in Figure C.2 suggests that this peak remains isotropic in the presence of oriented crystals.

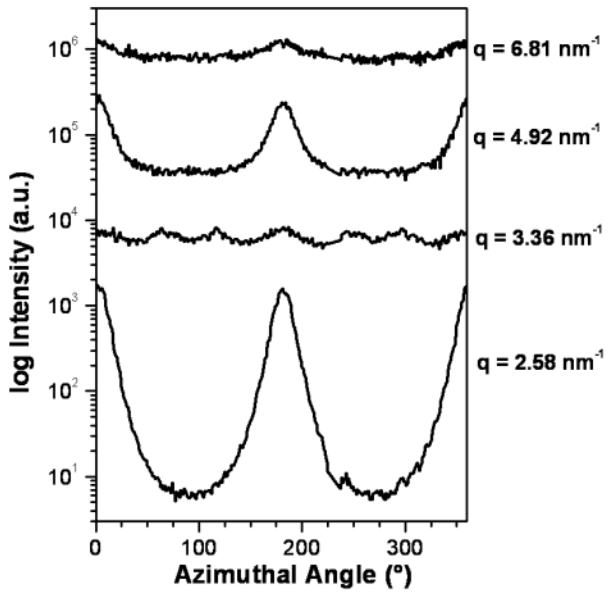

Figure C.2 X-ray scattering intensity as a function of azimuthal angle extracted from the anisotropic pattern of p21PA in Figure 4.7c. The specified q values correspond to the maxima of the intensity vs. q patterns observed in Figure 4.8.

The crystalline and amorphous components in the layered and cubic materials are highlighted utilizing ^{13}C CP MAS NMR experiments with additional spectral filters applied (Figure C.3). The amorphous components are highlighted in green utilizing ^{13}C CP MAS NMR with a dipolar filter applied. These experiments suppress a portion of the crystalline component and enhance the amorphous resonances. The ^{13}C CP MAS NMR with ^{1}H spin-lock (data in red) was utilized to suppress the amorphous components and enhance the crystalline components. The chemical shifts and line-widths for the crystalline and amorphous components were extracted from these filtered experiments and utilized as constraints to fit the ^{13}C quantitative data.

The filtering experiments for the cubic materials exhibit a poor signal-to-noise ratio for p15gPA due to the small sample size (Figure C.4, top). However no distinct enhancement is observed in either the spin-lock or dipolar filter experiments. The dipolar-filter and ^{1}H spin-lock experiments exhibit no noticeable difference from the ^{13}C CP NMR MAS data for p21gPA indicating the presence of an intermediate phase with dynamics on the NMR timescale (Figure C.4). The experimental details of the spin-lock and dipolar filter experiments are provided in Jenkins et at.[1]

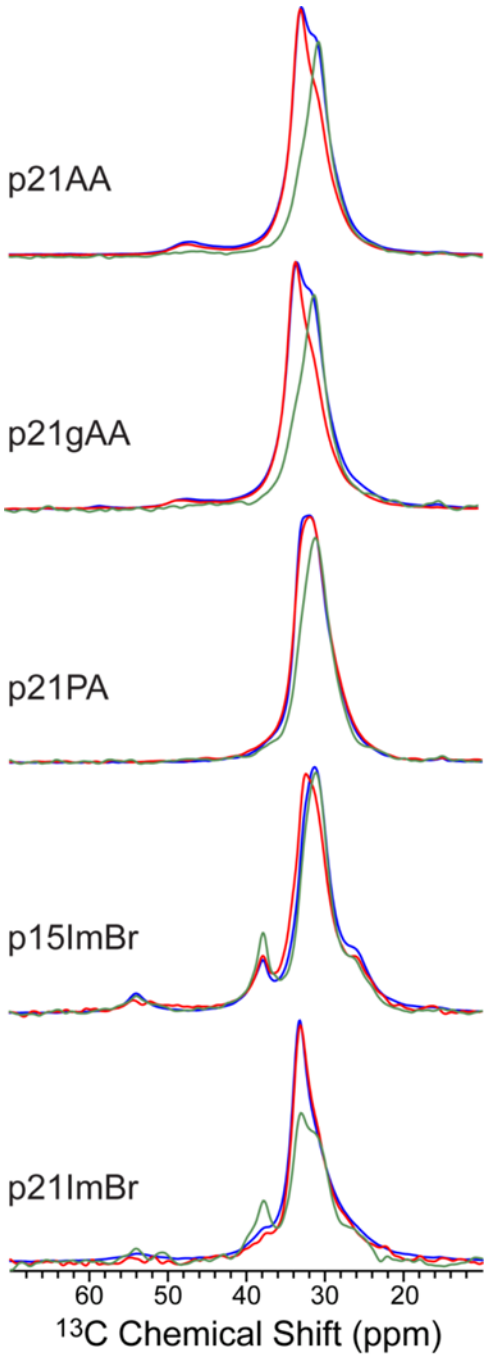

Figure C.3 ^{13}C CP NMR MAS data (blue) overlaid with ^{13}C CP NMR MAS data with dipolar-filter (green) and ^{1}H spin-lock (red) data for precise copolymers that exhibit layered morphologies at room temperature. These copolymers are semi-crystalline.

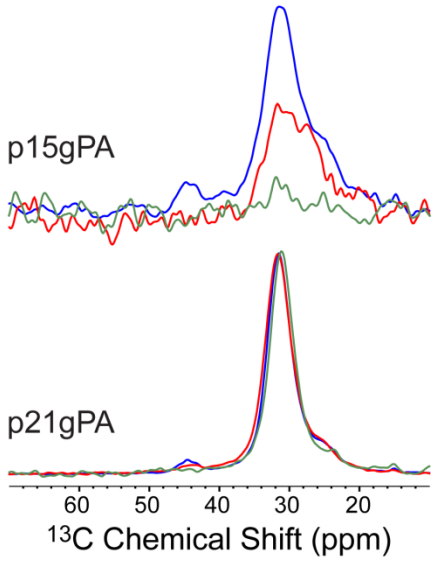

Figure C.4 ^{13}C CP NMR MAS data (blue) of the "cubic materials" with overlay of ^{13}C CP NMR MAS data with dipolar-filter (green) and ^{1}H spin-lock (red).

References

1. Jenkins, J. E.; Seitz, M. E.; Buitrago, C. F.; Winey, K. I.; Opper, K. L.; Baughman, T. W.; Wagener, K. B.; Alam, T. M. *Polymer* **2012,** 53, 3917-3927.

Appendix D

Additional Information for Chapter 5

Atomistic MD simulations and X-ray scattering of 3 precise acid copolymers and 8 precise ionomers are presented in this appendix. Each figure contains real-space snap shots from the simulations, and I vs. q data from the simulations and the X-ray scattering experiments. Furthermore, the I vs. q data was fit with models that approximate the ionic aggregates as cylinders (the modified hard-cylinder model, MHC) or spheres (the modified hard-sphere model, MHS).

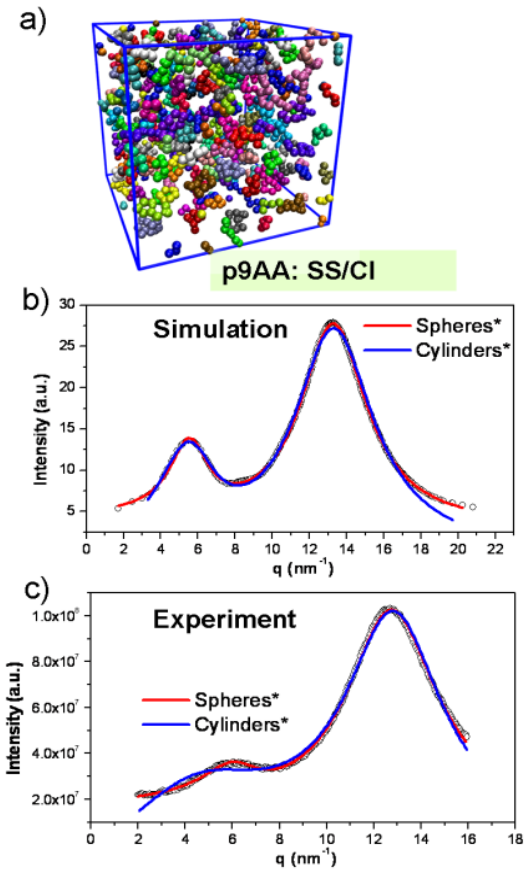

Figure D.1 (a) Real-space morphology of p9AA. (b) Simulated and (b) experimental I(q) profiles fit with the MHS and MHC models. Amorphous halo fit with *one or **two Lorentzians.

Table D.1 Analytical Fits to I(q) from X-ray Scattering and MD Simulations for p9AA

	MHC		MHS	
	Exp.	Sim.	Exp.	Sim.
R (nm)	0.05	0.28	0.40	0.38
Rca (nm)	0.38	0.42	0.49	0.55
L (nm)	1.0	2.83		
n (nm^{-3})	4.23	0.21	0.59	0.46

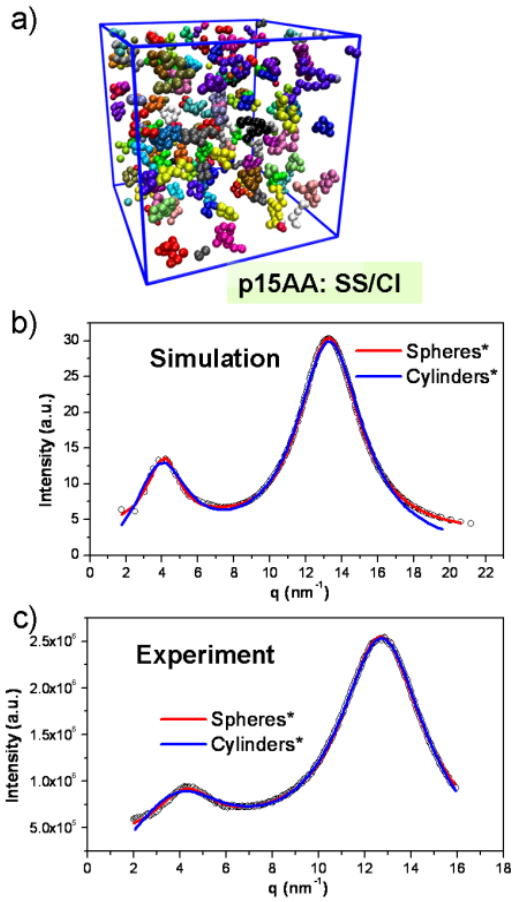

Figure D.2 (a) Real-space morphology of p15AA. (b) Simulated and (b) experimental I(q) profiles fit with the MHS and MHC models. Amorphous halo fit with *one or **two Lorentzians.

Table D.2 Analytical Fits to I(q) from X-ray Scattering and MD Simulations for p15AA

	MHC		MHS		Real space
	Exp.	Sim.	Exp.	Sim.	
R (nm)	0.13	0.27	0.33	0.42	0.33
Rca (nm)	0.50	0.55	0.66	0.73	0.53
L (nm)	2.34	5.23			
n (nm^{-3})	0.11	0.06	0.16	0.17	0.33

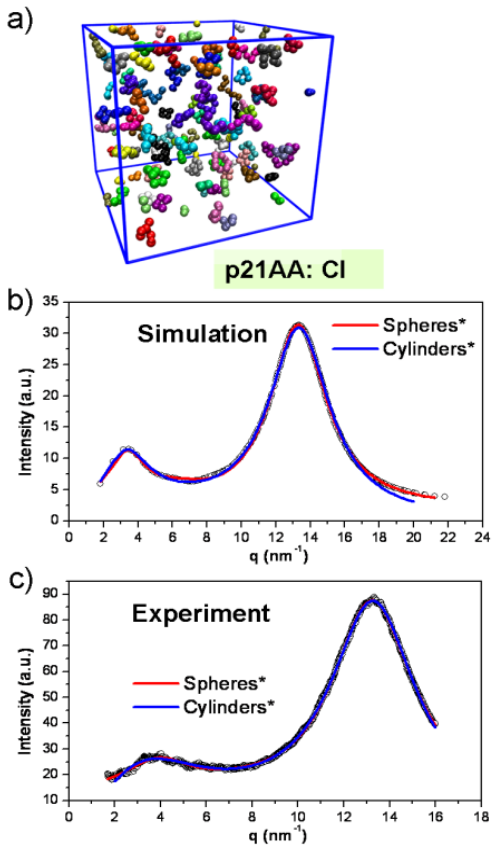

Figure D.3 (a) Real-space morphology of p21AA. (b) Simulated and (b) experimental I(q) profiles fit with the MHS and MHC models. Amorphous halo fit with *one or **two Lorentzians.

Table D.3 Analytical Fits to I(q) from X-ray Scattering and MD Simulations for p21AA

	MHC		MHS		Real space
	Exp.	Sim.	Exp.	Sim.	
R (nm)	0.05	0.21	0.32	0.38	0.32
Rca (nm)	0.48	0.64	0.70	0.85	0.56
L (nm)	4.97	3.14			
n (nm^{-3})	0.06	0.05	0.10	0.08	0.25

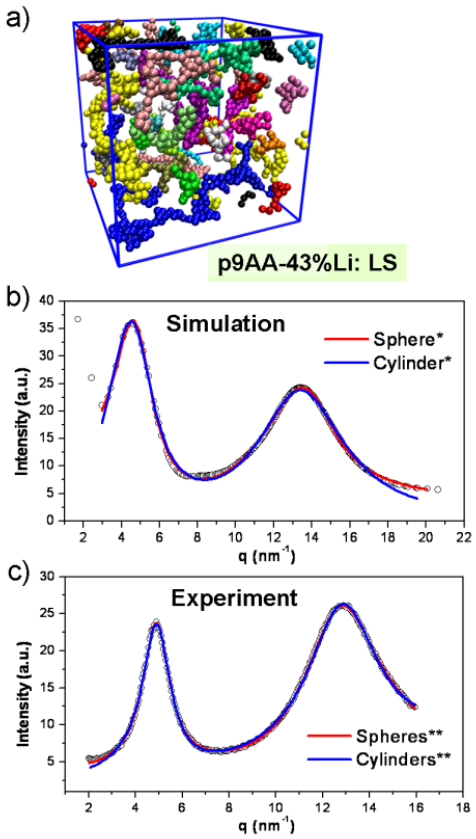

Figure D.4 (a) Real-space morphology of p9AA-43%Li. (b) Simulated and (b) experimental I(q) profiles fit with the MHS and MHC models. Amorphous halo fit with *one or **two Lorentzians.

Table D.4 Analytical Fits to I(q) from X-ray Scattering and MD Simulations for p15AA-45%Li

	MHC		MHS	
	Exp.**	Sim.*	Exp.**	Sim.*
R (nm)	0.37	0.34	0.45	0.47
Rca (nm)	0.51	0.51	0.66	0.63
L (nm)	4.94	3.24		
n (nm^{-3})	0.11	0.12	0.33	0.27

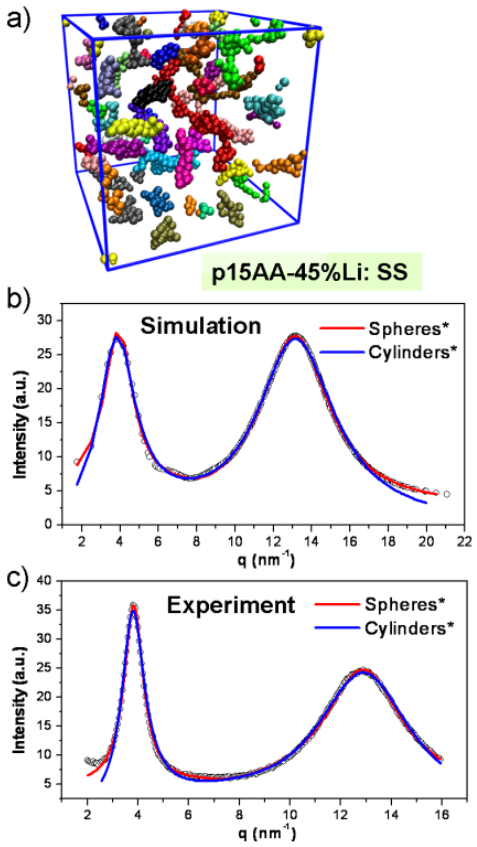

Figure D.5 (a) Real-space morphology of p15AA-45%Li. (b) Simulated and (b) experimental I(q) profiles fit with the MHS and MHC models. Amorphous halo fit with *one or **two Lorentzians.

Table D.5 Analytical Fits to I(q) from X-ray Scattering and MD Simulations for p15AA-45%Li

	MHC		MHS	
	Exp.*	Sim.*	Exp.*	Sim.*
R (nm)	0.23	0.31	0.57	0.48
Rca (nm)	0.67	0.62	0.87	0.77
L (nm)	7.4	5.30		
n (nm^{-3})	0.04	0.06	0.16	0.16

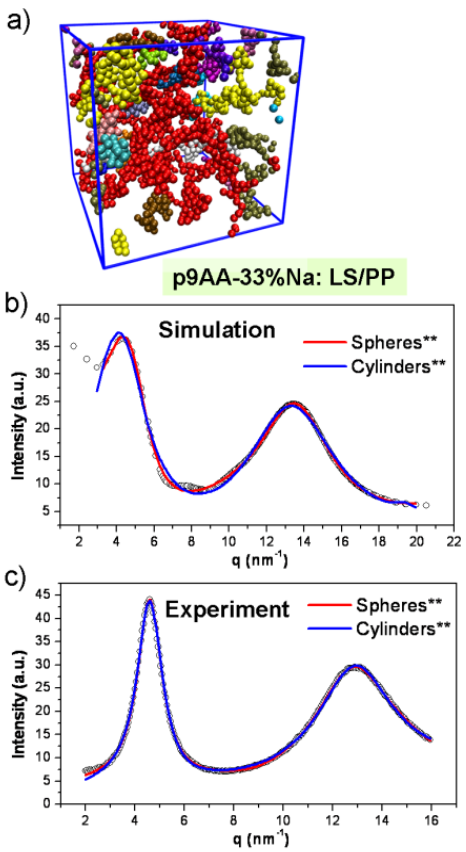

Figure D.6 (a) Real-space morphology of p9AA-33%Na. (b) Simulated and (b) experimental I(q) profiles fit with the MHS and MHC models. Amorphous halo fit with *one or **two Lorentzians.

Table D.6 Analytical Fits to I(q) from X-ray Scattering and MD Simulations for p9AA-33%Na

	MHC		MHS	
	Exp.**	Sim.**	Exp.**	Sim.**
R (nm)	0.37	0.34	0.48	0.55
Rca (nm)	0.55	0.52	0.71	0.60
L (nm)	5.28	3.43		
n (nm^{-3})	0.09	0.10	0.27	0.29

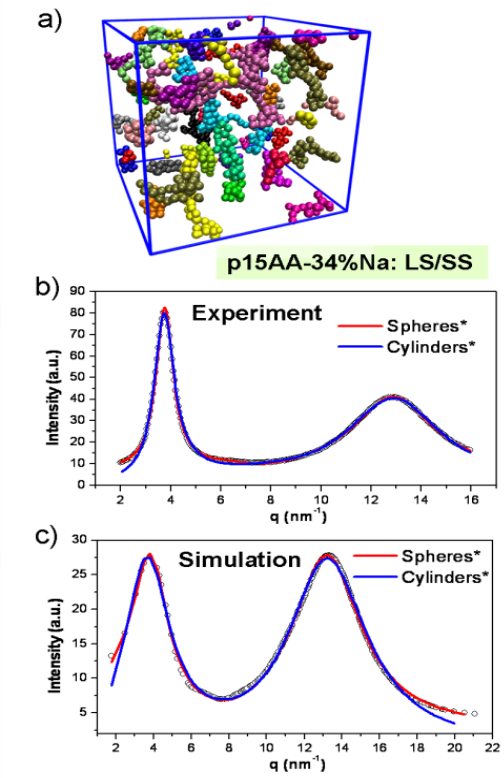

Figure D.7 (a) Real-space morphology of p15AA-34%Na. (b) Simulated and (b) experimental I(q) profiles fit with the MHS and MHC models. Amorphous halo fit with *one or **two Lorentzians.

Table D.7 Analytical Fits to I(q) from X-ray Scattering and MD Simulations for p15AA-34%Na

	MHC		MHS	
	Exp.*	Sim.*	Exp.*	Sim.*
R (nm)	0.25	0.33	0.55	0.49
Rca (nm)	0.68	0.61	0.90	0.75
L (nm)	4.30	5.54		
n (nm^{-3})	0.06	0.05	0.15	0.14

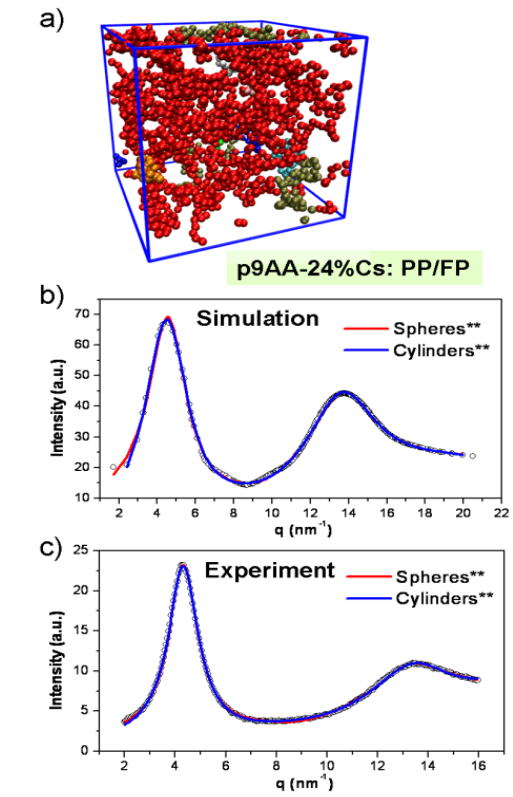

Figure D.8 (a) Real-space morphology of p9AA-24%Cs. (b) Simulated and (b) experimental I(q) profiles fit with the MHS and MHC models. Amorphous halo fit with *one or **two Lorentzians.

Table D.8 Analytical Fits to I(q) from X-ray Scattering and MD Simulations for p9AA-24%Cs

	MHC		MHS	
	Exp.**	Sim.**	Exp.**	Sim.**
R (nm)	0.36	0.33	0.48	0.43
Rca (nm)	0.58	0.52	0.74	0.65
L (nm)	5.52	3.04		
n (nm^{-3})	0.07	0.12	0.22	0.25

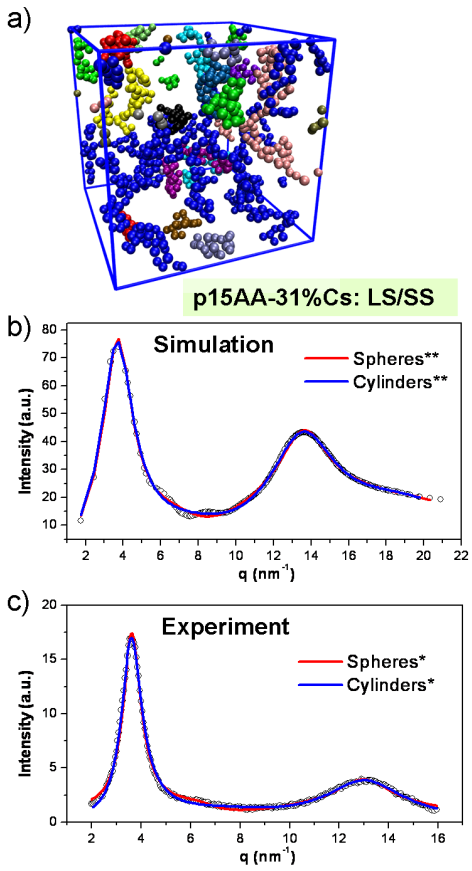

Figure D.9 (a) Real-space morphology of p15AA-31%Cs. (b) Simulated and (b) experimental I(q) profiles fit with the MHS and MHC models. Amorphous halo fit with *one or **two Lorentzians.

Table D.9 Analytical Fits to I(q) from X-ray Scattering and MD Simulations for p15AA-31%Cs

	MHC		MHS	
	Exp.*	Sim.**	Exp.*	Sim.**
R (nm)	0.24	0.27	0.53	0.45
Rca (nm)	0.71	0.66	0.92	0.81
L (nm)	5.86	5.39		
n (nm^{-3})	0.05	0.05	0.13	0.12

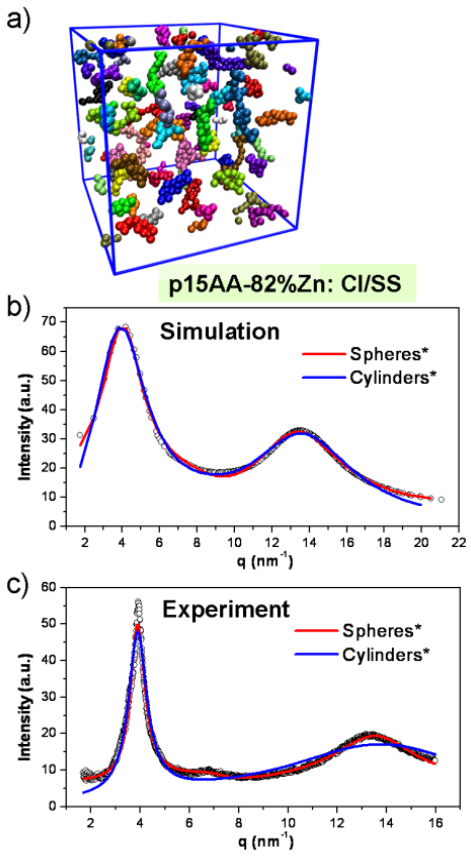

Figure D.10 (a) Real-space morphology of p15AA-82%Zn. (b) Simulated and (b) experimental I(q) profiles fit with the MHS and MHC models. Amorphous halo fit with *one or **two Lorentzians.

Table D.10 Analytical Fits to I(q) from X-ray Scattering and MD Simulations for p15AA-82%Zn

	MHC		MHS		Real space
	Exp.*	Sim.*	Exp.*	Sim.*	
R (nm)	0.32	0.26	0.50	0.39	0.41
Rca (nm)	0.65	0.57	0.88	0.72	0.76
L (nm)	6.50	5.85			
n (nm^{-3})	0.05	0.05	0.17	0.15	0.14

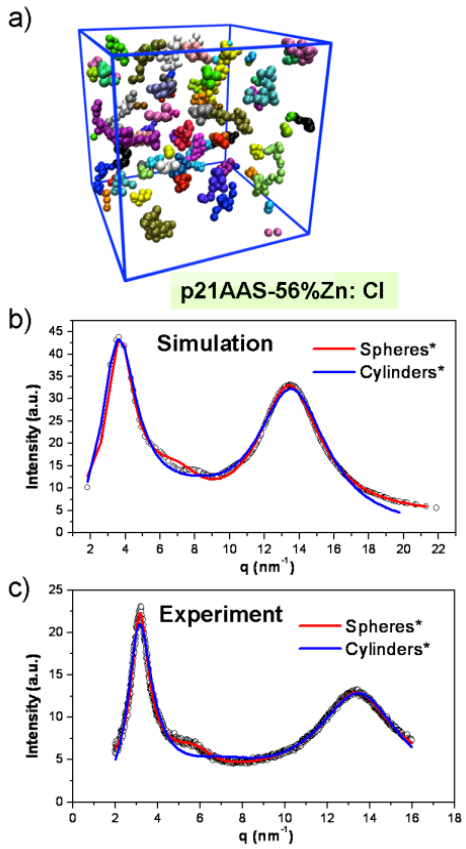

Figure D.11 (a) Real-space morphology of p21AA-56%Zn. (b) Simulated and (b) experimental I(q) profiles fit with the MHS and MHC models. Amorphous halo fit with *one or **two Lorentzians.

Table D.11 Analytical Fits to I(q) from X-ray Scattering and MD Simulations for p21AA-56%Zn

	MHC		MHS		Real space
	Exp.*	Sim.*	Exp.*	Sim.*	
R (nm)	0.11	0.21	0.50	0.37	0.46
Rca (nm)	0.79	0.65	1.02	0.82	1.01
L (nm)	5.46	5.49			
n (nm^{-3})	0.15	0.05	0.09	0.12	0.04